Investigation of Live-Bed Scour Around Circular Bridge Piers Under Flood Waves by Using Flow-3D

Firat Gumgum^{1*}, Mehmet Sukru Guney²

¹Dicle University, Department of Civil Engineering, 21280, Sur/Diyarbakir, Turkey.

²Izmir University of Economics, Civil Engineering Department, 35330, Balcova/Izmir, Turkey,

*Corresponding Author email: firat.gumgum@dicle.edu.tr

Abstract

In this study, an experiment concerning live-bed scour around circular bridge pier under unsteady flow conditions and its simulation performed by using the software FLOW3D are presented. Different turbulence models such as LES, RNG and two equations $k\text{-}\epsilon$ were tested separately and their effects on scour process were compared to each other, together with experimental findings. It was revealed that the LES turbulence model simulated better the scour around the pier while the RNG turbulence model simulated better both the scour in the wake region and the sediment transport. All these three turbulence models underestimated the scour depths compared to the experimental ones.

Key words

Live-bed Scour, Bridge Pier, Flood Waves, Flow-3D

1. INTRODUCTION

Local scour around bridge piers was registered as the most important reason for the bridge failures [1]. The mechanism of the local scour plays an important role in the design of the bridge foundations and the determination of the protection measures. There are many theoretical and experimental studies performed to enlighten the mechanism of the local scour, to predict the geometry of the scour hole and to evaluate the safety precautions ([2], [3], [4], [5], [6], [7] etc). Channel bottom slope, grain diameter, grain uniformity, flow characteristics, type and shape of the foundation etc. and the relationships between these parameters can differ significantly and result in numerous combinations. It would be extremely inconvenient to study all these combinations experimentally, and the financial burden would be very heavy. Therefore, it is more convenient to perform 3D numerical analyses with different combinations, as performed by various researchers in recent years.

Local scour is investigated under two headings; clear water scour, without sediment motion in the channel and live-bed scour at which sediment moves in the channel and feeds the scour hole during the scour process. Live-bed scour studies are quite rare compared to those performed in clear water conditions and there are very few live-bed scour investigations performed under unsteady flow conditions.

In this study, an experiment concerning live-bed scour around circular bridge pier under unsteady flow conditions and its simulation performed by using the software FLOW3D are presented. Different turbulence models such as LES, RNG and two equations k-ε were tested separately and their effects on scour process were compared to each other, together with experimental findings.

The file should be named with the surname of the Corresponding Author and the paper ID assigned.

2 Gungum and Guney

2. EXPERIMENTAL SET-UP

Experiments were carried out in a tilting flume 18.6 m long, 0.8 m wide and 0.75 m deep constructed in the Hydraulic Laboratory of Dokuz Eylul University Civil Engineering Department, within the scope of the project TÜBİTAK 106M274. The channel bottom slope was equal to 0.006. A schematic view of the flume is given in Figure 1 (a).

The circular pier of diameter 4 cm was placed at the 12th meter of the flume. The first 8 m and the last 5 m of the flume were filled with 20 cm thick gas concrete blocks. After the 3rd meter of the flume, the flume was covered with non-rippling sediment having 1.63 mm median diameter (d50) and 1.303 geometric standard deviation (σ g) to form a bed 25 cm thick.

Scour depth around the bridge pier was measured by Ultrasonic Velocity Profiler (UVP). Three transducers were located as follows: one at the upstream of the pier (T2) and two at the flanks of the pier (T1 and T3), as shown in Figure 1 (b).

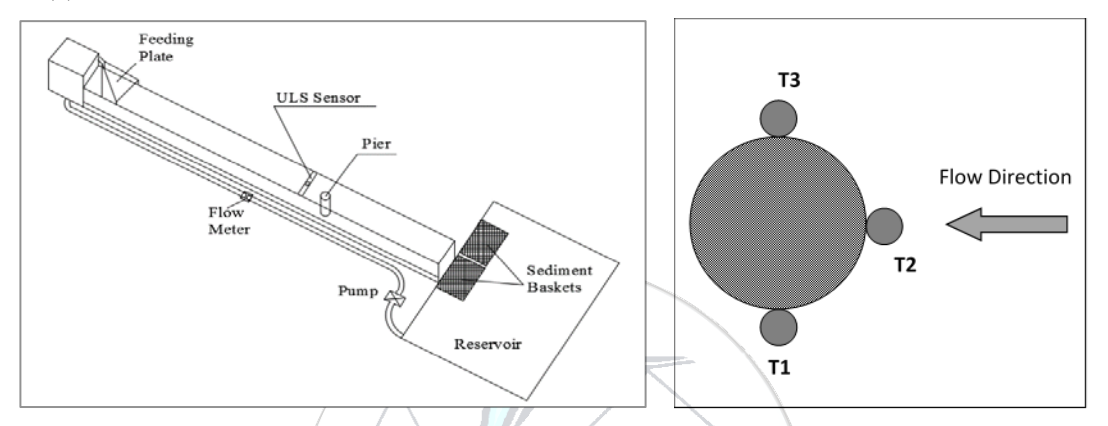


Figure 1. (a) Schematic view of the flume

(b) Location of the UVP transducers

Flow depths were measured by UltraLab ULS (Ultrasonic Level Sensor) manufactured by General Acoustics. Sediment was fed into the flume manually by means of the sediment feeding plate designed to provide uniform feeding, and collected by means of the baskets located at the end of the flume. Initially, a base flow of 1.5 L/s was conveyed to the flume for 10 minutes to provide a steady state. No scour was observed during this stage, as intended. Then, the triangular hydrograph with peak discharge of 20 L/s was generated. The durations of rising and falling limbs were equal to 3 minutes. The evolution of the scour was recorded by means of a high precision camera. Experiments were repeated to ensure the accuracy of experimental findings.

3. NUMERICAL STUDY

In the numerical model, the last 5.6 meters of the flume was disregarded in order to reduce the number of the mesh cells, hence saving the simulation time. Mesh cell side was taken as 1 cm along the flow and lateral directions and 0.5 cm in the vertical direction. General overview of the flume model is given in Figure 2. Red zones indicate the concrete blocks, blue zone indicates the packed sediment and cyan layer corresponds to the initial water surface.

Initial conditions (flow depth, velocity etc.) were defined as the initial steady state of the experiment. Simulation was realized by the isosceles triangle shaped hydrograph. LES, RNG and two equations k-ε turbulence models were used during the simulations. Maximum turbulent mixing length was chosen as "dynamically computed" because of time-varied flow depths. Critical Shields parameter was calculated from Shields diagram as 0.038. The frequently used Meyer-Peter & Müller equation was chosen to predict the bed load transport. As suggested in Flow-3D manual, the bed load and entrainment coefficients were taken as 8 and 0.018 respectively [8].

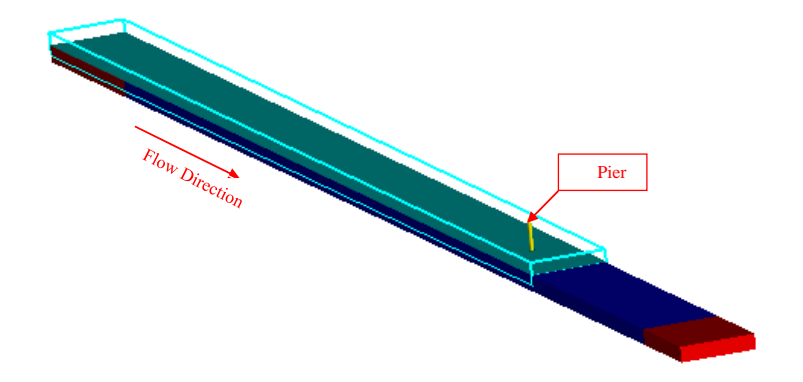


Figure 2. General overview of the flume model

4. RESULTS AND DISCUSSION

During the experiment, water level in the flume began to rise after the base flow of ten minutes. Flow filaments were evidently separated into two directions at the flanks of the pier and wake region began to develop. Two separate scour holes began to form at the flanks of the pier and met in front on the pier a few seconds later. With the increasing discharge, the development of horseshoe vortices enhanced the size of the scour hole rapidly and the scour hole took the shape of a frustum. After the flow velocity reached its critical value, sediment began to move and supply to the scour hole, causing fluctuations in scour depth and scour depth began to decrease during the falling limb. The bed material removed from the scour hole, and was drifted to downstream, 3-4 pier diameters away from pier, by wake vortices.

Similar process was obtained from the simulations. Figures 3 (a) and (b) represent the velocity fields in the wake region and at surrounding of the pier at peak time, respectively. In Figure 3 a, the wake region with the separation of the flow due to the pier existence can be distinguished. Its boundaries can be seen between the yellow and orange velocity fields. According to the velocity fields in Figure 3 b, downflow and horseshoe vortices seem not to be fully reflected.

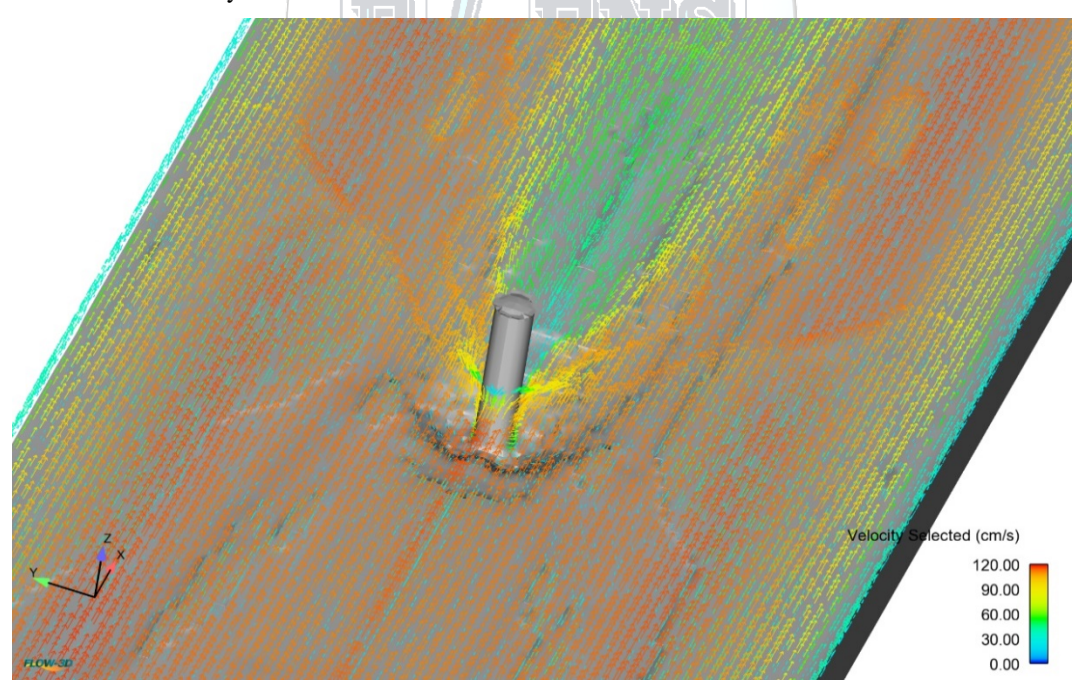


Figure 3. (a) The velocity field at the peak time in the wake region

4 Gumgum and Guney

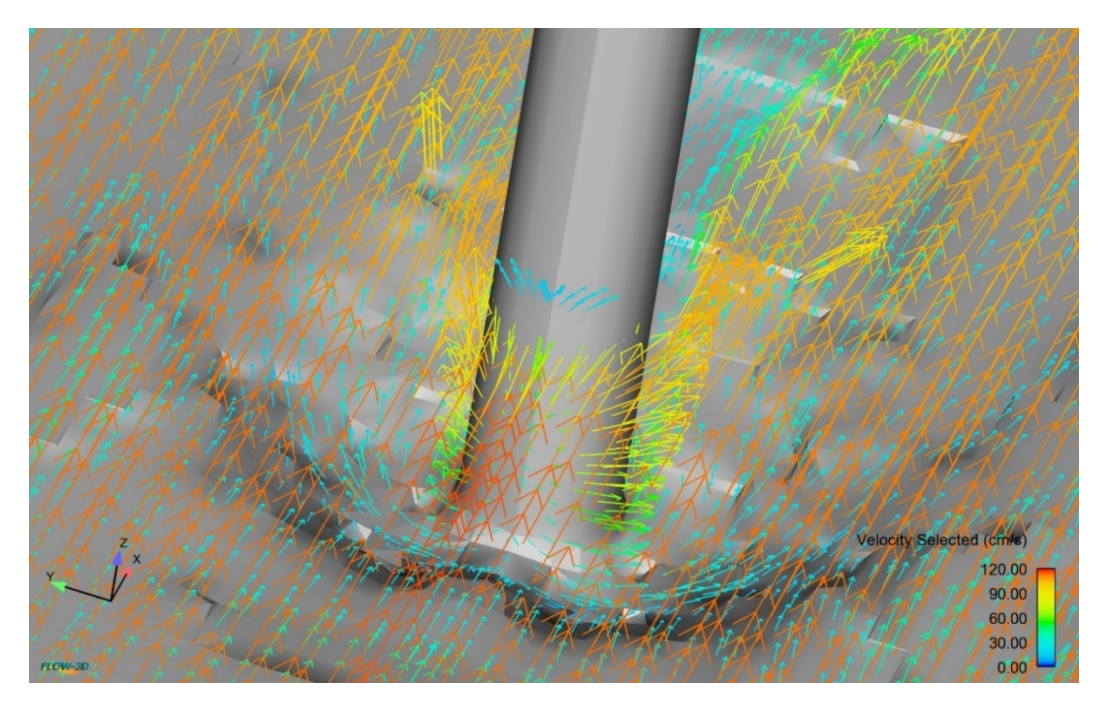


Figure 3. (b) The velocity field at the peak time in the surrounding of the pier

3D pictures of the scour hole were taken for each turbulence model at every 60 seconds. They are given in Figures 4, 5 and 6. for LES, RNG and two equation k-ε turbulence models, respectively.

The picture of scour hole corresponding to the end of the experiment is given in Figure 7.

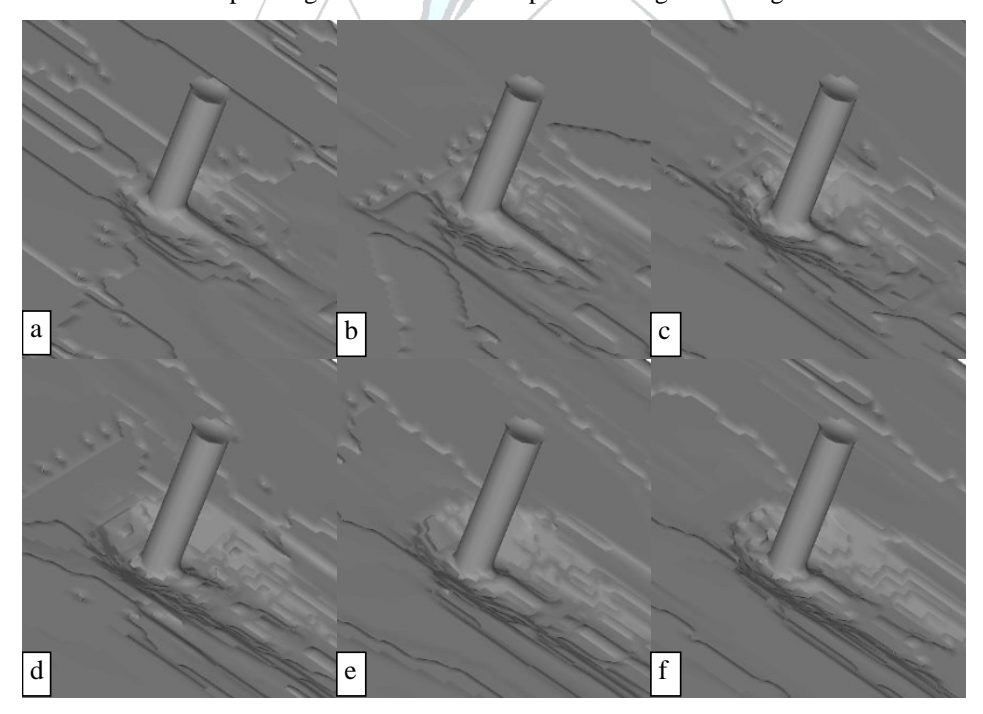


Figure 4. Pictures of the scour hole for LES turbulence model at a) 60 s. b) 120 s. c) 180 s. d) 240 s. e) 300 s. f) 360 s.

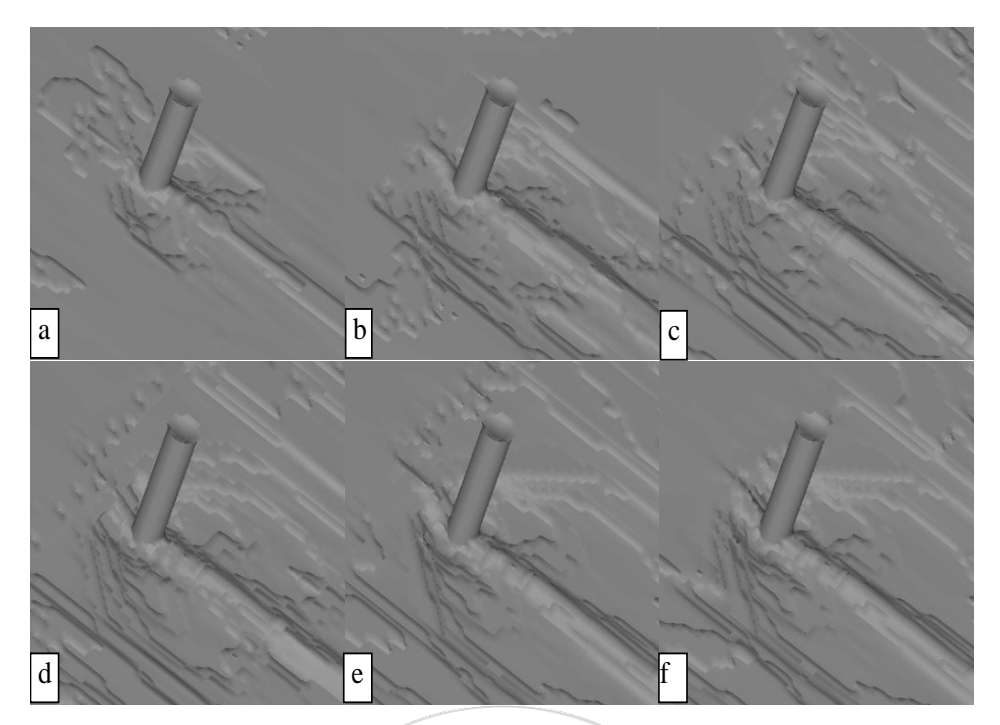


Figure 5. Pictures of the scour hole for RNG turbulence model at a) 60 s. b) 120 s. c) 180 s. d) 240 s.

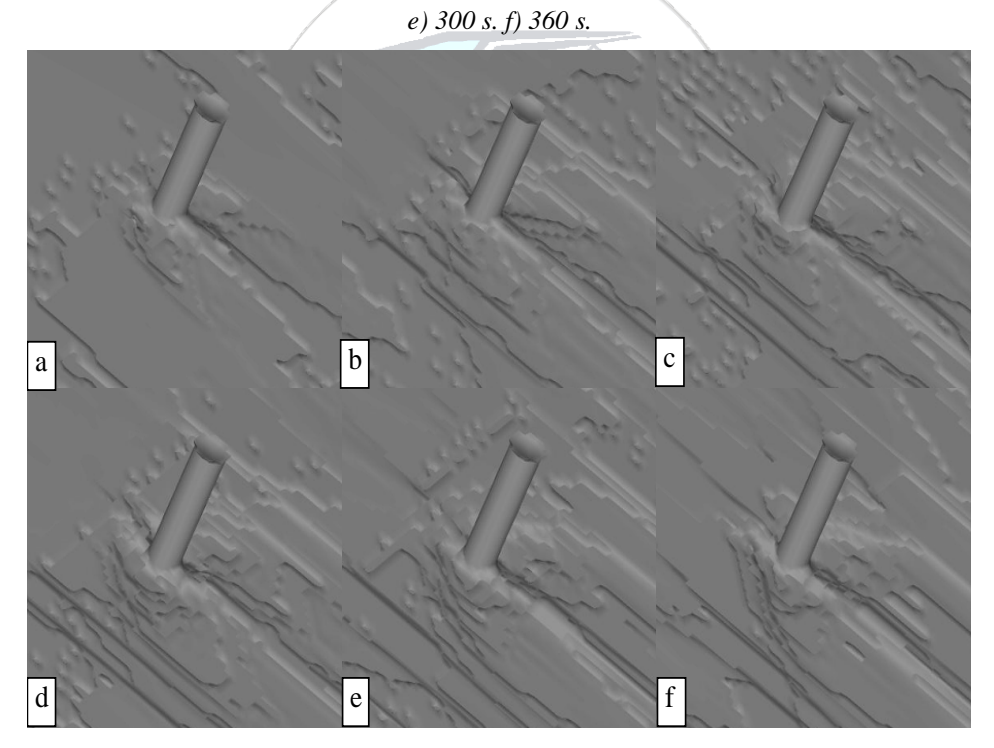


Figure 6. Pictures of the scour hole for k-\varepsilon turbulence model at a) 60 s. b) 120 s. c) 180 s. d) 240 s. e) 300 s. f) 360 s.

6 Gungum and Guney

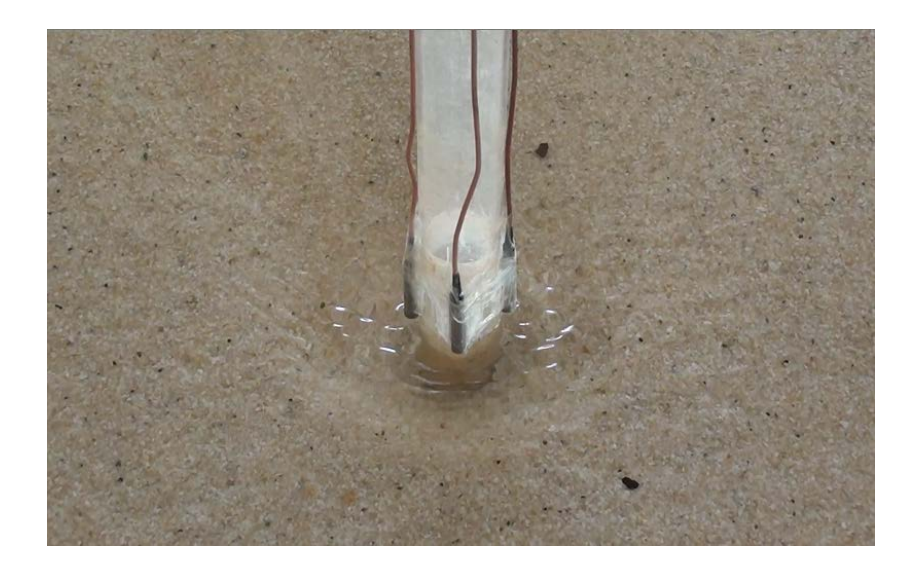


Figure 7. Picture of the scour hole at the end of the experiment (t=360 s)

It was found that the scour hole obtained by using the LES turbulence model was more similar to that obtained from the experiment. A "linear bump" occurred in front of the pier in all turbulence models but, this fact was not observed during the experiments. The frustum shaped of the scour hole seen in Fig. 7 was not obtained in the used turbulence models, except LES turbulence model at which this configuration appeared between 180 and 240 seconds. This situation caused lower scour depths in front of the pier compared to those at flanks, this fact being contradictory to the experimental results.

Maximum scour depths were observed approximately at the 240th second of the simulations. Figure 8, 9 and 10 show plan views of the scour hole at 240th s of the simulation for LES, RNG and two equations k-ε turbulence models, respectively (units are in centimeters). The LES turbulence model simulated scouring in front of the pier much better than the other turbulence models even if it gave lower scour depths compared to those at flanks. The RNG turbulence model simulated scouring in wake region better than the LES model.

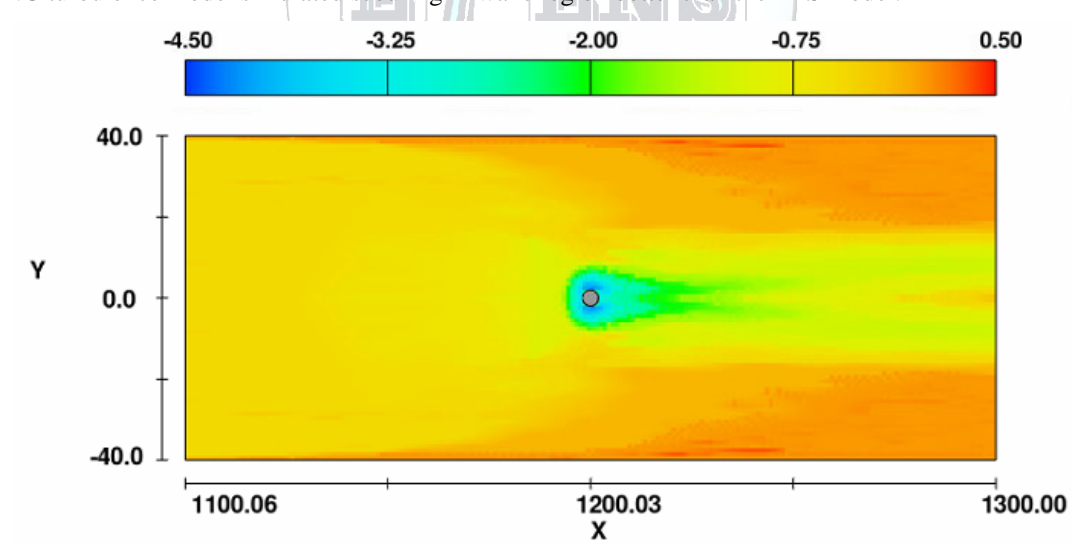


Figure 8. Plan view of scour holes in the case of the turbulence model LES

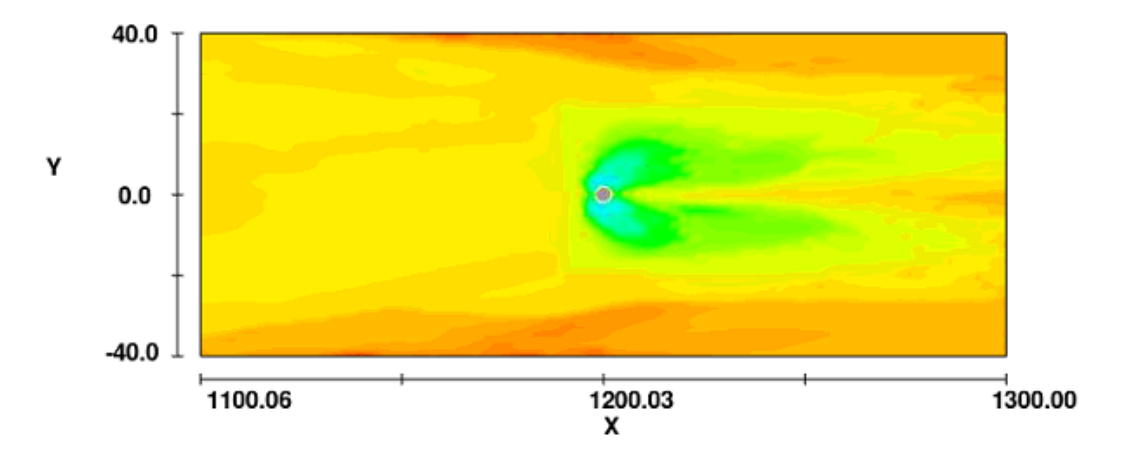


Figure 9. Plan view of scour holes in the case of the turbulence model RNG

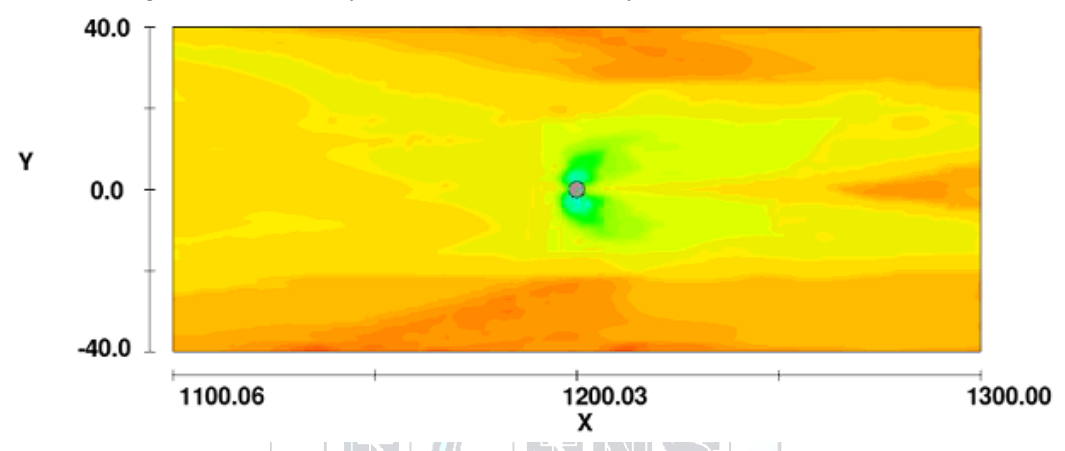


Figure 10. Plan view of scour holes in the case of the turbulence model two equations k- ε The numerical and experimental time dependent scour depths at flank (T1) and front (T2) are given in Figure 11.

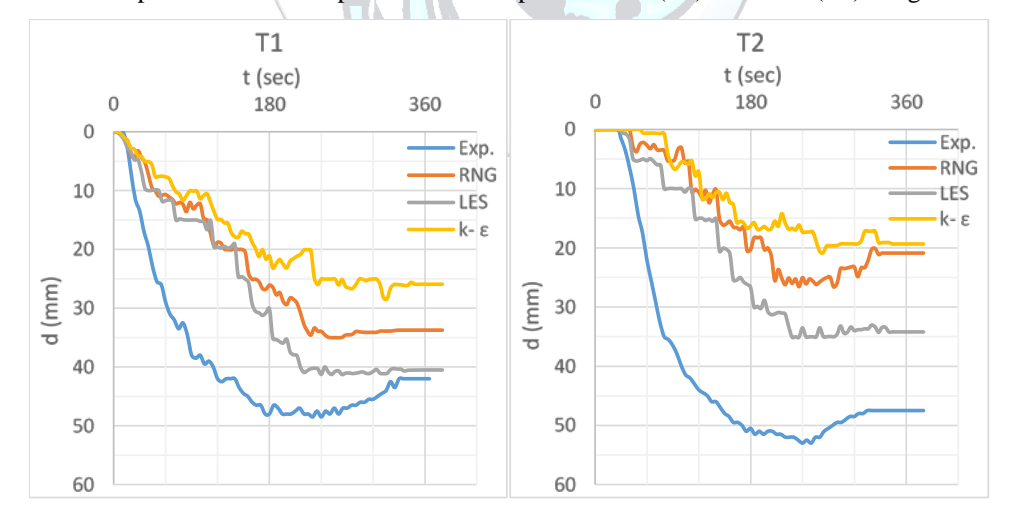


Figure 11. Time-varied numerical scour depths and experimental ones

The time-varied scour depths obtained from the simulations were found to be smaller than the experimental ones.

Scouring was found to be more rapid during the experiments. For example, at flank T1, during the experiments the scour depth of 20 mm was reached approximately at the 40th second, while this value was 115 s, 130 s, and 165 s in the case of the turbulence models LES, RNG and two equations k- ϵ , respectively.

By contrast with experimental findings, the scour depths at front were found smaller compared to those calculated at flanks.

5. CONCLUSIONS

The turbulence model RNG seems to reflect better the sediment transport, since the final scour depth was found to be smaller than the maximum scour depth. On the other hand, the scour depths calculated by using turbulence model LES are relatively much closer to those obtained from the experiments.

ACKNOWLEDGMENTS

The authors thank Dokuz Eylul University for the financial support provided through the scientific research project BAP (Project Number 2016.KB.FEN.003).

CONFLICT OF INTEREST STATEMENT

The authors declare that there is no conflict of interest.

REFERENCES

- [1]. Laursen, Emmett M., Toch, Arthur. Scour around bridge piers and abutments. Vol. 4. Ames, IA: Iowa Highway Research Board, 1956.
- [2]. Jain, Subhash C., Fischer, Edward E. Scour around circular bridge piers at high Froude numbers (No. FHWA-RD-79-104 Final Rpt.), 1979.
- [3]. Chiew, Yee-Meng. Local scour at bridge piers (Doctoral dissertation, ResearchSpace@ Auckland), 1984.
- [4]. Kothyari, U. C., K. G. Ranga Raju, and R. J. Garde. "Live-Bed Scour Around Cylindrical Bridge Piers." Journal of Hydraulic Research 30, no. 5 (September 1992): 701–715. doi:10.1080/00221689209498889.
- [5]. Melville, Bruce W. "Live-bed Scour at Bridge Piers." Journal of Hydraulic Engineering 110, no. 9 (September 1984): 1234–1247. doi:10.1061/(asce)0733-9429(1984)110:9(1234).
- [6]. Sheppard, D. Max, and William Miller. "Live-Bed Local Pier Scour Experiments." Journal of Hydraulic Engineering 132, no. 7 (July 2006): 635–642. doi:10.1061/(asce)0733-9429(2006)132:7(635).
- [7]. Yanmaz, Ali M. "Köprü Hidroliği" METU Press, (October, 2002)
- [8]. Marion, Andrea, Matteo Tregnaghi, and Simon Tait. "Sediment Supply and Local Scouring at Bed Sills in High-Gradient Streams." Water Resources Research 42, no. 6 (June 2006). doi:10.1029/2005wr004124.
- [9]. Singer, Michael Bliss. "Downstream Patterns of Bed Material Grain Size in a Large, Lowland Alluvial River Subject to Low Sediment Supply." Water Resources Research 44, no. 12 (December 2008). doi:10.1029/2008wr007183.
- [10]. Ferrer-Boix, Carles, and Marwan A. Hassan. "Influence of the Sediment Supply Texture on Morphological Adjustments in Gravel-Bed Rivers." Water Resources Research 50, no. 11 (November 2014): 8868–8890. doi:10.1002/2013wr015117.
- [11]. Pfeiffer, Allison M., Noah J. Finnegan, and Jane K. Willenbring. "Sediment Supply Controls Equilibrium Channel Geometry in Gravel Rivers." Proceedings of the National Academy of Sciences 114, no. 13 (March 13, 2017): 3346–3351. doi:10.1073/pnas.1612907114.
- [12]. Hong, Jian-Hao, Yee-Meng Chiew, Po-Hung Yeh, and Hsun-Chuan Chan. "Evolution of Local Pier-Scour Depth with Dune Migration in Subcritical Flow Conditions." Journal of Hydraulic Engineering 143, no. 4 (April 2017): 04016098. doi:10.1061/(asce)hy.1943-7900.0001261.
- [13]. Wang, Le, Alan Cuthbertson, Gareth Pender, and Deyu Zhong. "Bed Load Sediment Transport and Morphological Evolution in a Degrading Uniform Sediment Channel Under Unsteady Flow Hydrographs." Water Resources Research 55, no. 7 (July 2019): 5431–5452. doi:10.1029/2018wr024413.
- [14]. Gumgum, Firat, and Mehmet Sukru Guney. "Time Dependent Live-Bed Scour Around Circular Piers Under Flood Waves." Periodica Polytechnica Civil Engineering (January 1, 2020). doi:10.3311/ppci.14664.
- [15]. Guney, M. Sukru, Gokcen Bombar, Aysegul O. Aksoy, and Mustafa Dogan. "Use of UVP to Investigate the Evolution of Bed Configuration." KSCE Journal of Civil Engineering 17, no. 5 (June 28, 2013): 1188–1197. doi:10.1007/s12205-013-0131-5.
- [16]. Aksoy, Aysegul Ozgenc, Gokcen Bombar, Tanıl Arkis, and Mehmet Sukru Guney. "Study of the Time-Dependent Clear Water Scour Around Circular Bridge Piers." Journal of Hydrology and Hydromechanics 65, no. 1 (March 1, 2017): 26–34. doi:10.1515/johh-2016-0048.
- [17]. Melville, Bruce W., and Yee-Meng Chiew. "Time Scale for Local Scour at Bridge Piers." Journal of Hydraulic Engineering 125, no. 1 (January 1999): 59–65. doi:10.1061/(asce)0733-9429(1999)125:1(59).
- [18]. Melville, Bruce W. "Pier and Abutment Scour: Integrated Approach." Journal of Hydraulic Engineering 123, no. 2 (February 1997): 125–136. doi:10.1061/(asce)0733-9429(1997)123:2(125).
- [19]. Yen, Chin-lien, and Kwan Tun Lee. "Bed Topography and Sediment Sorting in Channel Bend with Unsteady Flow." Journal of Hydraulic Engineering 121, no. 8 (August 1995): 591–599. doi:10.1061/(asce)0733-9429(1995)121:8(591).

- [20]. Lee, Kwan Tun, Yi-Liang Liu, and Kai-Hung Cheng. "Experimental Investigation of Bedload Transport Processes Under Unsteady Flow Conditions." Hydrological Processes 18, no. 13 (August 27, 2004): 2439–2454. doi:10.1002/hyp.1473.
- [21]. Bombar, Gökçen, Şebnem Elçi, Gokmen Tayfur, M. Şükrü Güney, and Aslı Bor. "Experimental and Numerical Investigation of Bed-Load Transport Under Unsteady Flows." Journal of Hydraulic Engineering 137, no. 10 (October 2011): 1276–1282. doi:10.1061/(asce)hy.1943-7900.0000412.
- [22]. Graf, W. H., Suszka, L. "Unsteady flow and its effect on sediment transport." 21st IAHR congress. 1985.
- [23]. De Sutter, Renaat, Ronny Verhoeven, and Andreas Krein. "Simulation of Sediment Transport During Flood Events: Laboratory Work and Field Experiments." Hydrological Sciences Journal 46, no. 4 (August 2001): 599–610. doi:10.1080/02626660109492853.



Comparison of Power Line Communication Infrastructures

Bugrahan Uzun^{1*}, Okan Ozgonenel²

¹Ondokuz Mayıs University, Department of Electrical and Electronics Engineering, 55270, Atakum/Samsun, Turkey.

²Ondokuz Mayıs University, Department of Electrical and Electronics Engineering, 55270, Atakum/Samsun, Turkey.

*Corresponding Author email: bugrauzun55@hotmail.com

Abstract

In this paper, better advantageous communication method is investigated by comparing powerline communication methods. Pros and cons of PLC method and wireless communication methods are compared. After choosing PLC as the communication method, noise, channel impedance and signal weakening problems that have negative effects of data transmission over the transmission line are examined. AMS, SCADA, PRIME, G3 methods were compared. Modulation methods that may be suitable for transmission line communication are compared. Transmission line communication system simulation is designed with BPSK modulation method. The carrier signal, which is at very high frequencies compared to the 50Hz frequency network signal transmitted over the transmission line, is modulated with the BPSK signal. The information signal to be transmitted is sent via BPSK modulation over the transmission line. At the transmission line output, the demodulation process is applied and the information signal at the input is read at the output. PSIM is used for computer simulations and performance curves are evaluated over different PLC modulation techniques.

Key words

Power Line Communication, Distribution Lines, Transmission Lines, Power Quality

1. INTRODUCTION

Rapid increase of technological developments in our country today, provides the infrastructure for studies on the use, security and analysis of powerlines. In our age there is a need for fast communication, apart from the need for a house or device where only electricity was transmitted. This situation creates an environment for a faultless, continuous and efficient energy to reach the consumer. In addition to technological developments, the increased day by day. Besides, the need for electrical energy in all areas, especially the production sector, service sector and telecommunication sector, is increasing day by day.

The use and dissemination of radio frequencies have played a major role in the development of communication. The advantages and disadvantages of two different communication methods, wired and wireless, have been examined and applied according to the area of use and purpose. Information exchange over energy transmission lines, which have a low-cost effect in wired communication, emerged in the 1800s with the studies of the scientists of the period and has reached to the present day.

The data signal to be transmitted in the exchange of information over the powerline is superimposed with the help of high-frequency carrier signals and applied to the energy transmission line. The signal transmitted over the transmission line is then filtered with the help of filters and the information signal is seen on the receiver side. By this way, communication takes place. Since the transmission line cabling had already been done, one of the biggest advantages of the communication system over the energy transmission line is that it is an economical method since there is no need for wiring.

2. MATERIALS AND METHODS

In this study, studies on power line communication, application areas, negative effects that may be encountered during transmission and thrust techniques have been examined. In this context, simulation studies that can set an example for power line communication have been done. For this purpose, the advantages and disadvantages of IHH applications compared to each other were compared. Transmission line communication applications are separated according to many characteristics. The pros and cons of AMS, SCADA, PRIME and G3 power line communication methods are examined below.

2.1. Plc Negative Effects

The main problems of powerline communication are noise, channel impedance and signal reduction. Information exchange for powerlines has a destructive channel effect. Changing impedance and noise cause the impact of communication to be questioned and to lose its importance. Therefore, it is required to propose a new solution to the three-way relationship depending on time, speed and signal level. Noise, channel impedance and signal weakening are examined below.

• Noise: Depending on the size of the noise, the disruptive effect on the sinusoidal wave increases. Increasing the disruptive effect is undesirable. It damages the functioning of the communication system. The effect of noise should be reduced as much as possible. When we apply 5- times to sinusoidal wave in MATLAB program, the changes that occur to the sign are seen in Figure 1 and Figure 2.

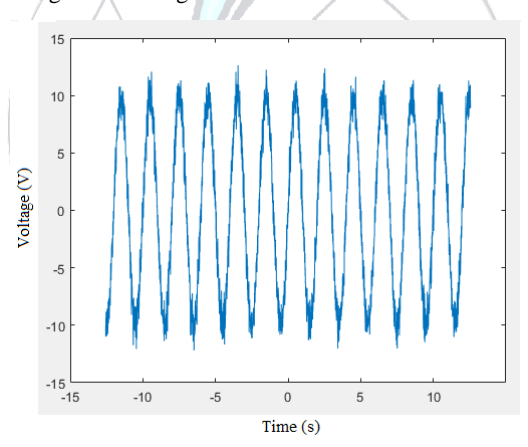


Figure 1. One way noiseless

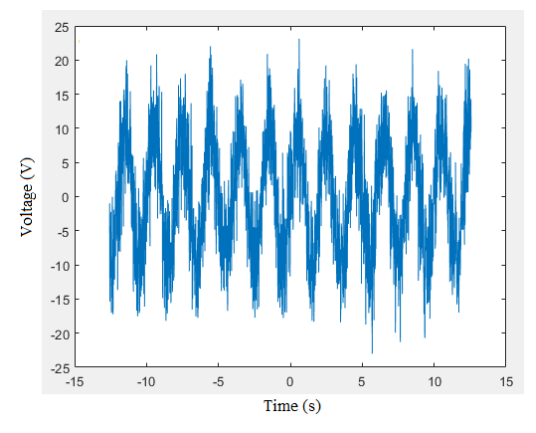


Figure 2. One way 5 times noise

• Channel Impedance: The electricity grid is quite complex and brings together many systems simultaneously. The imbalance in channel impedance caused by system-connected loads and distribution elements makes it difficult to exchange information. The imbalance that comes to the challenge in the channel impedance negatively affects the signal strength in the output. This causes afailed communication environment between the informational and the receiver. In order to investigate the effect of channel impedance disorder on the sign, in urban and industrial areas, CENELEC in Turkey, B, a series of measurements between 10 and 170 kHz bands C and D were obtained. Based on these measurements, 3-17 Ω in rural areas, 1-17 Ω in urban areas and 1-21 Ω in industrial areas were determined. in addition, signal weakening in these bands was found to be 4-30 dB when looking at phase-neutral, phase-earth and neutral-earth measurements for different power lines. The output ports and modem output impedance and power line input impedance must be mapped appropriately for the transfer of power between the power line and IHH. For an efficient modem design, the power line impedance must be known. Power line impedance varies according to the location of the power lines. Time impedance depends on many factors, including loads on transmission lines, day or night power leps. Therefore, bands, sign levels and procedures have been determined in Europe and CENELEC, EN-50,065-1 has emerged.

• Signal Reduction: On the transmission line, there may be differences between the signal sent from the input and the signal received from the output, and deterioration of the signal quality may occur. The main causes of disturbances on the power line are as follows. Transmission Stage Type, Transmission speed, Communication Distance. The reasons for distortion of the transmission are as follows. Signal Weakening, Restricted Bandwidth, Delay Corruption, Noise. Signal reduction occurs by decreasing signal strength depending on communication distance. Solution can be provided by using signal booster or repeater. This change in signal level can be shown as in equation (1).

$$dB = 10log\left(\frac{Signal\ Output\ Power}{Signal\ lnput\ Power}\right) \tag{1}$$

If we talk about the effect of noise on the signal, the most important criterion is the SNR shown in equation (2). The following formula is used to understand how much the sign is weakened. Signal reduction is 100 dB per kilometer for LV lines and 10 dB per kilometer for MV lines. The more signal reduction is seen in Low Voltage networks. By using repeaters at distances less than 1 km, signal reduction is prevented.

$$SNR(dB) = 10log\left(\frac{Signal\ Power}{Noise\ Power}\right) \tag{2}$$

2.2. Qpsk Modulation Methods

QPSK modulation is a type of numerical modulation. PSK enters the modulation class. The process of transmitting the logic1 and logic0 information given by the 2-bit information signal to be transmitted at the input with the help of four different and high frequency carrier signals with 90 ° phase difference between them is called QPSK modulation. The carrier phase angles connected to the information sign bits are included in Table 1.

Table 1. QPSK Data Signal Bits and Carrier Signal Phase Angels

ВІТ	PHASE
00	45°
01	135°
10	225°
11	315°

The four carrier signs with 90 $^{\circ}$ phase difference between them are high frequency sinus signs named as 00, 01, 10, 11 as seen in Figure 3.

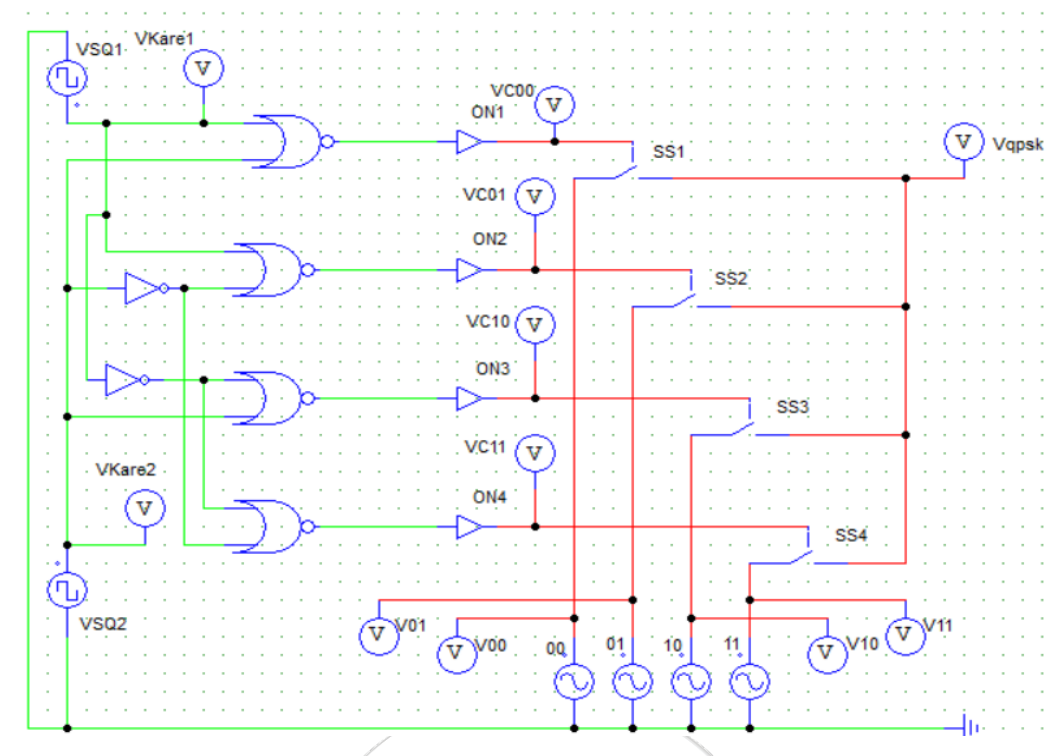


Figure 3. QPSK Modulation Circuit on PSIM

The carrier signal chart simulated in the PSIM program is as follows.

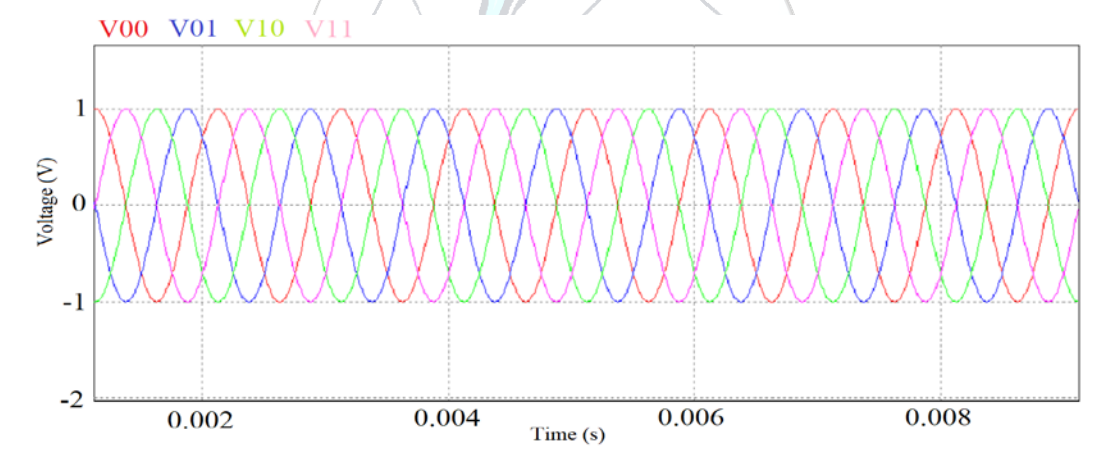


Figure 4. 90° Phase Angel High Frequency 4 Carrier Signal on PSIM

Depending on the 1 or 0 status of the information to be ed, only one of the carrier signs is turned on and the others are closed, with the help of switching the mark from 1 to 0 and 0 to 1 of the mark coming out of 2 different square waves. Thus, only one superimposed sign is seen. In Figure 3, this switching is provided with the help of ON and SS elements, and the Vqpsk signal is seen in Figure 5.

As seen in Figure 3, four different carriers are activated and deactivated according to the 1 and 0 states of the elements Vkare1 and Vkare2. The open-closed state of the carriers switched by square waves is shown in Figure 4. When examined in certain time frame intervals, only one carrier is active for each second interval. Information transmission is carried out by that carrier for the time intervals during which carriers are active. This is how Vqpsk is working for the modulation method. Table 2 and Figure 5 has a QPSK modular output mark.

14 Uzun and Ozgonenel

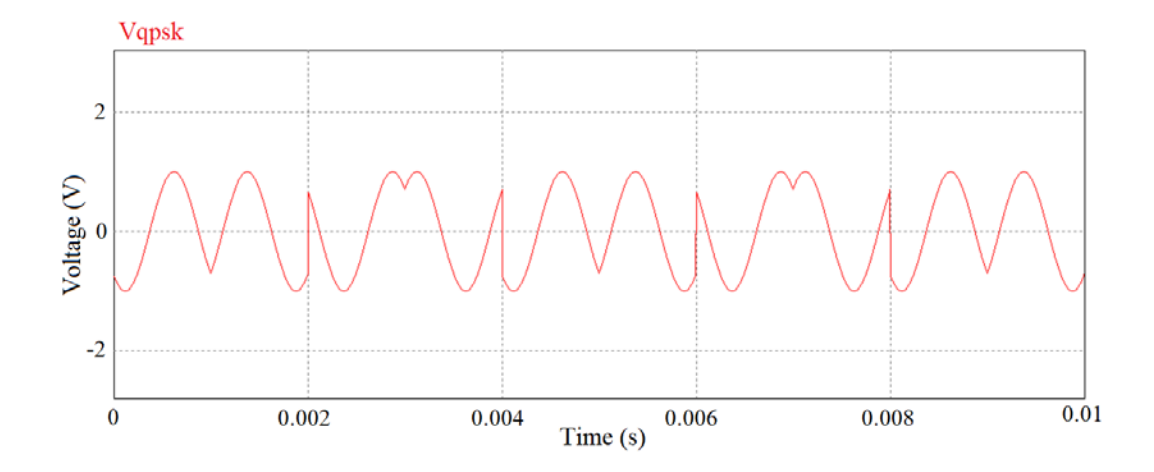


Figure 5. QPSK Modulation Output Signal on PSIM

2.3. Bpsk Modulation Methods

We will carry out the data transmission with BPSK modulation with the circuits we have built on PSIM. BPSK, which is treated with switching logic, will be provided by in and out of the open-closed state of carriers with different phase angle and the same frequency. Thus, continuity will be provided in the information mark to be transmitted and a healthy communication will be made.

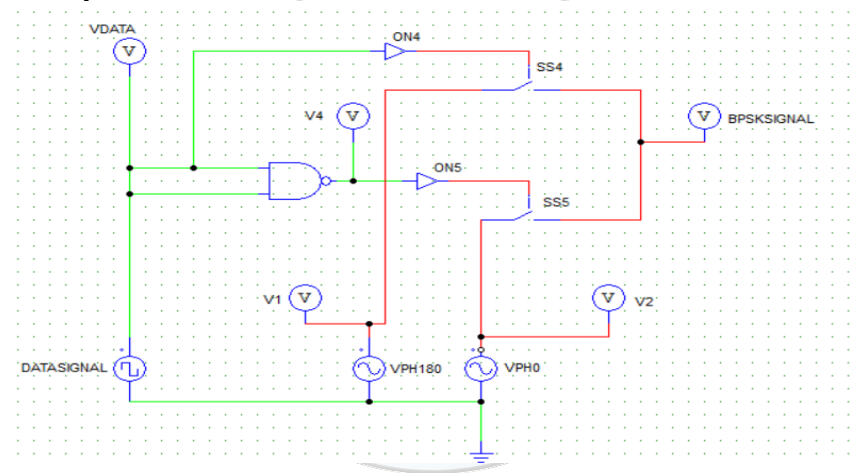


Figure 6. BPSK Modulation Circuit on PSIM

The data signal to be transmitted in the circuit above has a frequency of 1 Volt and 100 Hz. The VPH180 is a carrier signal with a phase angle of 10000 Hz 180°. Our other carrier signal is the VPH0, a carrier signal with a phase angle of 10000 Hz0°. With the NAND gate in the circuit, the data signal creates the modular signal by switching according to the status of 1 and 0.

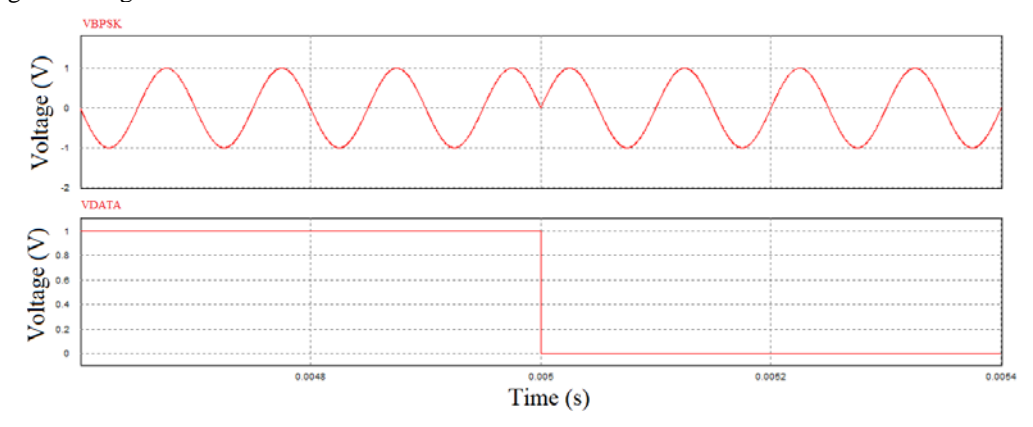


Figure 7. Data Signal and BPSK Modulated Signal

3. RESULTS AND DISCUSSION

The combination of 2FKA superimposed data signal and grid signal is applied to the transmission line. The shape of the signal passing over the Vihson voltage probe after its transmission over the transmission line is as follows.

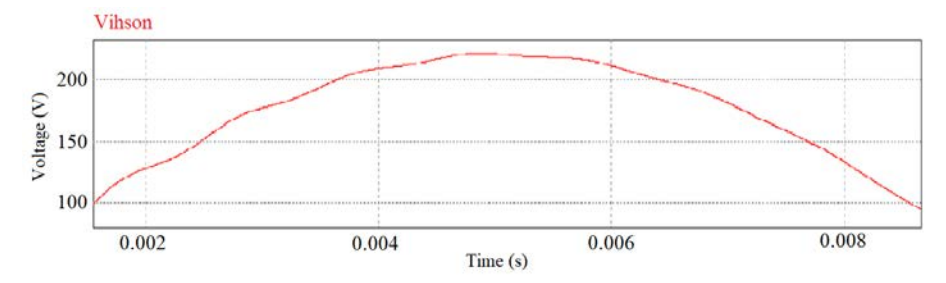


Figure 8. Power Line Output Signal

Since the BPSK signal is a very high frequency sign, it shows faster and shorter changes on a 220 Volt and 50 Hz grid signal. Therefore, it is observed that it creates small fluctuations on the network signal. The data signal is transmitted over the power line after BPSK modulation. However, the system cannot detect the function of the signal and does not work because the signal that appear from the power line output is over-boarded. For this reason, the superimposed signal at the exit of the transmission line must go through the decomposition process and return to the square wave format. Thus, the system continues to run by getting the correct input-output information. BPSK sign demodulation circuit is as follows.

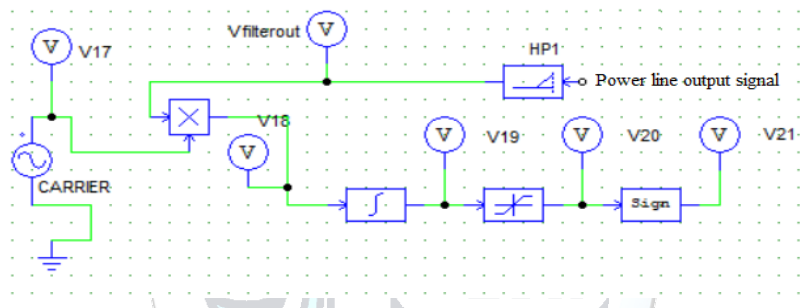


Figure 9. BPSK Demodulation Circuit

The signal from the power line is filtered with the help of a high pass filter. Then, the separation process is completed by taking integral and derivative functions of the mark combined with the carrier signal, respectively. At the beginning of the circuit, the desired square wave, at the end of the circuit with the demodulation process will find its own form.

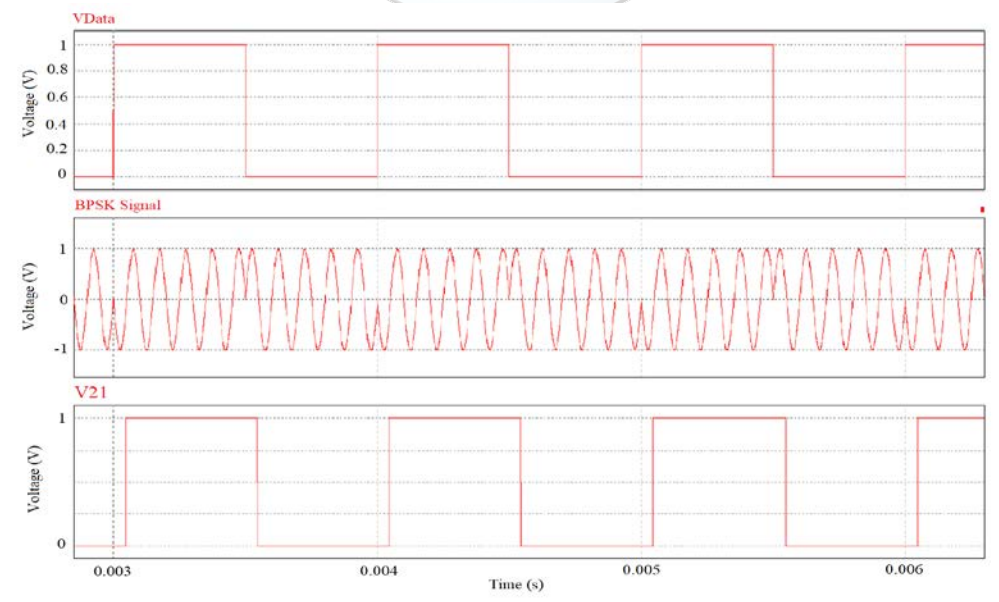


Figure 10. Input Data Signal, BPSK Signal and Output Data Signal

In this study, studies on power line communication, application areas, negative effects that may be encountered during transmission and thrust techniques have been examined. In this context, simulation studies that can set an example for power line communication have been done. For this purpose, the advantages and disadvantages of IHH applications compared to each other were compared. Transmission line communication applications are separated according to many characteristics. The pros and cons of AMS, SCADA, PRIME and G3 power line communication methods are examined below.

AMS is a remote meter reading application. With AMS, consumption values on the counter can be read remotely. If we look at the pros, personnel expenses have been reduced with this application. Reading consumer consumption values is done more accurately without allowing human error. Missing fugitives can be tracked. Cons, on the other hand, cannot provide control along the power line. It cannot analyze the entire power line system between the source and the consumer. It cannot predetermine the interruptions that may be caused by line protection elements and provide an instant solution. It cannot offer improvement by matching and comparing the information received from the meters with each other. It cannot locate fault. It cannot keep records because it cannot detect malfunctions.

The SCADA system is a central inspection and information collection application in which complex system transmission lines are managed from a single center. It can switch on and off remotely. In case of line failure, it can control the feeding of the transmission line from a different place. It can instantly monitor all consumers and feeders along the power transmission line. The malfunction can be located. It can keep track of where and when the fault occurred. When we examine these features, it can be seen that the SCADA system is much superior to the AMS system.

G3 and PRIME have more developed features than SCADA and AMS. Scada is an energy monitoring system. Compared to SCADA, G3 and PRIME are superior because it works based on PLC. It can make more detailed power line analysis. It can create and apply different solution scenarios according to the failure situations that may ocur.

4. CONCLUSIONS

G3 power line communication system emerged after the PRIME system. G3, one of the new technologies of the last period, has similar features to PRIME. Remote on-off and line fault location detection. It is able to control all systems along the power line by doing network analysis. It can prepare different consumer feeding scenarios depending on the on-off situations of the protection elements for each failure situation. G3 transmission speed is slower than PRIME. More G3s are preferred for long-distance transmissions as a plus of noise resistance. PRIME has more transport channels than G3. G3 uses the IPv6 package. PRIME uses the IPv4 package. Therefore, G3, which uses an IPv6 package, provides a more secure network environment than prime. The G3 can find up to 36 different transport channels, while PRIME can have 96 different transport channels. This allows larger data to be sent through different channels in terms of data submission. In terms of noise resistance, the G3 is more advanced. The G3 system has more noise resistance than the PRIME system. This provides a win for communication over long distances. G3 is more stable than PRIME. The priority in the powerline is to maintain the communication more stable. Therefore, G3 is more preferred than PRIME.

ACKNOWLEDGMENT

I would like to express my gratitude to Prof.Dr.Okan Ozgonenel who guided me along this project. I would also like to thank my wife, daughter and all family members who supported me and offered deep insight into the study.

CONFLICT OF INTEREST STATEMENT

The author(s) declare(s) that there is no conflict of interest.

REFERENCES

- [1]. Chariag, D., Guezgouz, D., Raingeaud, Y., Lebunetel, C., "Channel Modeling and Periodic İmpulsive Noise Analysis in İndoor Power Line", IEEE, 2011
- [2]. Achaichia, P., Le Bot, M., Siohan, P., "Potential İmpact of the CENELEC Spectral Mask on Broadband PLC Networks", IEEE, 2013
- [3]. Al-Mawali, S., Al-Qahtani, S., Hussain, M., "Adaptive Power Loading of OFBÇ-Based Power Line Communications İmpaired by İmpulsive Noise", IEEE, 2010
- [4]. Adeyemi, A., Emanuel, O., "An Agent-Based Adaptive BPSK/QPSK Modülation for Rice-Longnormal Channel", IEEE, 2007

- [5]. Chehri, A., "A Low Complexity Turbo Equalizer for Power-Line Communication with Applications to Smart Grid Networks", IEEE, 2019
- [6]. H. Meng, S. Chen, Y. Guan, C. Law, P. So, E. Gunawan, et al., "Modeling of transfer characteristics for the broadband power line communication channel", *IEEE Trans. Power Del.*, vol. 19, no. 3, pp. 1057-1064, Jul. 2004
- [7]. Sharma, A., Majumdar, S., Naugarhiya, A., Acharya, B., Majumder, S., Verma, S., "VERILOG Based Simulation of ASK, FSK, PSK, QPSK digital Modulation techniques", I-SMAC, 2017
- [8]. Ustun Ercan, S., Ozgonenel, O., W. P. Thomas, D. "Power line communication channel for smart grid", Smart Grids and Cities Congress and Fair (ICSG) 2018 6th International Istanbul, pp. 208-212, 2011
- [9]. Yadav, P., Saini, L., "Powerline FSK Communication Using Signal Wire Technique", IEEE, 2017
- [10]. Washiro, T., "Applications of RFID Over Power Line for Smart Grid", IEEE, 2012
- [11]. Zheng, X., Tao, Y., "Analysis on using transmission lines travelling wave fault location based on fault information system", IEEE, 2011



Water Supply and Sewerage System in the Republic of Croatia and the Republic of Slovenia

Marija Šperac^{1*}, Dino Obradović²

¹Josip Juraj Strossmayer University of Osijek, Faculty of Civil Engineering and Architecture Osijek, 31000 Osijek, Croatia.

² Josip Juraj Strossmayer University of Osijek, Faculty of Civil Engineering and Architecture Osijek, 31000 Osijek, Croatia.

*Corresponding Author email: <u>msperac@gfos.hr</u>

Abstract

According to forecasts of various international organizations, it is estimated that by 2040 the Earth will be left with no sufficient quantities of drinking water. Water used for supplying drinking water to the population and industry is obtained from natural resources (i.e., the environment) and is distributed through the water supply system to the consumer. The used, polluted water is returned to the environment through the sewerage system with prior water treatment. During the distribution of drinking water through the water supply system, water losses occur. Such lost water does not reach the end consumers and is not even charged by the water supply company. These interconnected processes of obtaining water used for water supply and of returning polluted water to water resources, directly affect the changes in the quantity or quality of water, as well as the local environment and the local population, and, of course, the Earth in general. This paper will analyze statistical data on water supply (the total amount of water intake, distributed water, water losses, length of the water supply network, the number of water supply connections) and sewerage (total amount of wastewaters, length of sewerage network, number of sewerage connections) in the Republic of Croatia and the Republic of Slovenia. The interdependence of these elements will be presented through correlation coefficients.

Key words

Correlation, Sewerage system, Statistics, Water supply

1. INTRODUCTION

Water covers more than 70% of the Earth's surface. However, 97% of water is salty, 2% is trapped in glaciers, and remains only 1% of fresh drinking water. The role of water is multifaceted: it is a crucial necessity, a habitat for plant and animal species, a local and global resource, a transport corridor and a climate regulator. But for the last two centuries water has become the ultimate destination for many pollutants released into the environment.

We collect water for water supply from natural sources; we use it, and return wastewater back to nature. The characteristic feature of today's world is that the heavily polluted wastewater is increasing and the quality water supply is decreasing. In addition to high water pollution levels, losses occurring in the water supply system have a major impact on water supply. The causes of water losses in the water supply system may be different, e.g. the age of the system, pipe porosity, poor system management, illegal water connections to the system, failures and pipe breaks, system flushing. Such lost water does not reach the end consumers and is not even charged by the

water supply company. All of this is due to the "water crisis", which means that a large part of the population on Earth has no access to drinking water or the basic hygienic living conditions. According to the forecasts of various international organizations, it is estimated that by 2040 Earth will be left with no sufficient quantities of drinking water.

Water supply and sewerage are two cyclically connected infrastructures, as can be seen in Figure 1.

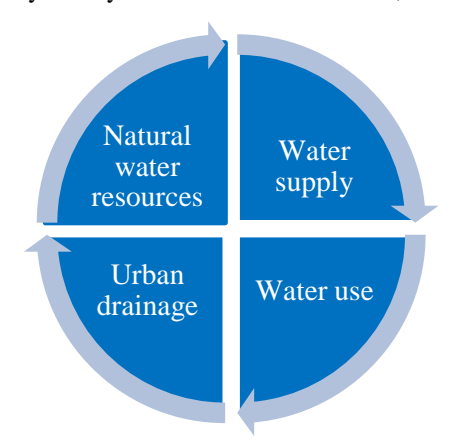


Figure 1. Connection of water supply and drainage

2. STUDY AREA

2.1. Republic of Croatia

The Republic of Croatia is situated in South-Eastern Europe, on the crossroads of Central Europe and the Mediterranean, stretching over 56,594 km² with the interior sea water and territorial sea area of 31,479 km² [1], [2], [3]. There are five neighbouring countries: Bosnia and Herzegovina, Slovenia, Hungary, Serbia and Montenegro [3]. According to the Köppen's classification, most of the Republic of Croatia has a moderately warm, rainy climate characterised by a mean monthly temperature ranging between -3 °C and +18 °C in the coldest month [2]. The capital of Croatia is Zagreb. Croatia has 4,456,096 inhabitants (according to 2011 census) [4]. Croatia has a total of 128 towns/cities and 6,757 settlements [2]. Also, there are in Croatia 1,620,002 house numbers and 53,096 streets [5].

2.2. Republic of Slovenia

The Republic of Slovenia is situated in Central and South-Eastern Europe, bordering Austria, Croatia, Hungary and Italy. The country has an area of approximately 20,271 km² and has a population of 2,094,060 [6], [7], [8]. According to the Köppen climate classification, most of Slovenia has a warm-temperate humid climate with the warmest month having a mean temperature below 22 °C and four or more months having a mean temperature above 10 °C. The climate of some coastal areas of Slovenia has a warm-temperate Mediterranean climate with the warmest month mean temperature being above 22 °C and humid conditions all year round [9]. The capital of Slovenia is Ljubljana. Slovenia has a total of 6,036 settlements [10]. In Slovenia, there are 558,160 house numbers and 10,400 streets [11].



Figure 2. Map of Republic of Croatia (left) and map of Republic of Slovenia (right) [12],[13]

For the purpose of clarity and easy comparison of the two analyzed countries, some of the aforementioned data are presented in Table 1.

Table 1. Basic information about Croatia and Slovenia [1], [2], [3], [4], [5], [6], [7], [8], [9], [10], [11]

Parameter	Croatia	Slovenia
Land area [km ²]	56,594	20,271
Population	4,456,096	2,094,060
Number of settlements	6,757	6,036
House numbers	1,620,002	558,160
Number of streets	53,096	10,400
Capital	Zagreb	Ljubljana
Number of neighbouring countries	(5+1 on sea)	4
Official script	Latin	Latin
Currency	Croatian Kuna (HRK)	Euro (EUR)
International telephone code	+ 385	+ 386

3. WATER SUPPLY AND SEWERAGE SYSTEM IN CROATIA

3.1. Water Supply

Croatia is a water-rich country split between two river basin districts, the Danube basin and the Adriatic basin. With around 24,495 m³ of renewable water per capita per year, Croatia is a water-rich country. Surface water quality is, however, a concern, particularly with respect to nutrient pollution in the Danube basin. Water supply comes mainly from groundwater (96%). Surface water provides 4% of overall drinking water supply. Most rivers flow into the Danube or one of its tributaries. Local governments are responsible for water and sanitation services and provide them through 156 public utility companies (140 for water and sanitation service and only 16 for sanitation service). Service quality in Croatia is generally very good by regional standards. Water service is continuous, and drinking water quality is mostly in compliance with national and European standards. The water supply network, which is 4 times as long as the wastewater network, is aging - most of it was installed more than 50 years ago - and its performance could be improved, since the leakage rate is as much as 40% [14].

Table 2. Basic characteristics of the water supply system (part of the analyzed data) [15]

Danamatan	Year						
Parameter	2014	2015	2016	2017	2018		
Total abstracted water (in 1000 m ³)	501188	508541	524063	505029	503503		
Total distributed water (in 1000 m ³)	307969	314906	307953	292908	302856		
Total water losses (in 1000 m ³)	193219	193635	216110	212121	200647		
Total length of water supply network (km)	42609	43104	44627	45603	45676		
Number of water connections	1247887	1245376	1245376	1245818	1257773		

Total length of sewerage network (km)

Number of sewerage connections

3.2. Sewerage System

Croatia has traditionally had a high level of service, with near-total access to piped water (99%) and flush toilets (95%). Croatian wastewater infrastructure needs upgrading. Among the 141 wastewater treatment facilities, 46% are equipped with preliminary and primary treatments, 51% with secondary treatment, and only 3% with tertiary treatment [14]. The typical sewerage system is mixed (faecal and precipitation waters together). Only a few smaller cities and residential districts of bigger towns have separate or split sewerage systems (faecal and precipitation waters are split) [16].

Downwoodow	Year					
Parameter	2014	2015	2016	2017	2018	
Discharge of wastewater (in 1000 m ³)	333353	327872	334790	312022	335807	

10493

521882

10885

555147

12047

568842

12448

584243

Table 3. Basic characteristics of the sewerage system (part of the analyzed data) [15]

9649

521882

4. WATER SUPPLY AND SEWERAGE SYSTEM IN SLOVENIA

4.1. Water Supply

Slovenia has good-quality and sufficient water resources. Eighty-one percent of the Slovenian territory belongs to the Black Sea basin, and the rest is part of the Adriatic Sea basin. With 15,411 m³ per capita per year, there are sufficient quantities of water on average in Slovenia, and most of it is in a good ecological state. However, agriculture has had a severe impact on groundwater quality, and there is a concern about the decreasing groundwater level in certain areas due to overabstraction. Drinking water supply relies almost exclusively on groundwater. Surface water is predominantly used for the production of electric energy in hydroelectric power stations, while groundwater provides 97% of the raw water for potable public supply. Local government units provide water and sanitation services through 98 utilities. Drinking water quality in Slovenia improved during 2004 to 2013 for both microbiological and chemical parameters. The compliance rate has steadily increased over the last decade to 92% in 2013. One-fourth of the Slovenian water network was installed before 1920. From 2000 to 2010, the rehabilitation of water supply systems was boosted by EU grants and funding specifically dedicated to water infrastructure improvement [17].

Table 4. Basic characteristics of the water supply system (part of the analyzed data) [18]

Parameter		Year					
Parameter	2014	2015	2016	2017	2018		
Total abstracted water (in 1000 m ³)	163095	164404	161821	169385	170718		
Total distributed water (in 1000 m ³)	117205	117886	116698	122559	121162		
Total water losses (in 1000 m ³)	45890	46517	45123	46827	49556		
Total length of water supply network (km)	24017	30923	31165	32519	32360		
Number of water connections	458305	439736	433305	444041	454487		

4.2. Sewerage System

Slovenians have full access to water services. Ninety-nine percent of the Slovenian population has access to piped water and flush toilets. Among the 486 water treatment plants, 72% rely on chlorine disinfection and 13% on mechanical and chemical treatment [17].

Table 5. Basic characteristics of the sewerage system (part of the analyzed data) [19]

Donomoton		Year					
Parameter	2014	2015	2016	2017	2018		
Discharge of wastewater (in 1000 m ³)	183285	162540	200653	217726	230638		
Total length of sewerage network (km)	8842	9638	8950	9664	9972		
Number of sewerage connections	266918	284120	268039	289680	296648		

5. RESULTS AND DISCUSSION

In this part of the paper, data on the water supply and sewerage system for the Republic of Croatia and the Republic of Slovenia for a 10-year period was analyzed. The period analyzed is from 2009 to 2018.

Table 6 shows some basic data on the water supply system and sewerage system for both countries.

Table 6. Basic data of the water supply and sewerage system

Parameter	Unit	Croatia	Slovenia
Average water losses per capita	m^3	51.01	23.67
Average water consumption per capita	m^3	78.47	57.86
Average abstracted water per capita	m^3	129.48	81.52
Average amount of wastewater per capita	m^3	67.95	110.14
Average water losses per one km of water mains	m^3	4392.83	1531.40
Average wastewater amount per one sewerage connection	m^3	574.77	777.48
Average water consumption per one water connection	m^3	240.79	266.60
Water supply network density	km/km ²	0.807	1.60
Sewerage network density	km/km ²	0.220	0.50

Programs MS Excel® and TIBCO Statistica TM were used to process the data. All the tables shown below are given in their original form and obtained from the TIBCO Statistica TM software package used for statistical data processing while for diagrams is used MS Excel.

Table 7 shows the descriptive statistics for the data on the water supply and sewerage system of the Republic of Croatia, while Table 8 shows the descriptive statistics for the data on the water supply and sewerage system of the Republic of Slovenia. Eight variables are observed as follows: Discharge of wastewater (m³), Total length of

sewerage network (km), Number of sewerage connections, Total abstracted water (m³), Total distributed water (m³), Total water losses (m³), Total length of water supply network (km) and Number of water connections.

Table 7. Descriptive statistics for the data on the water supply and sewerage system of the Republic of Croatia

	Descriptive Statistics (Croatia.sta)					
Variable	Valid N	Mean	Mnimum	Maximum	Std.Dev.	
Discharge of wastewater (m3)	10	324455200	301030000	343544000	14453256	
Total length of sewerage network (km)	10	9853	8144	12448	1557	
Number of sew erage connections	10	512320	435607	584243	47495	
Total abstracted water (m3)	10	537884400	501188000	576985000	32075086	
Total distributed water (m3)	10	330747900	292908000	365281000	27641139	
Total water losses (m3)	10	207136500	193219000	227293000	10630124	
Total length of water supply network (km)	10	43111	41246	45676	1619	
Number of water connections	10	1229711	1146088	1257773	33884	

Table 8. Descriptive statistics for the data on the water supply and sewerage system of the Republic of Slovenia

	Descriptive Statistics (Slovenia.sta)				
Variable	Valid N	Mean	Minimum	Maximum	Std.Dev.
Discharge of wastewater (m3)	10	186774700	151465000	230638000	25170598
Total length of sewerage network (km)	10	8620	7215	9972	957
Number of sewerage connections	10	263504	231243	296648	22502
Total abstracted water (m3)	10	165556400	161731000	170718000	3212054
Total distributed water (m3)	10	119326800	116698000	122559000	1958004
Total water losses (m3)	10	46229600	42352000	49556000	2309067
Total length of water supply network (km)	7	27899	21656	32519	4875
Number of water connections	7	450271	433305	466461	11620

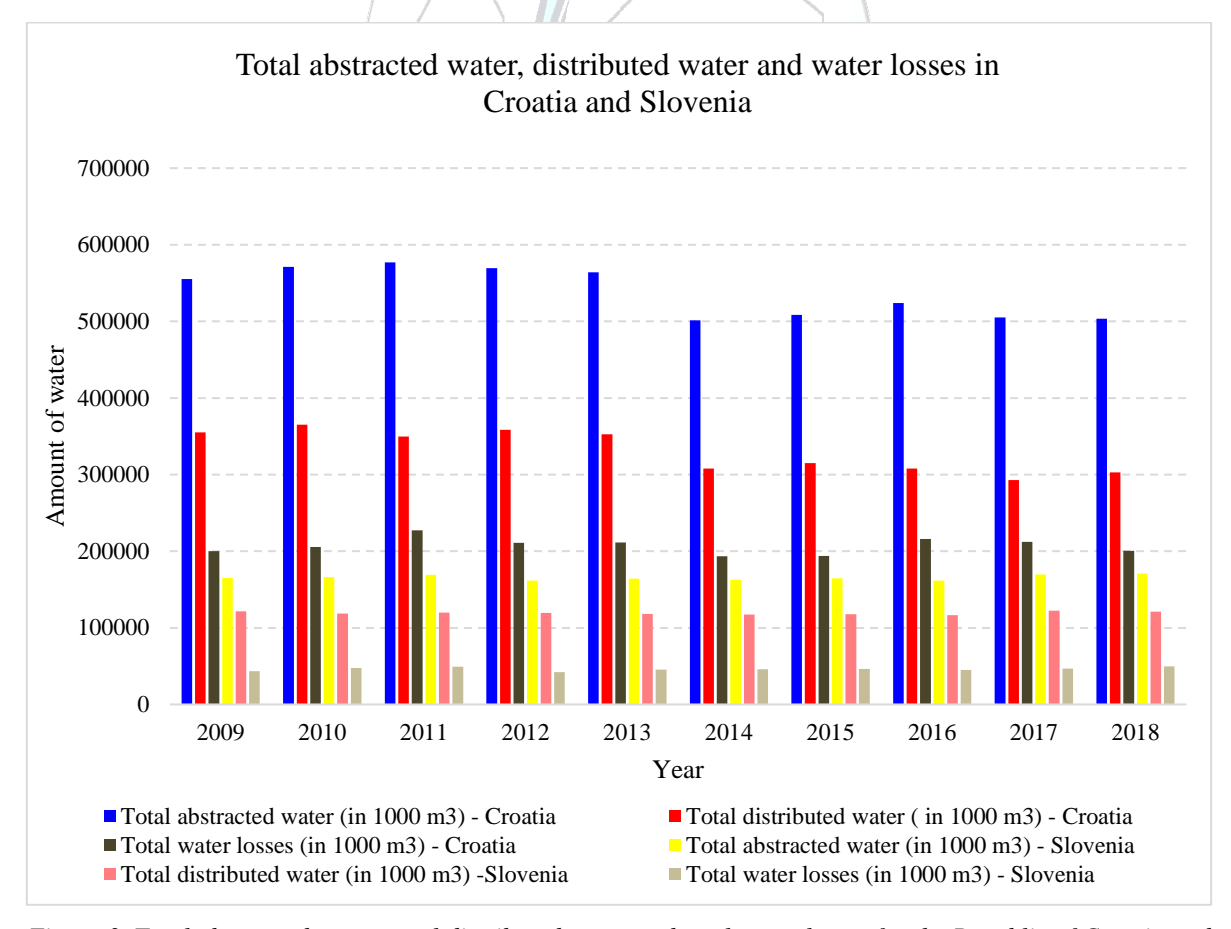


Figure 3. Total abstracted water, total distributed water and total water losses for the Republic of Croatia and Republic of Slovenia for a 10-year period

The following two tables (Tables 9 and 10) show the correlation coefficients for all the eight variables (five variables on the water supply system and three variables on the sewerage system) for the Republic of Croatia.

Table 9. Correlation coefficients for five variables of the data on the water supply of the Republic of Croatia

	Correlations (Croatia) Marked correlations are significant at p < ,05000 N=10 (Casewise deletion of missing data)						
Variable	Total abstracted water (m3) Total distributed water (m3) Total water losses (m3) Total length of water supply network (km) Number of water connections						
Number of water connections	-0,491906	-0,581819	0,028615	0,638773	1,000000		
Total length of water supply network (km)	-0,734558	-0,861877	0,024670	1,000000	0,638773		
Total water losses (m3)	0,553988	0,258278	1,000000	0,024670	0,028615		
Total distributed water (m3)	0,947360	1,000000	0,258278	-0,861877	-0,581819		
Total abstracted water (m3)	1,000000	0,947360	0,553988	-0,734558	-0,491906		

Table 9 shows the relationship between the Total Length of water supply network and: Total abstracted water (r = -0.734558), Total distributed water (r = -0.861877) and Number of water connections (r = 0.638773).

Table 10. Correlation coefficients for three variables of the data on the sewerage system of the Republic of Croatia

	Correlations (Croatia) Marked correlations are significant at p < ,05000 N=10 (Casewise deletion of missing data)			
V <i>a</i> riable	Discharge of wastewater (m3)	Total length of sewerage network (km)	Number of sewerage connections	
Discharge of wastewater (m3)	1,000000	0,319136	0,360549	
Total length of sewerage network (km)	0,319136	1,000000	0,964483	
Number of sewerage connections	0,360549	0,964483	1,000000	

Table 10 shows the relationship between the Total length of sewerage network and Number of sewerage connections (r= 0.964483).

Tables 11 and 12 show the correlation coefficients for all the eight variables (five variables on the water supply system and three variables on the sewerage system) for the Republic of Slovenia.

Table 11. Correlation coefficients for five variables of the data on the water supply of the Republic of Slovenia

Correlations (Slovenia)							
	Marked correlations are	significant at p < ,0500	0				
	N=7 (Casewise deletion						
	Total abstracted	Total abstracted Total distributed Total water losses Total length of Number of water					
	water (m3)	water (m3)	(mB)	water supply	connections		
Variable	` '	, ,	` '	network (km)			
Total abstracted water (m3)	1,000000	0,836563	0,837419	0,634198	-0,066432		
Total distributed water (m3)	0,836563	1,000000	0,401109	0,371276	0,172839		
Total water losses (m3)	0,837419	0,401109	1,000000	0,689979	-0,283524		
Total length of water supply network (km)	0,634198	0,371276	0,689979	1,000000	-0,756905		
Number of water connections	-0,066432	0,172839	-0,283524	-0,756905	1,000000		

Table 11 shows the relationship between the Total abstracted water and: Total distributed water (r = 0.836563) and Total water losses (r = 0.837419).

Table 12. Correlation coefficients for three variables of the data on the sewerage system of the Republic of Slovenia

	Cordedions (Soveria) Markedoomelations are significant at p<,05000 N=10 (Casevise obtetion of missing obta)		
	Discharge of wastewater (m3)	Total length of severage	Nuntoer of sewerage
Variable		network(km)	cornections
Discharged væstevæter (m3)	1,00000	0,621428	0,650735
Total length of severage network (km)	0,621428	1,000000	0,990051
Number of severage connections	0,650735	0,990.51	1,000000

Table 12 shows the relationship between the Discharge of wastewater and Number of sewerage connections (r= 0.650735), and between the Total length of sewerage network and Number of sewerage connections (r= 0.990051).

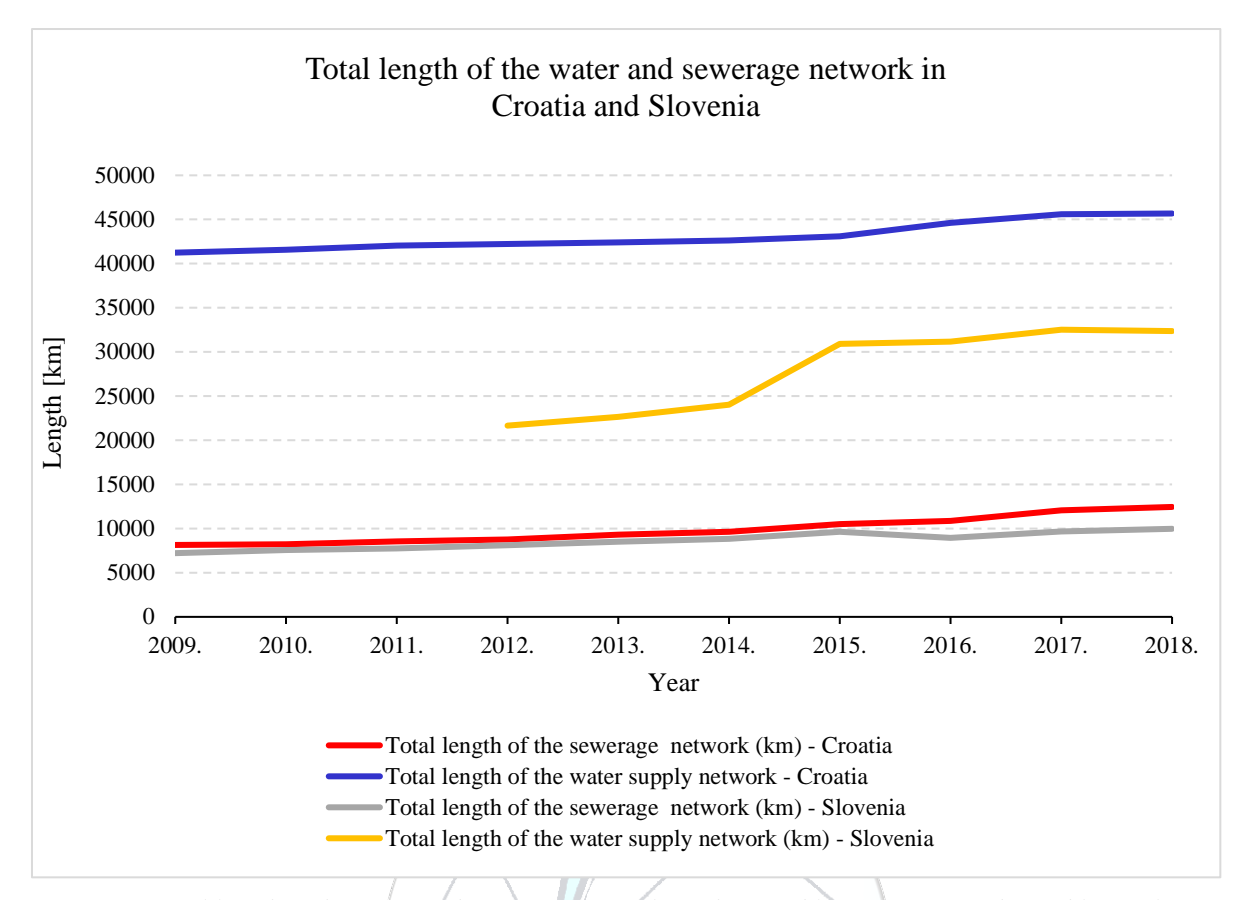


Figure 4. Total length of the water and sewerage network for the Republic of Croatia and Republic of Slovenia for a 10-year period

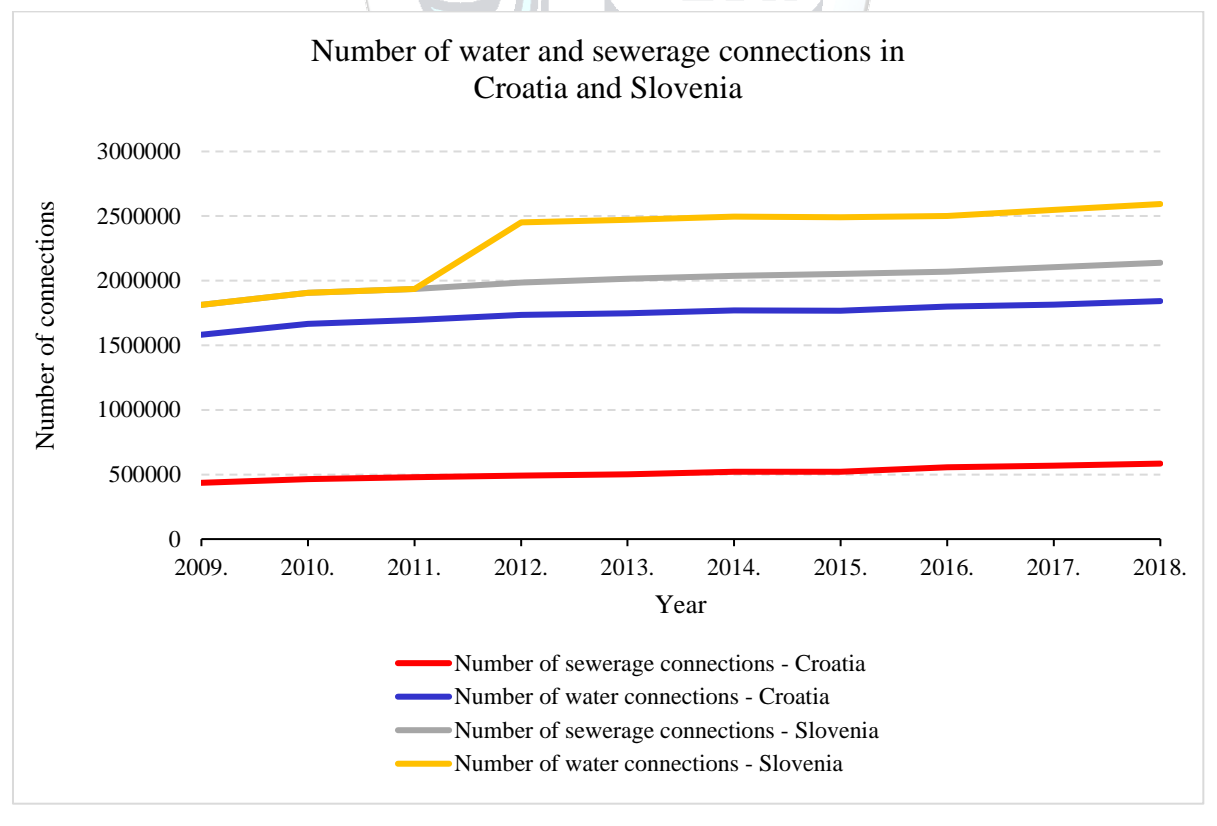


Figure 5. Number of water and sewerage connections for the Republic of Croatia and Republic of Slovenia for a 10-year period

6. CONCLUSIONS

By analyzing the correlation coefficients between individual parameters of water supply and sewerage, it can be concluded that the parameters with a correlation coefficient higher than 0.7 have a good connection or a significant mutual influence. For parameters between which the correlation coefficient is less than 0.7 we can say that the correlation is small or non-existent, i.e. that they do not have mutual influences.

All correlations between the water supply and sewerage system can be used in the development of the model and the calculation of a specific required data if we know some input data. The development of such models is a potential subject of future research. The construction, connection and condition of the water supply and sewerage network are of great importance for the development of each country. The main problems faced by all countries are water losses in the water supply, and the treatment and discharge of wastewater into the environment. Today, we are witnessing declining supplies of drinking water, and large-scale pollution of water and the environment from the discharge of untreated wastewater, and various diffuse sources of pollution. According to the EU Framework Directives (of which Croatia and Slovenia are members) it is necessary to achieve the maximum connection of the population to the water supply and sewerage network, reduce water losses to the limits of permitted losses, build wastewater treatment plants and connect all settlements up to a minimum of 2000 population equivalent, all with the aim of achieving a good water status and a sustainable water management. This paper shows that in Croatia and Slovenia the connection to the water supply and sewerage system is satisfactory. However, it is working on a higher percentage of construction and connection to the networks. Water losses in the water supply system are high in both countries, as a result of the age of the network, inadequate maintenance, failures and damage. In Croatia, an additional problem for water supply and sewerage is a large number of small settlements with less than 500 population equivalent for which it is economically unprofitable to bring sanitary infrastructure. These settlements have water supply from local wells, and wastewater is collected in septic tanks that are water permeable and represent sources of diffuse pollution.

REFERENCES

- [1]. Croatian National Tourist Board, Tourist Information, Full of stories, 2019., https://www.htz.hr/en-GB
- [2]. Croatian Bureau of Statistics, Statistical Yearbook of the Republic of Croatia, Zagreb, December 2018., https://www.dzs.hr/Hrv_Eng/ljetopis/2018/sljh2018.pdf
- [3]. Agency for Mobility and EU Programmes, A Foreign Researcher's Guide to Croatia, 5th Edition, 2019., https://www.euraxess.hr/croatia/news-events/foreign-researchers-guide-croatia
- [4]. (2013) Croatian Bureau of Statistics. [Online]. Available: https://www.dzs.hr/default.htm
- [5]. Croatian Bureau of Statistics. Croatia in figures 2018, Zagreb, 2018., https://www.dzs.hr/Hrv Eng/CroInFig/croinfig 2018.pdf
- [6]. (2020) Slovenia Consulate of the Republic of Slovenia in Norway. [Online]. Available: http://www.slovenia.no/EN/about-slovenia.php
- [7]. [7]. Republic of Slovenia, Statistical Office. Spremembe v površini Slovenije, dopis, 2018., https://www.stat.si/StatWeb/File/DocSysFile/10033/Spremembe_povrsine_Slovenije.pdf
- [8]. (2019) Republic of Slovenia, Statistical Office. [Online]. Available: https://www.stat.si/StatWeb/en/Field/Index/17
- [9]. (2020) Weather Online. [Online]. Available: https://www.weatheronline.co.uk/reports/climate/Slovenia.htm
- [10]. (2017) Republic of Slovenia, Statistical Office. [Online]. Available: https://stat.si/StatWeb/en/News/Index/6452
- [11]. (2020) Republic of Slovenia, Statistical Office. [Online]. Available: https://pxweb.stat.si/SiStatDb/pxweb/sl/50_Arhiv/50_Arhiv_02_upravna_razdelitev_02148_terit_enote/0214809S.px/table/tableViewLayout2/
- [12]. (2020) Encyclopaedia Brittanica. [Online]. Available: https://www.britannica.com/place/Croatia/People
- [13]. (2020) Encyclopaedia Brittanica. [Online]. Available: https://www.britannica.com/place/Slovenia
- [14]. The World Bank / IAWD Danube Water Program, Croatia country note, A State of the Sector, May 2015. Available: https://sos.danubis.org/files/File/country_notes_pdf/SoS_Croatia.pdf
- [15]. (2020) Croatian Bureau of Statistics Republic of Croatia. [Online]. Available: https://www.dzs.hr/default_e.htm
- [16]. L. Matković, Waste and Water Management in Croatia, Zagreb: Embassy of Belgium in Croatia, Commercial Section, 2015.
- [17]. The World Bank / IAWD Danube Water Program. Slovenia country note, A State of the Sector, May 2015. Available: https://sos.danubis.org/files/File/country notes pdf/SoS_Slovenia.pdf

- [18]. (2020) Republic of Slovenia, Statistical Office. [Online]. Available: https://pxweb.stat.si/SiStatDb/pxweb/sl/30 Okolje/30 Okolje 27 okolje 03 27193 voda 01 27501 ja vni_vodovod/?tablelist=true
- [19]. (2020) Republic of Slovenia, Statistical Office. [Online]. Available: https://pxweb.stat.si/SiStatDb/pxweb/sl/30 Okolje/30 Okolje 27 okolje 03 27193 voda 02 27502 ja vna kanalizacija/?tablelist=true



Smart Scale IoT Application

Radosveta Sokullu¹

¹ Corresponding author: Ege University, Department of Electrical and Electronics Engineering, 35100, Bornova/Izmır, Turkey. radosveta.sokullu@ege.edu.tr

Abstract

The use of electronic and communication devices in homes, factories, cars and many other sectors are increasing day by day, helping us to create a more environment friendly world. There is a growing demand to manage and analyze the collected data in a simple way. Many devices around us are turned into "smart devices". This concept implies that the devices can collect data in a controlled manner, save it and transmit it to other devices either automatically or with minimal human control and minimal effect on the environment. The "Internet of Things" (IoT) has emerged as a new technology which allows devices to connect to a network through various protocols and communicate with each other over wide area networks. Thus the need to collect and analyze the data in a more manageable way has become an important research issue. This paper describes the work for creating a smart scale that can be incorporated in various healthcare, home and industrial IoT systems. The developed prototype system allows transferring weight data, provided from smart sensors, to a data center using the MQTT protocol via ESP32. The user will be able to access the information in the data center from his mobile device or personal computer and follow up and/or analyze the data. A user interface was developed for Android based devices using the Android Studio. The project ensures full integration between the MQTT applications and the Android Studio using the Eclipse-Paho library. The prototype system can find usage in various areas, from personal health, to environmental and industrial sectors. Results from the smart scale can be transmitted electronically, integrated in public healthcare systems, environment monitoring systems and industrial applications.

Key words

Internet of Things, smart devices, smart scale, MQTT

1. INTRODUCTION

The use and communication of electronic devices in homes, factories, cars and many sectors are increasing day by day. For this reason, there is lot of theoretical and application research going on currently both in the academia and the industrial world. The Internet of Things (IoT) has emerged as the new technology that allows to connect and operate various devices over long distances with minimal or no human intervention for the purpose of collecting and evaluating data and when required carry out actuation of specific operations. The IoT technology has penetrated in different areas of our lives, starting from smart homes, smart appliances, smart traffic, and smart agriculture to smart vital signs collecting systems and industrial applications. Data collected over the IoT can be used in many diverse ways – from personal look-up applications, to vast data analytics systems. The work presented here addresses the issue of collecting weight measurement data and transmitting it over the IoT to be used for personal record tracking. The paper describes the design and prototype of a smart food weighing system created using the internet based technologies. This so called "Smart Scale" will transfer weight sensor data via ESP32 to a data center using the MQTT protocol. The user will be able to access the information in the data center from his mobile

device or personal computer and analyze the data. In this way, he will be able to determine the daily nutritional requirements and also remotely monitor the amount of food remaining in stock. From here on the paper is organized as follows: in the following section a short overview of some related work is presented. In section 3 the proposed system architecture and main components are described followed by user interface design, evaluation and conclusion.

2. RELATED WORK

An interesting study utilizing a smart weighing system is presented in [1] where the authors use a wireless weighing platform, comprising the latest advances in low power wireless sensor network technology, to better understand the condition of the colony in beehives. One of the main measures of the strength of a beehive is the weight of the colony. Changes in weight can accurately reflect the productivity of the colony. The installed system is able to scale the measurement linearly and has been found successful in terms of energy consumption. A farming related smart scale system is presented in [2]. The authors consider the case of collecting rubber from various small farmers in Malaysia. In the traditional practices, each farmer brings his load, which is weighted and recorded in a logbook manually. However, this practice is very prone to human errors and in many cases physical records are lost. So the authors propose the so called "Smart Rubber Scale" (SRS) System which utilizes cloud storage to ensure long term preservation and accessibility of the data. The SRS prototype consist of load cell sensor, scale sensor, Arduino UNO R3, sensor module HX711, Bluetooth module and an LCD display. A dedicated SRS website is developed by using PHP that allows the staff to automatically store rubber weight information automatically after measurements are taken. Both the farmer and the staff have access to the uploaded data and also detailed monthly records can be downloaded. Another system which presents an example of a smart IoT based personal system is presented in [3]. It describes the design of an IoT application aimed at storing personal vital signs information in a cloud. It provides a possibility to access and evaluate the data via a mobile application. In this process, the data collected from the patient with an embedded sensor device installed with the STM32 card and is then transmitted to a predefined database over the internet. An MQTT based cloud system is used. The saved data can be accessed and processed individually using a custom designed Android based application. As a result, a system with very low power consumption and low latency is designed. More details on how security issues in this type of applications can be handled are to be found in [4]. The work discusses the secure communication model for embedded devices over the Internet of Things (IoT). The goal is to examine innovations in the application layer together with the widely used MQTT protocol to provide secure communication. The basic idea is that the MQTT protocol enrolls using a username and password. In order to prevent this information from being captured by third parties during communication, a modified application logic and unnecessary encryption method is used. With this method, the risk could be partially compensated. In [5] the authors present a remote controlled dog feeding mechanism with changeable and adaptable characteristics. The proposed prototype system allows dog owners to take care of their dogs without interrupting their daily routines. At the same time it provides a good record of the feeding practices over a given period of time by determining the stock information, feeding frequency and consumption. The prototype uses a load cell for remote weight measurement, an Android application and a RFID for realizing control operations. When the feeding process is completed a message is sent remotely providing information about the time and details of the feeding. An example of a system using the ESP32 module for wirelessly transmitting locally collected data is presented in [6]. The authors' aim is to create an application related to smart grid technology. The proposed solution allows transmitting and controlling electrical energy consumption by using a smart meter. Thus, the service provider and the consumer are able to obtain information about energy consumption at certain time intervals. The data measured locally is broadcast to an MQTT server with the help of a ESP32 module. Users have the possibility to access their personal recorded information whenever they want via the web over this MQTT server. This is an attractive application, which deploys an IoT network and makes it quite easy to keep track of our electricity consumption intelligently.

30 Sokullu

3. PROPOSED SYSTEM ARCHITECTURE AND MAJOT COMPONENTS

3.1. System Architecture

The proposed prototype comprises an IoT smart scale which can collect weight data from a smart load cell and transfer it through an wireless unit to a MQTT server. The functional diagram of the developed prototype is presented in Fig.1 below.



Figure 1. System Architecture

As can be seen from the figure the architecture of the proposed system contains a load cell, an HX711, a wireless transmission module ESP32 for collecting and transmitting the weight data; a cloud server to store the information and an Android based user application which allows access and evaluation of the recorded data. An LCD screen to provide user input when required.

3.2. Major Components

In this section the main components of the proposed system are discussed.

3.2.1. Smart Weighing Module

The smart weighing module is based on a load cell with HX711 shown in Figure 2. Measurement of the weight is done using load cell sensors, which convert the force acting on the load cell into a signal. This signal can be a change in voltage, current or frequency depending on the type of load cell and circuit. Thanks to the strain-gauge structure inside the two 5 kg load cells used in this work, an analog signal is generated by the difference in resistance caused by the load on it. This signal is transferred to the HX711, which is on a 24-bit ADC module. The E+ and E- inputs of the load cells are connected to the E+ and E- input of the HX711 by mapping. The red ends of the mutual load cells are connected to the E+ and E- inputs of the HX711, providing the combined use of load cells.

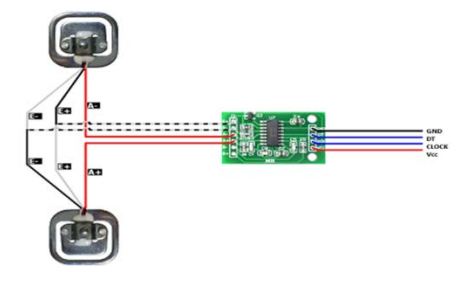


Figure 2. Load Cell with HX711 connection

3.2.2. The ESP32 Module

ESP32 is a microcontroller with a 240 MHZ clock frequency, a programmable WiFi receiver/transmitter with embedded power amplifier, filter and antenna, and is frequently used in IoT applications. It contains peripherals such as I2C, SPI, UART, and can be programmed with Arduino or MicroPython IDEs. ESP32 can be operated over protocols such as TCP, HTTP, MQTT, SNTP. In this prototype, the data from the HX711 is transferred digitally from the data end to the ESP32 with a specific clock frequency. The data is processed by using the "HX711.h" library in ESP32. Thus, the weight data measured from the load cell module is ready to be transferred to the server for use. After the user selects the product, the product information from the LCD keypad is transferred to the MQTT server along with the weight data. The ESP32 is defined to the MQTT server as a publisher. The ESP32 is connected to a WiFi network using the predetermined SSID and password information. Open source Cloud MQTT was chosen as the MQTT server.

3.2.3. The MQTT Module

MQTT is a machine-to-machine (M2M) protocol, one of the most widely used protocols for IoT. It provides a messaging network based on the publish/subscribe principle. The protocol works over TCP/IP, but any lossless, double-sided network protocol will work. It operates with limited data rate and is especially suited for IoT applications, which require low data rate and small data volumes. There are 2 main entities in the MQTT protocol: a MQTT server and a certain number of MQTT clients connected to it. The MQTT server receives messages from all clients and directs them to the addresses to be reached (clients). An MQTT device connects the server to the network and compiles the MOTT library. The MOTT packet consists of a header and message part. The messages are listed under headings. If a title appears on the server and there is no subscriber under this title, the server deletes it. "Publisher" is an MQTT client that sends a message to the server. "Subscriber" is an MQTT client that can view or use the messages under the header by registering for the title sent by the publisher. Three types of MQTT messages are used: Connect, Disconnect and Publish. The connect message is used for establishing the connection between the server and the units; the disconnect message causes the disconnection; publish message is the MQTT client request message. As shown in Figure 4, subscriber devices can reach the server and at the same time publish messages on the server as a "publisher", register in the headers and send messages under the header. MQTT applications use a microcontroller as a "publisher" to save the data it receives.

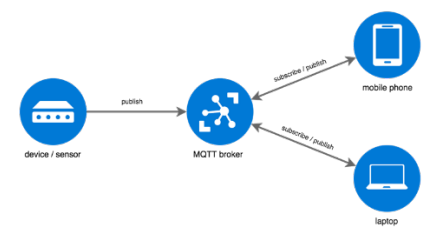


Figure 3. MQTT Protocol Operation

ESP32 is one of the most used and most suitable microcontrollers for this purpose. Devices connected to the server as "subscriber" are devices that provide the data to the user with applications installed on operating systems such as Android, IOS, Windows, usually from sensors. In the project created, a solution was produced for Android devices using Android Studio. The use of Eclipse-Paho library, where MQTT applications are executed for Android Studio, and its integration into the project has been provided.

3.3. System software

Eclipse-Paho library is used for the MQTT protocol in Android programming. A publisher/server application is developed with Java in Eclipse-Paho library. Each interface page for Android

32 Sokullu

consists of activities. Abstract operations are done with the help a similar interface. Interfaces define functions in a way that we can "override". Helper Java classes can also be created for use in activities that execute the interface. For example, MainActivity, AfterLogInActivity, ProgressActivity used in this prototype are examples of activities; AppDatabase, MyAdapter, MqttHelper are examples of Java helper classes. The Android programming was carried out in Java. The interface that welcomes the user when the application is opened is the interface where the user will register, i.e. MainActivity. The classes User, User Alme and AppDatabase, which are connected to the MainActivity, are the classes that perform the operations on the local database to store the information that the user has registered. The User class determines the user's variables, such as email, password, name and surname that the user must save in the system. AppDatabase is the class in which the connection configurations of the database are made. Android Room Database is used as the database.

The main algorithm is given in Figure 4 below. After the user registers with their profile information, they are directed to ProressActivity. ProgressActivity is an activity that offers the user a welcome screen with their first and last name. In ProgressActivity, the name and surname information given by the user while registering to the system is taken from the Room Database (a local database in Android). Following the input of the user's name and surname, a special welcome screen is activated for the user followed by direction to the AfterLogInActivity. MQTT messages are displayed sequentially in AfterLogInActivity. There is a RecyclerView library in this class that allows the functions and messages that receive MQTT messages to be displayed sequentially. The class that allows RecyclerView to connect to the activity is the MyAdapter class. In addition, each message is set up with CardView to print a cloud icon and message. The class in which MQTT functions are defined is the MqttHelper class. The MqttHelper allows integration of MQTT operations and defines the actions to be taken when the message is received.

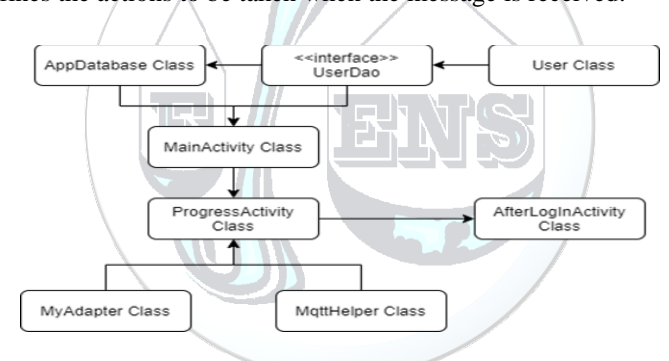


Figure 5. The main algorithm

4. USER INTERFACE DESIGN

An important part of the design is the user interface. The first screen on the LCD that meets the user is given in Figure 5 below and shows the message "Welcome, Press a Key".



Figure 5. The Welcome LCD screen

After connecting to the server, the system offers the user the opportunity to choose a product. While the user selects the desired product by pressing the keys, the scale measures the weight of the product. Each time the user presses a key, the weight data from the scale is updated. Thus, when there is a new user, or the user wants to change the weight, he will be able to weigh the product again and save it to the system with new data. An example regarding the product information and the sensitivity of the scale is shown in Figure.6.



Figure 6. An Example of Weighing a Milk Carton

After the product selection and weighing process is completed, the information on the screen is sent to the MQTT server as soon as the user presses the "Select" button. Thus, it is connected to the MQTT server as "Publisher" with ESP32. When the user connects to the server as a "Subscriber" from any Android device, they can view the messages under the "topic" on their device. The mobile device software was developed using Android studio. Examples of the design can be seen in Figure 7 below.

5. PRELIMINARY RESULTS AND DISCUSSION

The work described in this paper is part of an ongoing project for creating a user-friendly home environment. The described prototype has been tested as a standalone system and the results are presented below. Experiments regarding the input interface and weighing sensitivity of the scale have been developed. Two groups of tests were carried out: the first was testing the connectivity of the system and the proper operation of software. Examples of the user screens at the stage where the user is greeted on the Android device and the profile information is saved to the system are given in Figure 7 below. The second group of tests regarded the measuring systems. The load cellbased system was calibrated and tested with various samples of goods. For a 1.5 lt water bottle it was observed that the weight measurement was had a deviation of 6.25%; in the tests performed with 1 kg tea package, weight measurements were obtained without error; tests performed with a 300 gram snack package showed a deviation of 3.44%. The average error was estimated at below 2.6%. Compared to other similar systems like the ones presented in references [1], [2] and [5] these results are acceptable. The system has met the requirements and smoothly operates over the provided wireless environment. Privacy and protection of the data is secured by the login requiring registration, username and password. Since the goal was to create a simple, low cost prototype using off-the-shelf elements no further protection mechanisms were incorporated.

34 Sokullu





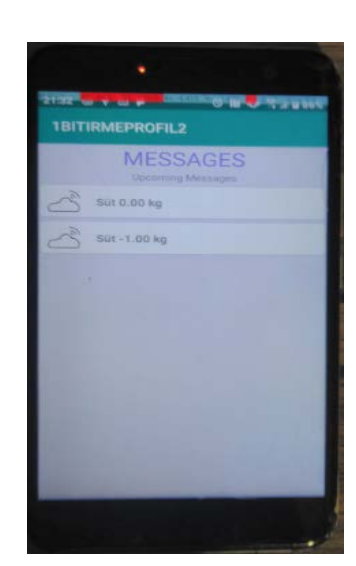


Figure 7. Examples of user interface screens

6. CONCLUSION

In this paper we have discussed the proposed prototype and main components for an IoT based smart scale application. The user has been provided with easy access to food weight information. ESP32 was chosen as the microcontroller, and the weight data received from the load-cells were stored on Cloud MQTT servers using the MQTT protocol along with the product information from the LCD keypad. The data on this server can be accessed through the application developed for Android devices. The designed prototype had in mind a personal food tracking information system, as part of a smart environment project, but with small modifications it can be used in other situations including also industrial weighing applications

ACKNOWLEDGMENTS

The authors would like to thank Eyüp Fatih Ersoy and Ata Durak for their contributions.

REFERENCES

- [1]. D. W. Fitzgerald, F. E. Murphy, W. M.D. Wright, P. M. Whelan, E. M. Popovici, "Design and Development of a Smart Weighing Scale for Beehive Monitoring", 26th Irish Signals and Systems Conference, ISSC 2015, 21 July 2015 DOI: 10.1109/ISSC.2015.7163763
- [2]. N.S.N. Ismail, N; S.Z.B. Mustafa, F. Yunus, N.B.A. Warif, Internet of Things Smart Rubber Scale System Using Arduino Platform In Proc.: 2020 IEEE International Conference on Automatic Control and Intelligent Systems (I2CACIS) pp.45-50, Shah Alam, Malaysia, June 2020
- [3]. D. Yi, F. Binwen, K. Xiaoming, M. Qianqian, "Design and Implementation of Mobile Health Monitoring System based on MQTT Protocol", IEEE Advanced Information Management, Communicates, Electronic and Automation Control Conference (IMCEC), pp.1679-1682 Harbin, Oct, 2016
- [4]. P. Peniak, M. Franeková, "Extended Model of Secure Communication for Embedded Systems with IoT and MQTT", International Conference on Applied Electronics, 19 October 2018, DOI: 10.23919/AE.2018.8501434, 2018
- [5]. V. K. Karyono, H. T. Nugroho, "Smart Dog Feeder Design Using Wireless Communication, MQTT and Android Client", In Proc. 2016 International Conference on Computer, Control, Informatics and its Applications: Recent Progress in Computer, Control, and Informatics for Data Science, IC3INA 2016, , pp191-196, February 2017
- [6]. R. K. Kodali, S. Sahu, "MQTT Based Smart Metering", Proceedings of the 2nd International Conference on Green Computing and Internet of Things, ICGCIoT 2018, August 2018, pp.399-402. DOI: 10.1109/ICGCIoT.2018.8753052
- [7]. MQTT website. [Omline]. Available: http://mqtt.org/

IoT Based Forest Fire Monitoring System

Radosveta Sokullu¹

¹ Corresponding author: Ege University, Department of Electrical and Electronics Engineering, 35100, Bornova/Izmɪr, Turkey. radosveta.sokullu@ege.edu.tr

Abstract

This paper describes a prototype system for monitoring forest fire using IoT and drones. Sensors placed in the forest area continuously measure parameters, which can provide early warning about arising fire situations such as temperature, humidity, carbon monoxide and simultaneously transfer the data for processing to a control unit. The control unit aggregates and maps the collected information separately for each parameter and then creates fire mapping based on the FFDI index including all parameters. The severity of the situation is reflected on the map using a special coloring scheme. When a certain color level is exceeded, a drone (possibly carrying water supplies) is sent to the transmitted coordinates to provide visual data and help extinguish the fire at as early stage as possible. The wireless sensor network consists of small size sensors, cheap off-the-shelf nodes placed in the environment to interact with the physical world. These nodes autonomously cooperate in the physical area and provide information about the current surrounding environment over LAN and WAN. Since these devices can easily be damaged and need to be replaced, they are intentionally selected to be very cheap with little processing ability. The functions of integrating and evaluating the collected data are embedded in the control unit, which is located at a safe distance within communication range. The communication between the control unit and the drone is over WAN. The drone would normally be waiting ready in a monitoring station or fire fighter location. Upon receiving critical information the drone can be dispatched to collect visual data of the area and/or if possible to help with extinguishing the

Key words

Internet of Things, smart devices, forest fire detection, FDDI index

1. INTRODUCTION

One of the first areas where wireless sensor networks and Internet of Things have found application is environment monitoring. In the early stages WSN were custom-designed to provide early warning about possible forest fires. With the development of infrastructure and the standardization of new low cost wireless connectivity protocols, the Internet of Things (IoT) established itself as the main technology in many applications, like environmental monitoring, agriculture, industry etc. From smart homes, smart appliances, smart traffic, and smart agriculture to smart vital signs collecting systems and industrial applications IoT has become a ubiquitous technology. The paper describes the design of a system for monitoring forest fire using IoT and drones. Sensors placed in the forest area continuously measure parameters, which can provide early warning about arising fire situations such as temperature, humidity, carbon monoxide and simultaneously transfer the data for processing to a control unit. The control unit aggregates and maps the collected information separately for each parameter and

36 Sokullu

then creates fire mapping based on the FFDI index including all parameters. When a certain color level is exceeded, a drone (possibly carrying water supplies) is sent to the transmitted coordinates to provide visual data and help extinguish the fire at as early stage as possible. From here on the paper is organized as follows: in the next section a short overview of some related work is presented. In section 3 the theoretical background on forest fire indices and fire danger calculations is provided. Section 4 presents the system architecture and main components followed by user interface design, evaluation and conclusion.

2. RELATED WORK

In the last decade, together with rising temperatures and unstable weather conditions causing draughts and excessive flooding the number of forest fires all over the world has increased considerable. Incurred forestation destruction, wildlife loss and environmental calamities are becoming more sizeable every year. Studies show that the fires contribute to the rise of global temperatures and negatively affect climate change. [3,4]. That is why there are a lot of work focusing on monitoring, preventing and detecting forest fires. Depending on the adopted approach research can roughly be divided into 3 groups: based on WSN; using images and image processing techniques; using unmanned aerial vehicles (UAVs).

An interesting study covering the use of WSN and a small satellite to provide early warning about forest fire is presented [1]. The authors describe a WSN for collecting data about temperature, smoke and CO2 which is transmitted over wireless medium to the small satellite which re-transmits the data to a ground station where they are analyzed. The proposed prototype comprises a set of sensors, a transmission module, a microcontroller with an LCD and a remote control unit. The authors in [2] address the problem faced by wildlife and forest departments due to the reduced forest areas and the increased movement of wild animals into residential areas. The work proposes a system for tracking animals and alarming the responsible authorities to protect both animals and forests against forest fires. A fire detector using Arduino UNO is designed which is interfaced with a temperature sensor, a smoke sensor and a buzzer. Whenever a fire occurs, the system automatically senses and alerts the user by sending an alert to an app installed a mobile or webpage accessible through the internet. A detailed overview of using artificial neural networks to help in early forest fire warning systems is provided in [3]. The authors define three phases in the development of forest fires: pre-fire when action for controlling the occurrence of fire control can be taken; during arising fire, when early detection and appropriate action is required; post-fire when damage assessment and mitigation planning is done. In many countries satellite-based surveillance system are used to detect forest fire but this approach is usually used when fire has already spread over a large area. The authors propose a model for early fire detection and prediction. Besides Raspberry Pi microcontroller and required sensors the system comprises a centralized server, used for storing the data and analyzing that data. Feed-forward fully connected NN is used for prediction purpose. In [4] the authors present two solutions for early fire detection systems based on emerging new technologies; unmanned aerial vehicles (UAVs) with specialized cameras and LoRaWAN sensor networks. Different scenarios for the possible use of the drones in such cases are presented and analyzed. An interesting angle to detecting forest fire at an early stage using image processing and color schemes is proposed in [5]. The work classifies the characteristic color of the forest fire using image processing techniques. The authors argue that especially during the late spring and summer when the fire is easily distinguished from the color of trees and foliage and suggest a new method which combines several predetermined and fuzzy criteria for image segmentation. Another approach that has emerged in recent years is based on incorporating drones. Such options provide lower operational costs and allow UAVs to reach areas that are inaccessible or considered too dangerous for firefighters. The work in [6] describes the application of a real-time forest fire detection algorithm using aerial images captured by a video camera onboard an UAV. The forest fire detection algorithm consists of a rule-based color model that uses both RGB and YCbCr colour spaces to identify fire pixels. A fire geolocation algorithm is proposed to estimate the location of the fire and transmit the location in terms of latitude (φ), longitude (λ) and altitude (h).

Different than the research presented above, in this work the fire detection is done based on a combination of sensing data, color-scale map using the FDDI index and coordinate determination for drone dispatch. A large number of sensors are used to collect data which is then aggregated and processed by a remote control unit to produce a map of the area with colors depending on the possibility of fire occurrence. Location information is also extracted and a UAV can be sent to the endangered area.

3. FOREST FIRE DANGER ESTIMATION AND DETECTION

Forest fires all over the world cause a lot of damage to the wildlife habitat and human population. During the years various methods have been developed for detecting forest fires at an early stage and also evaluating the

danger of their occurrence. Scientists have proposed various indices which take into consideration parameters from the surrounding environment to evaluate the possibility of fire ignition.

One of the most popular indices is the McArthur Fire Danger Index (FDI), which was proposed by McArthur in 1966. [7] [8] The FDI is a measure of fire initiation, spreading speed and also evaluates how difficult it is to contain it at the source. Later on it has been extended it to include other environmental parameters like temperature, relative humidity, wind direction, vegetation type and terrain characteristics. Noble in 1980 proposed a detailed equation form of the index. [9] Besides this index, which has been operational in Australia since 1967, the number 1 country in danger of forest and bushfires, other indices are also used. Examples include the Canadian Fire Weather Index (FWI) [10], the American National Fire Danger Rating System (NFDRS) [11], Nesterov index [12], Angstro'm index [13].

Today many countries use the FFDI (Forest Fire Danger Index) and GFDI (Grasland Fire Danger Index) which also include the draught factor (DF). The DF, provides an estimation of the vegetation fuel available for burning and has values in the range 1-10, where a DF = 10 indicates maximum possible fuel available for combustion. In their centennial paper [14] John J. Keetch and George M. Byram formulated the Drought index (DI) drought index, which expresses moisture deficiency in hundredths of an inch and the index is based on 8.00 inches of water available for transpiration, so the index ranges from 0 to 800. It can be computed for a given level of mean annual rainfall. Since there were no computers at that time, the authors developed detailed tables and recording examples (Fig. 1) for deriving the correct value of DI.

		sample Agency		ample Istrict		mple tion	June Month	1966 Year	
	Day of the Month	24-Hour Rainfall (measured amount)	Net Rainfall (adjusted amount see instructions)	Air Temperature maximum temp. X dry-bulb temp.	Drought Index yesterday, or as reduced by net rainfall (col. 3)	Drought Factor From Table	Drought Index For Today col. 5 plus col. 6	Current Stage of Drought	
- ,	1	2	3	4	5	_6	7	8	١.
-/:	1		0	79	164	10	174-		١.
/	2		0	75	174	. 8	152	1	1 \
/	. 3.	0.66	.+6	70	136	6	142		١ ١
/ /	14			76	142	9	151	1	
	5	0.23	.03	79	148	ii	159		
			0	84	159	14	/ 73		
	7	0.16		65	/ 7.3	4	177		
	9	112	75	"	7.7	71	1	((

Figure 1 – Drought Index Sample Record (1968)

An ongoing EU funded project, the High-End cLimate Impacts and eXtremes (HELIX) project, which started in 2014, is a collaborative research work of 16 organizations worldwide assessing the potential impacts of climate change. [15] Scientists work together to develop future scenarios of the natural and human world as a consequence of global warming. Using the McArthur and Keetch-Byram indices as well as the Noble equations they have summarized the following fire index calculations and values for the FFDI:

$$FFDI = 1.25 * D * exp [(T - H)/30.0 + 0.0234 * V]$$
 (1)

where D is the drought factor, T is the temperature (°C), H is the humidity (%), and V is the wind speed (km/h). The DF is calculated using Eq. 2:

$$D = (0.191 * (I + 104) * (N + 1)^{1.5}) / (3.52 * (N + 1)^{1.5} + P - 1)$$
(2)

where P is the precipitation in mm/day, N is the number of days since last rain, and I is the Keetch-Byram drought index.

4. PROPOSED SYSTEM AND MAJOR COMPONENTS

4.1. System Architecture

In this study a fire warning and detection system is presented incorporating three major modules. The first is the WSN, which provides sensor data from the environment; the second is the FFDI calculation and color mapping; the third is coordinate determination and drone dispatch (if required). The general system architecture is presented in Fig.2 below. Sensor nodes transmit through a gateway (also serving as an aggregating and control unit) over a TCP connection to a server where users can login to view and download the information.

38 Sokullu

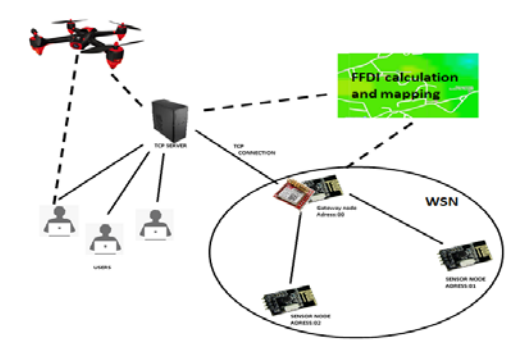


Figure 1. System Architecture

Data collected from the sensor nodes is used in the calculation of the FFDI. Based on the specific temperature, humidity etc. values a mapping is done to a color-scale map. The collected data is also used for determining the local coordinates.

4.2. Major Components

In this section the main components of the proposed system are discussed.

4.2.1. The sensor node

The wireless node and its components are shown in Figure 2. The DHT-11 is the temperature and humidity sensor, MQ-7 is CO2 sensor, connected to an Arduino Nano processor, nrf24l01 wireless module transmission module and the power supply.

The DHT-11 is a common temperature and humidity sensor used in embedded projects. The temperature range is from 0 to 50 degrees Celsius with an accuracy of + -2 degrees. The humidity range is between 20 and 80 percent with an accuracy of 5 percent. DHT11 operates with extremely reliable technology and thus ensures high stability. It is small, inexpensive and easy to use. This sensor is also used in weather stations to measure atmospheric temperature and humidity.

The sensitive material of the MQ-7 gas sensor is SnO_2 with lower conductivity in fresh air. It adjusts by high and low temperature cycle method and detects CO at low temperature (heated by 1.5V). The conductivity of the sensor becomes higher with increasing gas concentration. MQ-7 gas sensor has high sensitivity to Carbon Monoxide. The sensor can also be used to detect different gases containing CO, it is low cost and suitable for different application.

The NRF24L01 is a single chip radio transceiver for the worldwide 2.4-2.5 GHz ISM band. The transceiver frequency filter consists of a power amplifier, a crystal oscillator, a demodulator, modulator and protocol engine. Output power, frequency channels and protocol settings can be easily programmed through a SPI interface. The current consumption is very low, only 9 mA at -6dBm output power and 12.3mA in RX mode. It can easily save power with its built-in Power Off and Standby modes. When the NRF24L01 is powered off, it must always stand by 1.5 ms before entering either TX or RX mode. Supports up to 100 meters range in low band open area.

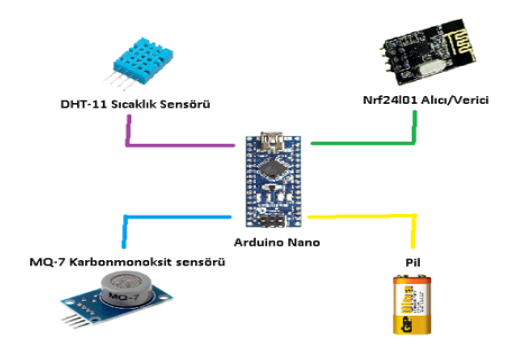


Figure 3. Components of a sensor node

4.2.2. The GSM/GPRS Module

SIM800L GSM / GPRS module is a miniature GSM modem that can be integrated into many IoT projects. This module can do almost anything a normal cell phone can do. It can be connected to the internet via GPRS or TCP/IP. Moreover, the module supports the quad-band GSM / GPRS network, which means it can work almost anywhere in the world. The Sim800L GSM/GPRS module plays the role of a gateway.

4.3. System software

3.3.1. The NRF24 library

In order to manage the NRF24 sensor network as required, nrf24 network open source library is used. When a transmission occurs from one radio module to another, the receiving radio communicates with an acknowledgment (ACK) packet with the sender to indicate success. If the transmitter does not receive an ACK, the radio automatically switches to a series of timed retries at regular intervals. Radios in this network are connected with the addresses assigned to the channels. Each radio can listen to 6 addresses on 6 lines, so each radio has a main line and 5 sublines used to create a tree structure. Nodes communicate directly with their parents and child nodes. All other traffic to or from the node must be routed across the network.

3.3.2. Phyton Based Interface

Python is an object oriented, interpretive, unitary and interactive high-level programming language. Today it has started to replace the C series programming languages, and it has a wide area of use especially related to IoT applications and interfaces. With Phyton one can easily access the open source codes of many libraries from graphics engines to artificial intelligence. It has been selected as the basis of the interface system designed in this application. The functional interface includes many systems from mapping system to drone command application.

3.3.3. Phyton Based TCP Server

The project uses TCP/IP based communication. In order for TCP messages to be transmitted, the recipient must be specified. However, if the recipient is a WiFi user, every time WiFi connection is turned on and off, the port addresses of the users on the WiFi change, even if the IP address remains the same. Therefore, in this system a server with fixed IP and port addresses is used to deliver data to the recipient. While the sender transfers data to the server, the receiver receives that data from the server. Thus, there is no need for a fixed port, the receiver and the transmitter can exchange messages over the desired IP address and port.

4.4. Forest Fire Detection Index Calculation

The novelty in this work, different from other similar system is in the use of FFDI and color-scale map. For defining the value of the FFDI the procedures determined by the HELIX project are used. The diagram for the calculation process is given in Figure 4. The number of sensors is independent of the map, so the number of nodes can be increased to obtain highly successful predictions in high risk areas. The FFDI index is calculated using the temperature and humidity values received from sensor readings while the wind speed is derived from a regional external source. The value obtained for the FFDI determines the degree of fire hazard. (Figure 5) Values from neighboring sensors are aggregated and averaged to provide easier color mapping. The color scale and an example map are provided in Figure 5.

40 Sokullu

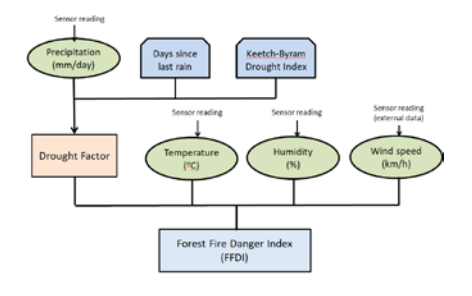




Figure 4. FFDI calculation

Figure 5. FFDI and color mapping

5. USER INTERFACE AND SYSTEM EVALUATION

The user interface is designed using Phyton and compatible libraries. Two types of user maps are provided: sensor map, which gives the positions, names and coordinates of the deployed sensors and a color-scale map,



Figure 6. The Sensor map and readings selection

which reflects the degree of fire danger. Figure 6 gives an example of a sensor map. The sensor map provides a selection of different readings, temperature, humidity, CO. The designed interface allows the user to add and delete sensors, to display sensor readings in a table format (Excel) or to edit descriptions of the sensors (Figure 7).



Figure 7. User interface editing and viewing options

Furthermore after the FFDI is calculated, the user is provided with a color-scale map depicting the degree of fire danger. (Figure 8).

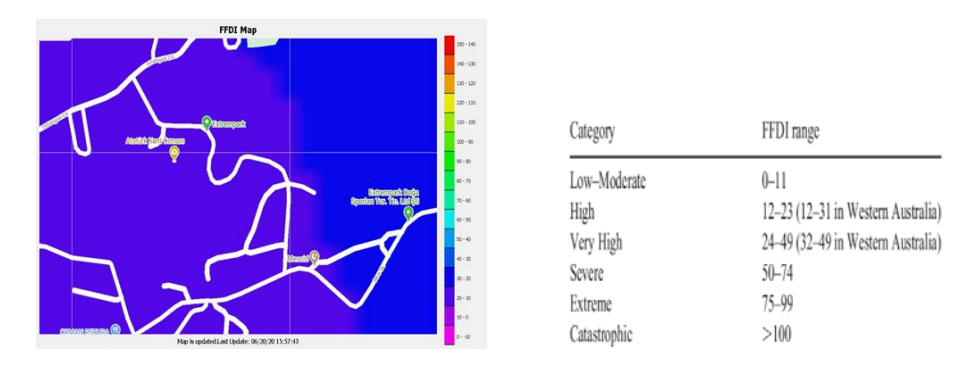


Figure 8. FFDI map with color scale; fire danger level-FFDI range table

Besides the visual features the software allows to calculate the absolute coordinates of the sensors using positioning information. The sensor positions can be mapped on Google maps. Also the coordinates can be calculated in latitude/longitude format to be fed to a drone. Drone can be sent to the coordinates determined to take visual aerial images of the area and/or provide help in extinguishing the fire. This part depends on the actual implementation.

The operation of the hardware and software was tested under various environmental conditions in the city of Bursa, Turkey. Sensor operation, control unit operation, FFDI calculations and TCP server connections all proved to be going smoothly without extensive connection delays. System was tested under varying weather conditions (high temperature, low humidity, high humidity etc.) but no real life fire situations were tested.

6. CONCLUSION

This paper discussed a system for an IoT based Fire Danger Detection. Several different approaches in monitoring and detecting fire danger conditions were incorporated in this work. First of all environmental data is collected using a WSN. A central unit, playing the role of a gateway as well is used for aggregating and evaluating the collected data. Using the FFDI calculation procedures suggested by the international HELIX project and using the McArthur and Noble Forest Fire danger Index a color map is provided depicting the degree of fire occurrence. An user interface, designed with Phyton provides options to add and delete sensors, to switch between different map options and to export the sensor data information into external (excel) file format. Furthermore, the software allows to calculate the absolute coordinates of the area involved and to direct an UAV if required for aerial imaging or to help extinguish the fire.

ACKNOWLEDGMENTS

The authors would like to thank Yusuf Tar and and Oguzhan Ozgur for their contributions.

REFERENCES

- [1]. D. Divya, A.; Kavithanjali, T.; Dharshini, "IoT Enabled Forest Fire Detection And Early Warning System", In Proc.: 2019 IEEE International Conference on System, Computation, Automation and Networking (ICSCAN), 1-5 Mar, 2019
- [2]. S.T.Saikumar, P. Sriramya, "IoT Enabled Forest Fire Detection and Altering The Authorities", International Journal of Recent Technology and Engineering, Volume 7, Issue 6, pp. 429-433, April 2019
- [3]. V. Dubey, P. Kumar, N. Chauhan, "Forest Fire Detection System Using IoT and Artificial Neural Network", in Lecture Notes in Networks and Systems, Volume 55, pp. 323-337, 2019
- [4]. G. Hristov, J. Raychev, D. Kinaneva, P. Zahariev, "Emerging Methods for Early Detection of Forest Fires Using Unmanned Aerial Vehicles and LoRaWAN Sensor Networks", In Proc. 28th EAEEIE Annual Conference (EAEEIE2018 28th.: 1-9 Sep, 2018
- [5]. D. Dzigal, A.Akagic, E.Buza, A. Brdjanin, N. Dardagan, "Forest Fire Detection based on Color Spaces Combination", In Proc.: 11th International Conference on Electrical and Electronics Engineering (ELECO), December, 2019
- [6] J.V.R. de Sousa, P.V. Gamboa, "Aerial Forest Fire Detection and Monitoring Using a Small UAV", ICEUBI2019 International Congress on Engineering — Engineering for Evolution, Volume 2020
- [7] A.G. McArthur, "Weather and grassland fire behavior", Department of National Development, Forestry and Timber Bureau leaflet no. 100. Canberra, Australia, 1966
- [8] A.G. McArthur "Fire behaviour in eucalypt forests", Department of National Development, Forestry and Timber Bureau leaflet no. 107. Canberra, Australia, 1967
- [9] I.R. Noble, G.A.V.Bary, A.M. Gill "McArthur's fire-danger meters expressed as equations", Aust J Ecol, 5:201–203 1980;
- [10] C. Van Wagner, "Development and structure of the Canadian forest fire weather index system", Canadian forest service technology report no. 35
- [11] L.S. Bradshaw, J.E. Deeming, R.E. Burgan, I.D. Cohen, "The 1978 national fire danger rating system: technical documentation", USDA forest service, intermountain forest and range experimental station technical report, INT-169, Ogden, Utah, USA
- [12] V. Nesterov, "Forest fires and methods of fire risk determination", Russian, Moscow, Goslesbumzdat
- [13] J. Skvarenina, J. Mindas, J. Holecy, J. Tucek, "Analysis of the natural and meteorological conditions during two large forest fire events in the Slovak Paradise National Park. In: International Bio-climatological Workshop, p 11, 2003

42 Sokullu

[14] J. J.Keetch; G.M. Byram, "A Drought Index for Forest Fire Control", Research Paper SE-38", Department of Agriculture, Forest Service, Southeastern Forest Experiment Station, Asheville, NC: U.S.35 p., 1968 https://www.srs.fs.usda.gov/pubs/rp/rp_se038.pdf
[15] https://helixclimate.eu/



Investigation of the Microstructure and Mechanical Properties of Gas Metal Arc Welded AISI 304 Austenitic Stainless Steel Butt Joints

Mehmet Ali EZER¹, Gürel ÇAM²*

¹ Iskenderun Technical University, Institute of Graduate Studies, Department of Mechanical Engineering, 31200 iskenderun-Hatay, Turkey.

²Iskenderun Technical University, Faculty of Engineering and Natural Sciences, Department of Mechanical Engineering, 31200 İskenderun-Hatay, Turkey.

*Corresponding Author email: gurel.cam@iste.edu.tr

Abstract

Austenitic stainless steels exhibit very good properties such as very good formability even at low temperatures, good mechanical properties and high corrosion resistance. Austenitic steels are the grades which are produced most in quantity among all stainless steels and AISI 304 is the most widely used grade among the austenitic steels. They are used widely in several industries such as chemistry and petro-chemistry industries, food processing industry, medical and dental equipments and kitchenware. However, several difficulties such as carbide precipitation in heat affected zone, and hot cracking and formation of brittle sigma phase in the fusion zone may be encountered in fusion joining of these steels. High heat inputs involved in arc welding may even increase the occurrence of these problems. Thus, successful joining of these alloys using conventional fusion welding methods is rather important. This study aims at investigating the influence of heat input on microstructural evolution in the weld region and the mechanical properties of the welded joints in gas metal arc welding of AISI 304 austenitic steel plates. For this purpose, 5 mm thick AISI 304 plates were joined using different heat input values. Detailed optical microscopy and micro-hardness measurements in addition to tensile and bending tests were carried out to study the microstructural and mechanical properties of the welded plates produced. Furthermore, it was also attempted to determine the effect of heat input on the performance of gas metal arc welded AISI304 joints.

Key words

Austenitic stainless steel, AISI 304, heat input, carbide precipitation, weld performance

1. INTRODUCTION

Austenitic stainless steels (ASS) exhibit good corrosion resistance and superior mechanical properties such as high good formability. Thus, they are widely used in a wide spectrum of applications ranging from kitchen utilities and implants to power plants and from steel bridges to petroleum, oil and gas, nuclear and marine industries [1-5].

The major problem encountered in fusion joining of stainless steels (SS) is the formation of chromium-depleted zones (i.e., carbide precipitation along the grain boundaries in heat affected zone - HAZ). Hot cracking and

44 Ezer and Çam

formation of brittle sigma phase may also be encountered in the fusion zone (FZ) of these steels. Somervuori et al. [6] clearly demonstrated that the Cr-depleted regions in the FZ deteriorated the corrosion behaviour. Kim et al. [7] investigated the influence of Creq/Nieq ratio on the microstructural changes and mechanical behaviour of 316L SS joints. They observed that higher Creq/Nieq ratios significantly affected the microstructure of AISI 316L joints. Shojaati and Beidokhti [8] also studied how different filler metals (ER 310, ER 316L, duplex ER 2209 and Ni-based Nichrome 80/20 filler metals) influenced the microstructural and mechanical characteristics of dissimilar AISI 304/AISI 409 SS joints. They reported that austenite with different morphologies of ferrite such as lathy, acicular and vermicular were observed in the case of 310 and 316L austenitic filler metals. A mixture of austenite and ferrite phases was seen in the microstructure obtained with the duplex filler metal. Ferrite and Widmanstätten austenite were higher in the regions next to the weld interface owing to the faster cooling here and, thus, the incomplete transformation. The joint obtained using the Ni-based weld metal displayed a microstructure consisting of a Ni-Cr-Fe matrix and Fe-based precipitates in the FZ. Furthermore, the formation of a thin layer of martensite in this joint resulted in the fusion line cracking. It was also reported that the high content of δ -ferrite in the microstructure of FZ increased the hardness and tensile strength values.

As already mentioned fully ASSs are prone to hot cracking in fusion welding. In general, it is recommended that the delta-ferrite (δ -ferrite) content in the FZ should be kept in the range of 3-10% to prevent hot cracking problem [5]. Higher amounts of delta ferrite make the FZ more sensitive to high temperatures because of the phase transformation [5,9]. Dadfar et al. [10] studied the corrosion behavior of autogenous Gas Tungsten Arc (GTA) welded AISI 316L joints and observed that the solution heat treatment enhances the corrosion resistance of the as-welded AISI 316L joint. Muthupandi et al. [11] studied the welding of super duplex stainless steels. They concluded that the heat input used should be kept as low as possible. Moreover, they claimed that higher heat inputs might also lead to the precipitation of undesirable brittle phases such as σ (sigma) or X (chi).

Heat input is of great importance in joining of austenitic stainless steels as already pointed out in the preceding paragraph. The solid state friction stir welding technique, which is originally developed for difficult-to-fusion join low melting temperature Al-alloys [12-20] as well as Cu-alloys [21-23] and Pb [24], offers a potential to join steels including stainless steels [25,26]. Additionally, low heat input CMT arc welding method [13,27] or power beam welding techniques such as laser or electron beam welding [28-33] may also be used in joining of these steels. Due to this fact, numerous studies have been conducted on FSW of steels including stainless steels in last 30 years [26,27,34-41]. However, wear of the stirring tool is still a problem to overcome in FSW of steels since the peak temperature involved may reach over 1000 °C, and even the tools made of high temperature resistant materials may wear slowly over the time.

In this study, the influence of heat input applied to the AISI 304 plates on the microstructural evolution in the joint area and on joint properties was investigated. For this purpose, AISI 304 plates with a thickness of 5 mm were joined by gas metal arc welding (GMAW) using a filler wire of 308 with a diameter of 1.2 mm. Detailed microstructural investigations were conducted for microstructural characterization of the joints. Extensive microhardness measurements in addition to the mechanical testing were conducted to determine the joint properties. Moreover, the effect of heat input on the microstructural changes taking place in the weld region and thus on the joint performance was evaluated.

2. MATERIALS AND METHOD

The material used in this study is AISI 304 grade austenitic stainless steel plates of 5 mm thick. It was supplied in the form of large plate with the sizes of 1500x1000x5 mm3. Its chemical composition is given in Table 1.

Chemical Composition (wt. %)										
Material	C	Si	Mn	P	S	Cr	Ni	N	Mo	Cu
Base Material (AISI 304)	0,019	0,42	1,56	0,035	0,002	18,2	8,1	0,053		
Filler Material (ER308LSi)	0,025	0,804	1,95	0,010	0,023	20,016	9,966	0,035	0,181	0,287

Table 1. Chemical composition of AISI 304 grade austenitic steel plates used in this study.

The as-received 304 large plate was cut into the rectangular pieces of 250x190 mm and welding grooves were machined as shown schematically in Fig. 1, for welding trials. The surfaces to be welded were cleaned mechanically using a stainless steel metal brush prior to joining. The plates were welded by GMAW process with the use of an ER308LSi filler wire of 1,2 mm in diameter (the chemical composition of which is given in Table 1), the feeding rate was 17,5 mm/s, in two passes. The weld parameters employed in welding trials were given in Table 2. Two different heat inputs were employed in order to determine the effect of heat input on joint quality.

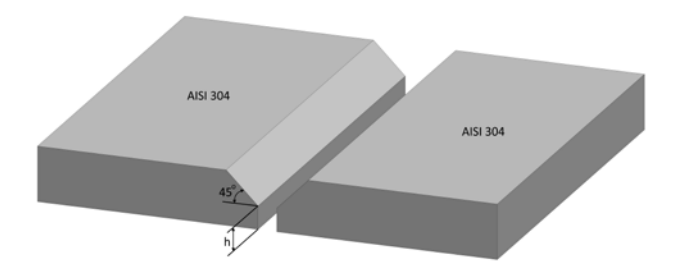


Figure 1. Preparation of the plates for welding trials.

Table 2. The weld parameters employed in welding trials (the same weld parameters were used in each pass in both welding trials).

Weld Trial	Current	Voltage	Weld speed	Wire feed rate	CL:-14:	
weid Triai	(A)	(V)	(mm/s)	(mm/s)	Shielding gas	
Low Heat Input	ave. 385	28	4,5	17,5	Argon (99,95%)	
High Heat Input	ave. 465	27	4,0	17,5	Argon (99,95%)	

Following the welding trials, a metallography specimen, two bend specimens and four tensile specimens were prepared for each joint to investigate the microstructural evolutions in the weld regions of the joints and their mechanical properties. Four tensile specimens were also extracted from the base plate for comparison purpose. The metallography specimens were first ground and then polished prior to etching procedure in which the specimens were immersed in an etchant comprising of 50 ml HCl and 150 ml HNO3 for about 15 seconds. A detailed microstructural investigation was conducted on these metallography specimens as well as microhardness measurements. Microhardness measurements were conducted on each joint along three lines across the weld region, one being almost in the center, the other two lines lying 1 mm from the surface and root of the joints, using a load of 500 g, as schematically illustrated in Fig. 2.

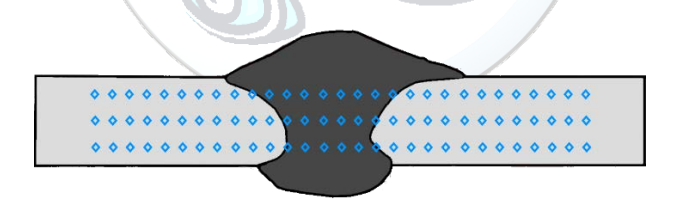


Figure 2. Schematic illustration of the conduction of microhardness measurements on each joint along three lines across the weld region, one being almost in the center, the other two lines lying 1 mm from the surface and root of the joints.

Transverse tensile specimens of the BM and the joints were also tested with a loading rate of 15 mm.min-1 in order to evaluate the joint performance values and the weld qualities. In addition, the two bend specimens extracted from each joint for bend testing (180 degrees). One of them was bent in the condition of surface bend and the other in the root bend configuration and the weld center in the middle position in order to determine whether cracking occurs in the weld region or not. Furthermore, an attempt was made to determine the effect of heat input on the microstructural evolution in the HAZ and thus on weld quality and performance.

3. RESULTS AND DISCUSSION

The results obtained from this study will be discussed in two subsections, namely microstructural aspects and mechanical properties, below.

46 Ezer and Çam

3.1. Microstructural Aspects

The macrographs illustrating the weld cross-sections of the joints produced using low and high heat inputs, respectively, are given in Figure 3. Figure 4 shows micrographs illustrating the base plate microstructure and the microstructures evolved in the FZs and HAZs of the joints produced. As seen from the micrographs, the AISI 304 grade austenitic base plate has a single phase microstructure consisting of austenite grains. Both joints showed a similar microstructural evolution within the weld region. A fine dendritic structure is observed in the FZ of both joints (Fig. 4b and c), which is very usual for this steel. No visible difference was observed between the FZ structures of both joints. Thus, there is no clear effect of heat input difference used.

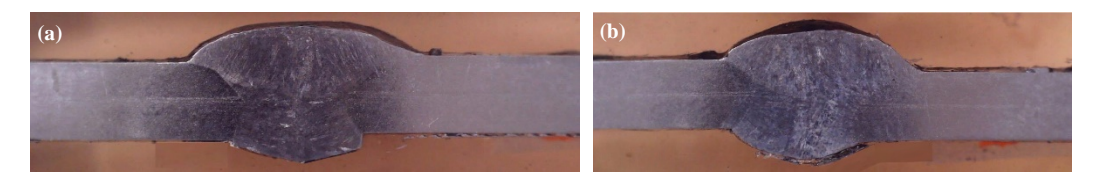


Figure 3. The macrographs illustrating the weld cross-sections of the joints produced: (a) the lower heat input joint and (b) the higher heat input joint.

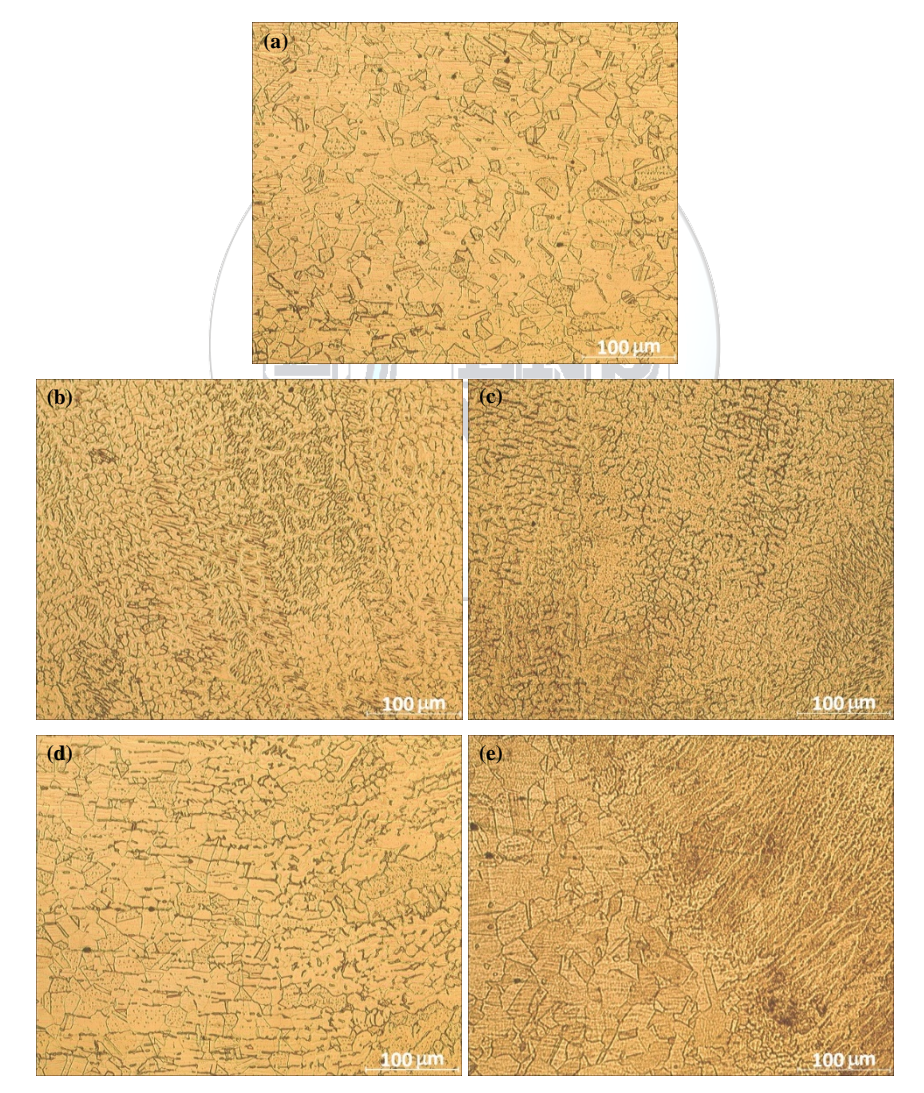


Figure 4. The micrographs illustrating the microstructures of: (a) base plate, (b) FZ of the lower heat input joint, (c) FZ of the higher heat input joint, (d) HAZ of the lower heat input joint and (e) HAZ of the higher heat input joint.

However, there is a clear difference between the microstructures evolving in the HAZs of two joints produced using different heat inputs. As seen from Figure 4(e), larger recrystallized grains of austenite phase were formed in the HAZ of the higher heat input joint. On the other hand, austenite grain size in the HAZ of the lower heat input joint is similar to that of the BM and finer compared to that of HAZ of the higher heat input joint. There are also some precipitates within the HAZ of the low heat input joint elongated in the cold rolling direction (Fig. 4d), indicating that a complete recrystallization did not occur due to lower input involved. Moreover, the fusion interface is more visible in the high heat input joint as a result of grain growth to a larger extent taking place in this joint due to the recrystallization occurring at higher temperatures compared to the lower heat input joint. In addition, there is no indication of chromium carbide precipitation within the HAZ of the higher heat input joint in contrast to the lower heat input joint as seen from Fig. 4(e).

3.2. Mechanical Properties

Figure 5 gives the hardness profiles obtained from the microhardness measurements conducted along three lines across the joints produced using low and high heat inputs. These hardness profiles show the hardness variations across the joints. As clearly seen from these profiles both joints exhibited similar hardness values across the weld region. The hardness profiles clearly show that there is neither a hardness increase (strength overmatching) nor hardness decrease (strength undermatching) in the weld region for both joints. Thus, both joints display a typical hardness profile of strength evenmatching joints. Furthermore, no significant hardness variation was observed across the weld area for both joints, indicating that the heat input variation used has no significant effect on hardness although a grain growth was detected in the high heat input joint. This implies that the slight grain growth in the HAZ of the high heat input joint does not significantly vary the hardness of this region.

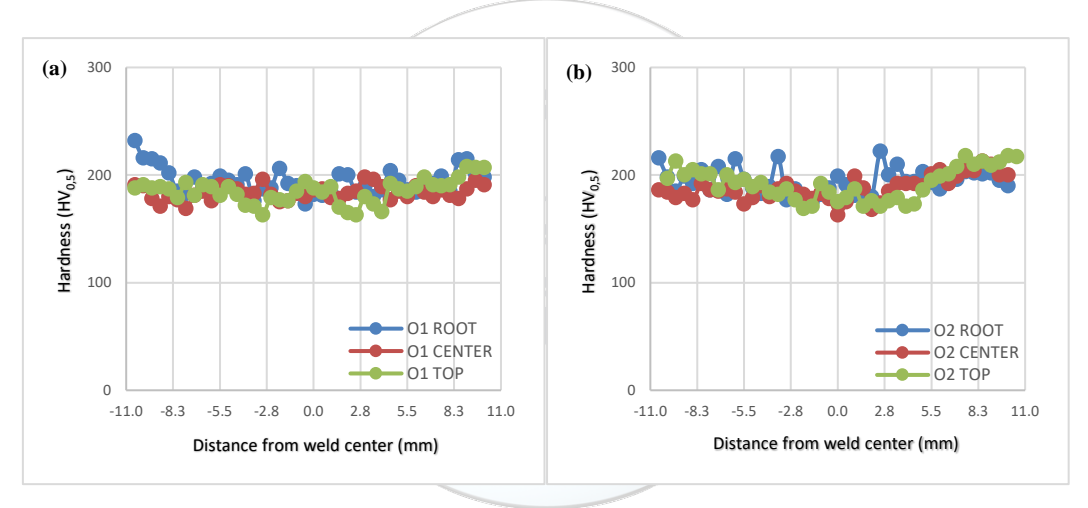


Figure 5. Hardness profiles showing the hardness variation across the joints: (a) lower and (b) the higher heat input joints.

Tensile test results obtained from the specimens prepared from the BM and the joints produced using low and high heat inputs are summarized in Table 3 and Figures 6 and 7. The AISI 304 base plate used in this study displayed a yield stress, tensile strength and elongation of 361 MPa, 636 MPa and about 48%, respectively. As clearly seen from the Table and Figures, both joints exhibited similar tensile properties to those of the BM, indicating that the performance of both joints are reasonably good. Indeed, the both joints exhibited similar tensile strength performance and ductility performance values of about 102% and 80%, respectively, indicating that the heat input variation employed in the current study does not have a significant influence on the joint performance. This results are quite reasonable since the joints did not display any weld defect and the hardness is more or less homogeneous across the joints. Figure 8 shows the fracture locations in all the tensile test specimens extracted from both lower and higher heat inputs joints after testing. As seen from this figure, all the specimens fractured in the base plate far away from the FZ. This clearly demonstrates that the weld quality, thus the joint performance, of both joints is quite good in tensile test condition.

Similar to the case in tensile testing, the heat input variation employed in this study did not have a significant effect on the joint behavior in bend testing. No cracking occurred in both surface and root bend specimens extracted from both joints (namely the lower and heat input joints) as shown in Figure 9. These results indicate that the heat input difference used in this study apparently did not have any diminishing effect on the weld

48 Ezer and Çam

performance in bending condition despite the presence of some carbide precipitates in the HAZ region next to the fusion line of the joint obtained using lower heat input (Fig. 4d).

Specimen	R _{P0.2} (MPa)	R _m (MPa)	Elongation (%)	Strength Performance (%)	Ductility Performance (%)	Failure Location
Base Plate	366, 358, 359 (361)	643,631,633 (636)	48, 48, 49 (48)			
Low Heat Input Joint	357, 374, 376, 362 (367)	650, 653, 649, 652 (651)	39, 38, 40, 40 (39)	102	81	Base plate
High Heat	349, 366, 353 (356)	631,648, 641 (640)	38, 38, 40 (38)	101	79	Base plate

Table 3. Tensile test results.

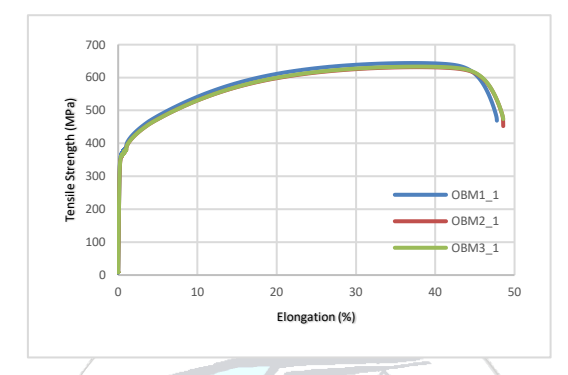


Figure 6. Stress-elongation (%) curve of the base plate AISI 304 steel used.

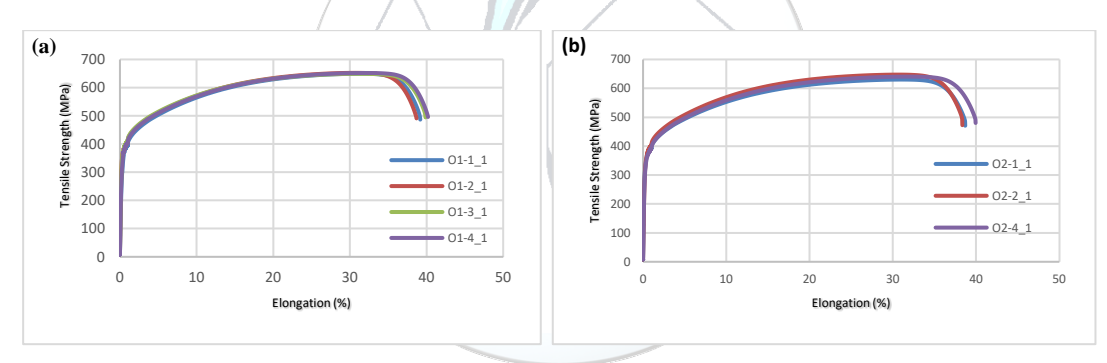


Figure 7. Stress-elongation (%) curves of the joints: (a) lower and (b) higher heat input joints.



Figure 8. Macrographs showing the fracture locations in the tensile test specimens extracted from: (a) lower and (b) higher heat input joints.

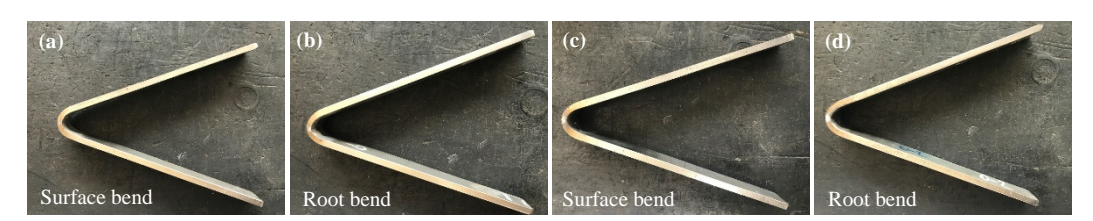


Figure 9. Macrographs showing the surface and root bend specimens, respectively, extracted from: (a) and (b) lower; and (c) and (d) higher heat input joints. Note that no cracking occurred in any of the specimens.

4. CONCLUSIONS

The influence of heat input experienced by the plates during welding on the microstructural evolution in the joint area and on joint properties was investigated for GMAW welded 5 mm thick AISI 304 plates using a filler wire of ER308 with a diameter of 1.2 mm. The following conclusions were withdrawn from this study:

- AISI 304 plates were defect-free welded in two passes by the GMAW process.
- A fine dendritic microstructure was obtained in the FZs of both joints.
- Some precipitates within the HAZ of the low heat input joint elongated in the cold rolling direction were observed while in the HAZ of the higher heat input joint larger recrystallized grains of austenite phase were formed but no carbide precipitates were observed.
- All the tensile test specimens prepared from both joints fractured in the BM far away from the FZ.
- Both joints exhibited similar mechanical properties (strength and ductility) to those of the base plate.
 Indeed, both joints displayed high tensile strength performance and ductility performance values of over 100% and about 80%, respectively.
- Both surface and root bend specimens extracted from both joints did not crack in bending test, indicating that the heat input variation employed in the current study does not have a significant influence on the joint performance.

ACKNOWLEDGMENT

We would like to thank Mr. Sedat UYSAL and Tuğrul YAZGAN from NOKSEL Çelik Boru Sanayi A.Ş. (Noksel Steel Pipe Inc.), İskenderun-Hatay, Turkey, for their support in conduction of the metallography and mechanical tests. The authors also thank Hikmet Gizem SARSILMAZ from Kahraman-Sarsılmaz Machinery, İskenderun, for conducting welds.

CONFLICT OF INTEREST STATEMENT

The authors declare that there is no conflict of interest.



REFERENCES

- [1]. B. Weiss and R. Stickler, "Phase instabilities during high temperature exposure of 316 austenitic stainless steel", *Metall. Trans.*, vol. 3, pp. 851-866, 1972.
- [2]. C. Balaji, S.V.A. Kumar, S.A. Kumar, and R. Satish, "Evaluation of mechanical properties of SS 316 L weldments using tungsten inert gas welding", *Int. J. Eng. Sci. Technol.*, vol. 4, pp. 2053-2057, 2012.
- [3]. L.P. Karjalainen, T. Taulavuori, M. Sellman, and A. Kyröläinen, "Some strengthening methods for austenitic stainless steels", *Steel Research International*, vol. 79, pp. 404-412, 2008.
- [4]. K. Devendranath Ramkumar, A.Singh, S. Raghuvanshi, A. Bajpai, T. Solanki, M. Arivarasu, N. Arivazhagan, and S. Narayanan, "Metallurgical and mechanical characterization of dissimilar welds of austenitic stainless steel and super-duplex stainless steel A comparative study", *Journal of Manufacturing Processes*, vol. 19, pp. 212-232, 2015.
- [5]. J.C. Lippold and D.J. Kotecki, Welding Metallurgy and Weldability of Stainless Steels. 1st ed., Hoboken: John Wiley & Sons Inc.; 2005.
- [6]. M.E. Somervuori, L.S. Johansson, M.H. Heinonen, D.H.D. van Hoecke, N. Akdut, and H.E. Hänninen, "Characterisation and corrosion of spot welds of austenitic stainless steels", *Mater. Corros.*, vol. 55, pp. 421-436, 2004.
- [7]. Y.H. Kim, D.J. Lee, J.C. Byun, K.H. Jung, J.I. Kim, H.J. Lee, Y.T. Shin, S.H. Kim, and H.W. Lee, "The effect of sigma phases formation depending on Cr/Ni equivalent ratio in AISI 316L weldments", *Mater. Des.*, vol. 32, pp. 330-336, 2011.
- [8]. M. Shojaati and B. Beidokhti, "Characterization of AISI 304/AISI 409 stainless steel joints using different filler materials", *Construction and Building Materials*, vol. 147, pp. 608-615, 2017.
- [9]. J. Barcik, "Mechanism of σ -phase precipitation in Cr-Ni austenitic steels". *Mater Sci Technol.*, vol. 4, pp. 5-15, 1988.
- [10]. M. Dadfar, M.H. Fathi, F. Karimzadeh, M. R. Dadfar, and A. Saatchi, "Effect of TIG welding on corrosion behavior of 316L stainless steel". *Mater Lett.*, vol. 61, pp. 2343-2346, 2007.

50 Ezer and Çam

[11]. V. Muthupandi, P. Bala Srinivasan, S. K. Seshadri, and S. Sundaresan, "Effect of weld metal chemistry and heat input on the structure and properties of duplex stainless steel welds", *Mater. Sci. Eng. A*, vol. 358, pp. 9-16, 2003.

- [12]. N. Kashaev, V. Ventzke, and G. Çam, "Prospects of laser beam welding and friction stir welding processes for aluminum airframe structural applications", *Journal of Manufacturing Processes*, vol. 36, pp. 571-600, 2018.
- [13]. G. Çam and G. İpekoğlu, "Recent developments in joining of aluminium alloys", *Int. J. Adv. Manuf. Technol.*, vol. 91(5-8), pp. 1851-1866, 2017.
- [14]. G. Çam, "Friction stir welding (FSW) A novel welding technology developed for Al-Alloys", *Engineer and Machinery*, vol. 46 (541), pp. 30-39, Feb. 2005. (in Turkish)
- [15]. A. Von Strombeck, G. Çam, J.F. Dos Santos, V. Ventzke, and M. Koçak, "A comparison between microstructure, properties, and toughness behavior of power beam and friction stir welds in Al-alloys", in Proc. of the TMS 2001 Annual Meeting Aluminum, Automotive and Joining (New Orleans, Louisiana, USA, February 12-14, 2001), eds: S.K. Das, J.G. Kaufman, and T.J. Lienert, pub.: TMS, Warrendale, PA, USA, pp. 249-264, 2001.
- [16]. G. Çam, V. Javaheri, and A. Heidarzadeh, "Advances in FSW and FSSW of Dissimilar Al-Alloy Plates", *Journal of Adhesion Science and Technology*, 2022 (DOI: https://doi.org/10.1080/01694243.2022.2028073).
- [17]. G. İpekoğlu, B. Gören Kıral, S. Erim, and G. Çam, "Investigation of the effect of temper condition friction stir weldability of AA7075 Al-alloy plates", *Mater. Tehnol.*, vol. 46 (6), pp. 627-632, 2012.
- [18]. G. İpekoğlu, S. Erim, B. Gören Kıral, and G. Çam, "Investigation into the effect of temper condition on friction stir weldability of AA6061 Al-alloy plates", *Kovove Mater.*, vol. 51 (3), pp. 155-163, 2013.
- [19]. G. Çam, G. İpekoğlu, and H. Tarık Serindağ, "Effects of use of higher strength interlayer and external cooling on properties of friction stir welded AA6061-T6 joints", *Sci. Technol. Weld. Join.*, vol. 19 (8), pp. 715-720, 2014.
- [20]. G. Çam, S. Güçlüer, A. Çakan, and H.T. Serindağ, "Mechanical properties of friction stir butt-welded Al-5086 H32 plate", *Mat.-wiss. u. Werkstofftech.*, vol. 40 (8), pp. 638-642, 2009.
- [21]. T. Küçükömeroğlu, E. Şentürk, L. Kara, G. İpekoğlu, and G. Çam, "Microstructural and mechanical properties of friction stir welded nickel-aluminum bronze (NAB) alloy", *Journal of Materials Engineering and Performance (JMEPEG)*, vol. 25 (1), pp. 320-326, 2016.
- [22]. G. Çam, S. Mistikoglu, and M. Pakdil, 'Microstructural and mechanical characterization of friction stir butt joint welded 63%Cu-37%Zn brass plate', *Weld. J.*, vol. 88 (11), pp. 225s-232s, 2009.
- [23]. G. Çam, H.T. Serindağ, A. Çakan, S. Mıstıkoğlu, and H. Yavuz, 'The effect of weld parameters on friction stir welding of brass plates', *Mat.-wiss. u. Werkstofftech.*, vol. 39 (6), pp. 394-399, 2008.1997.
- [24]. A. Günen, E. Kanca, M. Demir, F. Çavdar, S. Mistikoğlu, and G. Çam, "Microstructural and mechanical properties of friction stir welded pure lead", *Indian Journal of Engineering & Materials Sciences (IJEMS)*, vol. 25 (1), pp. 26-32, 2018.
- [25]. G. Çam, "Friction stir welded structural materials: Beyond Al-alloys", *Int. Mater. Rev.*, vol. 56 (1), pp. 1-48, 2011.
- [26]. G. Çam, G. İpekoğlu, T. Küçükömeroğlu, and S.M. Aktarer, "Applicability of friction stir welding to steels", *Journal of Achievements in Materials and Manufacturing Engineering (JAMME)*, vol. 80(2), pp. 65-85, 2017.
- [27]. S. Selvi, A. Vishvaksenan, and E. Rajasekar, "Cold metal transfer (CMT) technology An overview", Cold metal transfer (CMT) technology An overview, *Defence Technology*, vol. 14, pp. 28-44, 2018.
- [28]. G. Çam, Ç. Yeni, S. Erim, V. Ventzke, and M. Koçak, "Investigation into properties of laser welded similar and dissimilar steel joints", *Sci. Technol. Weld. Join.*, vol. 3 (4), pp. 177-189, 1998.
- [29]. J. dos Santos, G. Çam, F. Torster, A. Insfran, S. Riekehr, V. Ventzke, and M. Koçak, "Properties of power beam welded steels, Al- and Ti-alloys: Significance of strength mismatch", *Welding in the World*, vol. 44 (6), pp. 42-64, 2000.
- [30]. G. Çam, M. Koçak, and J.F. dos Santos, "Developments in laser welding of metallic materials and characterization of the joints", *Welding in the World*, vol. 43 (2), pp. 13-26, 1999.
- [31]. G. Çam, V. Ventzke, J.F. dos Santos, M. Koçak, G. Jennequin, P. Gonthier-Maurin, M. Penasa, and C. Rivezla: "Characterization of laser and electron beam welded Al-alloys", *Prakt. Metallogr.*, vol. 36 (2), pp. 59-89, 1999.
- [32]. G. Çam and M. Koçak, "Microstructural and mechanical characterization of electron beam welded Al-alloy 7020", *J. Mater. Sci.*, vol. 42 (17), pp. 7154-7161, 2007.
- [33]. G. Çam, V. Ventzke, J.F. dos Santos, M. Koçak, G. Jennequin, and P. Gonthier-Maurin, "Characterisation of electron beam welded aluminium alloys", *Sci. Technol. Weld. Join.*, vol. 4 (5), pp. 317-323, 1999.
- [34]. T. Küçükömeroğlu, S.M. Aktarer, G. İpekoğlu, and G. Çam, "Investigation of mechanical and microstructural properties of friction stir welded dual phase (DP) steel", *IOP Conf. Series: Materials Science and Engineering*, vol. 629, Paper No: 012010, 2019.

- [35]. G. İpekoğlu, T. Küçükömeroğlu, S.M. Aktarer, D.M. Sekban, and G. Çam, "Investigation of microstructure and mechanical properties of friction stir welded dissimilar St37/St52 joints", *Materials Research Express*, vol. 6 (4), Article Number: 046537, 2019.
- [36]. T. Küçükömeroğlu, S.M. Aktarer, G. İpekoğlu, and G. Çam, "Mechanical properties of friction stir welded St 37 and St 44 steel joints", *Materials Testing*, vol. 60 (12), pp. 1163-1170, 2018.
- [37]. T. Küçükömeroğlu, S.M. Aktarer, G. İpekoğlu, and G. Çam, "Microstructure and mechanical properties of friction stir welded St52 steel joints", *International Journal of Minerals, Metallurgy and Materials*, vol. 25 (12), pp. 1457-1464, 2018.
- [38]. L. Cui, H. Fujii, N. Tsuji, and K. Nogi, "Friction stir welding of a high carbon steel", *Scripta Mater.*, vol. 56, pp. 637-40, 2007.
- [39]. P. Chansoria, P. Solanki, and M.S. Dasgupta, "Parametric study of transient temperature distribution in FSW of 304L stainless steel", *Int. J. Adv. Manuf. Technol.*, vol. 80, pp. 1223-1239, 2015.
- [40]. H. Kokawa, S.H.C. Park, Y.S. Sato, K. Okamoto, S. Hirano, and M. Inagaka, "Microstructures in friction stir welded 304 austenitic stainless steel", *Welding in The World*, vol. 49, pp. 34-40, 2005.
- [41]. A.P. Reynolds, W. Tang, T. Gnaupel-Herold, and H. Prask, "Structure, properties, and residual stress of 304L stainless steel friction stir welds", *Scripta Mater.*, vol. 48 (9), pp. 1289-1294, 2003.



Microstructural and Mechanical Characterization of Gas Metal Arc Welded AISI 430 Ferritic Stainless Steel Joints

Mustafa ŞENOL¹, Gürel ÇAM^{2*}

¹ Iskenderun Technical University, Institute of Graduate Studies, Department of Mechanical Engineering, 31200 iskenderun-Hatay, Turkey.

²Iskenderun Technical University, Faculty of Engineering and Natural Sciences, Department of Mechanical Engineering, 31200 İskenderun-Hatay, Turkey.

*Corresponding Author email: gurel.cam@iste.edu.tr

Abstract

Ferritic stainless steels contain Cr as the main alloying element and display very good corrosion resistance even at high temperatures. These steels are widely used in manufacturing of products such as hot water storage units, car chassis components, exhaust systems and kitchenware. The most characteristic difficulty in fusion joining of this type of stainless steels is the grain growth in the HAZ. Furthermore, martensite formation or carbide precipitation along the grain boundaries in the HAZ may also be observed if the heat input used is extremely high or C content of the steel and/or filler wire high. Thus, it is required that the heat input should be kept low or filler wires with low C should be used to successfully join these steels by conventional fusion welding methods. The determination of the effect of heat input on microstructural evolution in the weld region and the mechanical properties of the joints in gas metal arc welding of AISI 430 ferritic steel plates is aimed in this study. To that end, AISI 430 ferritic steel plates with a thickness of 5 mm were joined using different heat input values. The microstructures in the weld region and mechanical properties of the welded joints were determined by extensive optical microscopy investigations, microhardness measurements, tensile and bending tests. Moreover, the heat input effect on the joint performance was also studied.

Key words

Ferritic stainless steel, AISI 430, heat input, martensite formation, weld performance

1. INTRODUCTION

AISI 430 grade ferritic stainless steel (FSS) possesses high strength and corrosion resistance coupled with relatively low cost. In addition, ferritic stainless steels have more resistance to chloride stress corrosion cracking than austenitic stainless steels (ASS). Thus, it is widely used in a wide range of applications ranging from household utensils, vehicle exhausts, road and rail vehicles to other applications in several industries such as oil, gas, petrochemical, nuclear and power industries [1-10]. They are the second largest selling type of stainless steels behind austenitic grades.

The major problem encountered in welding of FSSs is the reduced ductility (toughness) in the heat affected zone (HAZ) which limits their application [2]. This problem is caused by the evolution of large grains in the HAZ of

fusion welds. The temperature in this region reaches a critical temperature (955 °C) and causes rapid growth of the ferrite grains [3]. Moreover, although the carbon content of FSSs is very small, on rapid cooling the formation of intergranular martensite and/or chromium-depleted zones may take place along the grain boundaries in HAZ. Formation of martensite in the HAZ even in small amounts results in a loss of ductility in addition to grain coarsening. Carbide precipitation can make the steel sensitive to inter-crystalline corrosion.

For instance, Aguilar et al. [6] investigated the metallurgical transformations occurring during the submerged arc welding (SMAW) of AISI 430 FSS with AISI 316L ASS using two different filler wires, namely E309L and E2209. They clearly demonstrated that both grain growth and martensite formation at the ferrite grain boundaries took place in the HAZ of 430 steel next to the fusion line in both joints. They also reported that a refined grain zone was present following the coarse grain zone in the BM side of the HAZ of 430 steel. Similarly, Antunes et al [8] investigated the effect of the weld metal on the microstructure and mechanical behaviour of FSS AISI 444 welded joints employing two types of filler metal of ASS, namely E309L and E316L. The microstructural examinations conducted showed that a grain coarsening occurred in the HAZ of both welded joints. A recent study indicated that duplex SS consumables such as E2204 can be used to obtain defect-free welds of FSS. Duplex SS consumables can also yield higher strength than ASS consumables [9]. Moreover, Zhou et al [7] studied the influence of heat input on microstructural and mechanical characteristics of AISI 430 FSS joints produced by cold metal transfer GMA welding using E308L filler wire. They observed that the carbide precipitation and the formation of intergranular martensites as well as the coarsening of ferrite grains occurred in the coarse-grained zone of HAZ. They also reported that increasing heat input also caused an increase in the amount of intergranular martensite and carbide precipitation.

Heat input is a very important weld parameter in joining of FSSs. Thus, a low heat input solid state welding technique, namely friction stir welding, which was originally developed for low melting temperature Al-alloys [11-20] as well as Cu-alloys [21-23] and Pb [24], has a potential to join steels including stainless steels [25,26]. Similarly, low heat input CMT arc welding method [12,27] or power beam welding techniques [28-33] also offers a potential to join these steels. As a result, several studies have been conducted on FSW of steels including SSs in last 30 years [26,27,34-41]. However, it was observed that wear of the stirring tool takes place in FSW of steels since a peak temperature may reach over 1000 oC. Thus, even the tools made of high temperature resistant materials may wear slowly over the time.

Furthermore, extra low C, Ti or Nb containing FSS grades have been developed in recent years to overcome carbide precipitation and martensite formation along the ferrite grain boundaries within the HAZ. However, it is usually required to keep the heat input as low as possible to avoid grain growth within the HAZ next to the fusion line. Thus, the use of a low heat input (1kj/mm) and an interpass temperature of maximum 100-120°C is recommended in welding of these steels. Moreover, preheat is not advisable although it may be helpful when welding sections over 10mm thick, where excessive grain growth and welding restraint may result in cracking of the joint. Although preheating will lead to grain growth, it will reduce the cooling rate experienced in the HAZ. Thus, this will keep the FZ temperature above the ductile-brittle transition point and may reduce residual stresses. Preheat temperatures should be, however, kept between 50-250 °C depending on the composition of the steel.

In this study, the weldability of FSS, namely AISI 430, and the influence of heat input applied to the plates on the microstructural evolution in the joint area and thus on joint properties were investigated. Thus, 5 mm thick AISI 430 plates were welded by gas metal arc welding (GMAW) using a filler wire of ER307 with a diameter of 1.2 mm. Detailed microstructural investigations were conducted for microstructural characterization of the joints and detailed microhardness measurements were carried out in addition to the mechanical tests to determine the joint properties. Moreover, the influence of heat input on the microstructure in the joint area and thus on the joint performance was evaluated.

2. MATERIALS AND METHOD

In this study, AISI 430 grade FSS plates with a thickness of 5 mm were used. It was received in the form of large plate with the sizes of 1500x1000x5 mm3. Its composition is illustrated in Table 1.

Chemical Composition (wt. %)										
Material	C	Si	Mn	P	S	Cr	Ni	N	Mo	Cu
Base Material (AISI 430)	0,037	0,38	0,50	0,031	0,002	16,16	0,27	0,033	0,01	0,20
Filler Material (ER307)	0,075	0,790	7,10	0,009	0,020	19,075	9,010		0,005	0,070

Table 1. Composition of AISI 430 grade austenitic steel plates used in this study.

Rectangular pieces with the sizes of 250x190 mm were extracted from the as-received large plate and welding grooves were machined as illustrated in Fig. 1, prior to welding. The surfaces to be joined were cleaned mechanically using a stainless steel metal brush prior to the joining process. GMAW welding was carried out in two passes using an ER307 filler wire of 1.2 mm in diameter, the feeding rate was 17,5 mm/s. The weld parameters employed in welding trials were given in Table 2. As seen from this table, the welding trials were conducted using two different heat inputs in order to determine how the joint performance is influenced by heat input.

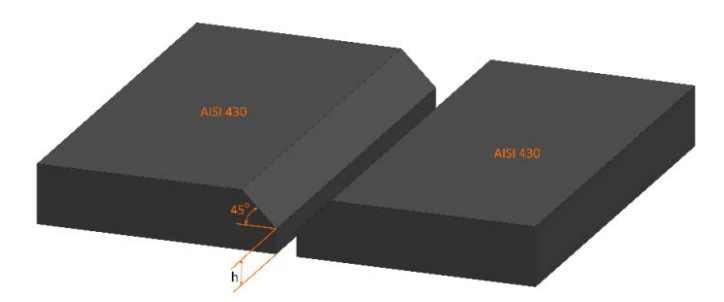


Figure 1. Preparation of the plates for welding trials.

W-14 T-:-1	Current	Voltage	Weld speed	Feeding rate of	Ch:-11:	
Weld Trial	(A)	(V)	(mm/s)	filler wire (mm/s)	Shielding gas	
Low Heat Input	ave. 385	28	4,5	17,5	Argon (99,95%)	
High Heat Input	ave. 465	27	4,0	17,5	Argon (99,95%)	

Table 2. The process parameters employed in welding.

One metallography specimen, two bend specimens and four tensile specimens were extracted from each joint in order to investigate the microstructural evolutions in the weld regions of the joints produced and to evaluate its influence on the mechanical properties. For comparison purposes and to evaluate the joint performance, four tensile specimens were also extracted from the base plate. The metallography specimens were first ground and polished prior to etching in which the specimens were immersed in a solution comprising of 50 ml HCl and 150 ml HNO3 for about 17 seconds. A detailed microstructural investigations were carried out on these specimens as well as microhardness measurements. Microhardness measurements were done on each joint along three lines across the weld region, using a load of 500 g, as schematically illustrated in Fig. 2.

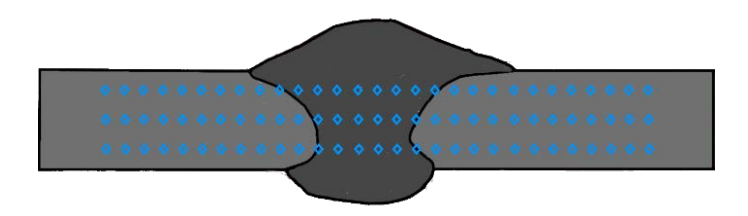


Figure 2. Schematic showing the conduction of microhardness measurements on each joint along three lines across the weld region.

Moreover, tensile test specimens of both the BM and the joints were tested with a loading rate of 15 mm/s to evaluate the mechanical properties, joint performance values and the weld qualities. Two bend specimens were also extracted from each joint in order to determine whether cracking occurs in the weld region of the joints produced using different heat input values. One of them was bent in the condition of surface bend and the other in the root bend configuration. The specimens were bent about 180 degrees and the weld center in the middle

position. Furthermore, the influence of heat input on the microstructural evolution in the HAZ and thus on mechanical behavior of the joints was also determined.

3. RESULTS AND DISCUSSION

The results obtained from this study will be discussed below in two subsections.

3.1. Microstructural Aspects

Figure 4 (a) shows the microstructure of the BM used in this study. The BM microstructure consists of a fully ferritic microstructure containing carbides, which are evenly distributed within the grains as well as along the grain boundaries. Figure 3 and 4 give macrograph and micrographs illustrating the weld cross-sections of the joints and the microstructures observed in the HAZ and FZ of the joints produced using low and high heat inputs, respectively. As seen from the micrographs, a fine dendritic structure was observed in the FZ of both joints. However, the grain size of dendritic structure is slightly coarser in the high heat input joint (Fig. 4c). This is not unexpected since high heat input applied during welding results in grain growth in the FZ.

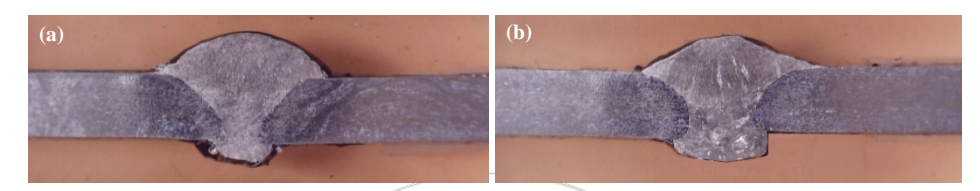


Figure 3. The macrographs illustrating the weld cross-sections of the welds produced: (a) the lower and (b) the higher heat input joint.

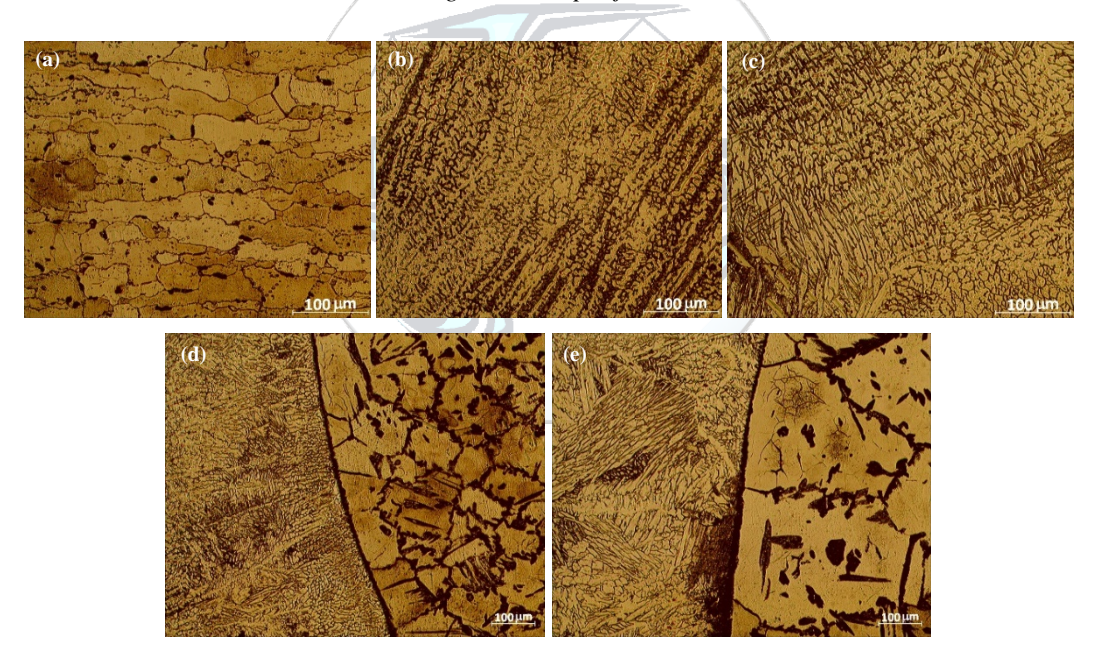


Figure 4. The micrographs illustrating the microstructures of: (a) BM, (b) and (c) FZ of the lower and higher heat input joint, respectively, and (d) and (e) HAZ of the lower and higher heat input joints, respectively.

Furthermore, it was observed that the BM microstructure was affected by solid state phase transformations induced by the weld thermal cycle in the HAZ of both joints. Thus, two distinct HAZ regions were formed in both joints, namely high temperature HAZ (so-called coarse grained HAZ, i.e. FGHAZ) and low temperature HAZ (often referred to fine grained HAZ, i.e FGHAZ) which is on the base metal (BM) side. Although both joints did exhibit CGHAZ next to the fusion boundary (FB), the extent of grain growth is much higher in the high heat input joint as clearly seen from Figs. 4(d) and (e). Martensite formation along the grain boundaries of ferrite phase and the growth of ferrite grains were detected in the HAZ region. Moreover, carbide precipitation along the fusion boundary was also observed in both joints. The grains were clearly much finer in the FGHAZ, and the grain size was almost the same as that of the BM, in contrast to CGHAZ where the grains are much coarser. Moreover, the evolution of intergranular martensites was also observed in the FGHAZ. However,

compared with CGHAZ, the amount of martensite was significantly less, and the martensite distributed discretely at the grain boundaries and no longer formed within the grains. The reason for this is the fact that the fine grain zone is far away from the FZ and the temperature is low. Thus, the formation of high-temperature austenite is suppressed, which inhibits martensite formation. The content of intergranular martensite and carbide precipitates along the fusion boundaries increases with an increase in heat input. Thus, the width of the HAZ also increases slightly with increasing heat input. According to Khorrami et al [42], the martensite formation in the HAZ of medium-Cr FSS joint is a well-known phenomenon. Van Warmelo et al [43] also proposed that the precipitates of carbides, nitrides or carbonitrides were usually formed in the HAZ of FSS. Moreover, Zou et al [7] reported that the dominant precipitate was Cr-rich carbide, i.e., M23C6 in which 'M' mostly stands for Cr and Fe. However, there is no clear indication of these precipitations in the HAZ of 430 FSS joints in the current study.

3.2. Mechanical Properties

Figure 5(a) and 5(b) gives the hardness profiles obtained from the joints produced using low and high heat inputs. These hardness profiles show the hardness variations across the joints. As clearly seen from these profiles, both joints displayed similar hardness variations across the weld region. The hardness profiles clearly show that there is a hardness increase (strength overmatching) in the weld region for both joints, particularly in the HAZ region. Thus, both joints display a typical hardness profile of strength overmatching joints. This hardness increase in the weld region of both joints is due to the formation of fine dendritic microstructure in the fusion zone (FZ) and the formation of intergranular martensite and growth of ferrite grains in the HAZ. Furthermore, the width of the HAZ in which hardness variation took place is wider in the higher heat input joint, indicating that the higher heat input has a significant effect on microstructure and thus on hardness across the weld region.

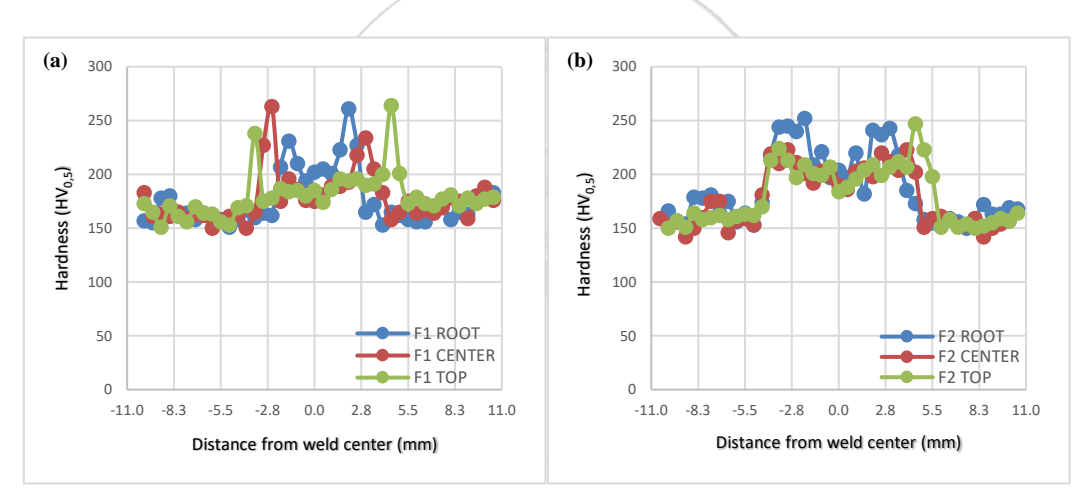


Figure 5. Hardness variation across the joints: (a) the lower heat input joint and (b) the higher heat input joint.

The results of tensile tests performed on the specimens of the BM and the joints produced using different heat input values are summarized in Table 3 and shown in Figure 6-7. Both welded joints showed good tensile strength and the failure took place at the BM away from the FZ for all samples. The tensile strength of both joints were very similar to that of the BM, Fig. 7. Thus, the tensile strength performance of both joints was found to be as high as 99%. On the other hand, both joints displayed lower ductility; i.e. about 15%, than that of the BM, i.e. 23%. This is not surprising since there is a strength overmatching in both joints as clearly illustrated by the hardness profiles. Thus, the higher strength weld region stays in the elastic region and does not contribute to the total elongation. This confined plasticity occurring only in the base plate sides of the tensile test specimen results in decreasing of the percentage elongation value. Similar results were also reported inhomogeneous welded joints, namely strength overmatched laser beam welded steels [28-30], strength undermatching Al-alloys joints [44-49] and bi-metallic joints showing confined plasticity [50,51]. Moreover, all the tensile specimens of the joints failed in the BM (in the region between fine grained HAZ and the base metal), as shown in Figure 8.

In contrast to tensile testing, the heat input variation employed in this study affected the joint behavior in bend testing. Although no cracking occurred in both surface and root bend specimens extracted from the lower heat input joint, the root bend specimen of the higher heat input joint has cracked as shown in Figures 9 and 10. The reason for this cracking is due to the presence of very coarse grains as well as martensite formation in the HAZ region next to the fusion line diminishing the toughness in this area (Fig. 4e).

Specimen	R _{P0.2} (MPa)	R _m (MPa)	Elongation (%)	Strength Performance (%)	Ductility Performance (%)	Failure Location
Base Plate	396, 392, 395 (394)	506,501,504 (504)	21, 25, 22 (23)			
Low Heat Input Joint	358, 364, 348, 354 (356)	498, 496, 495, 499 (497)	14, 15, 15, 15 (15)	99	65	Base plate
High Heat Input Joint	352, 300, 342, 341 (335)	497,496, 498, 503 (499)	15, 16, 14, 15 (15)	99	65	Base plate

Table 3. Tensile test results.

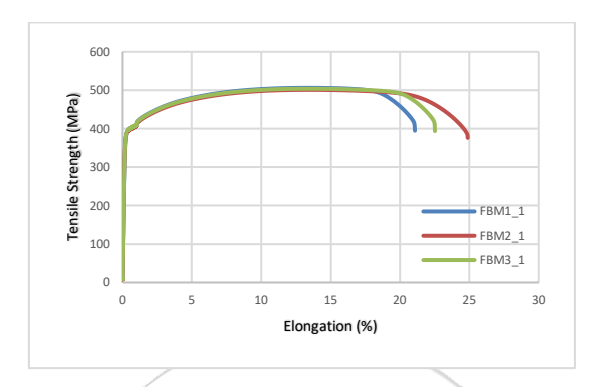


Figure 6. Stress-elongation (%) curve of the base plate AISI 304 steel used.

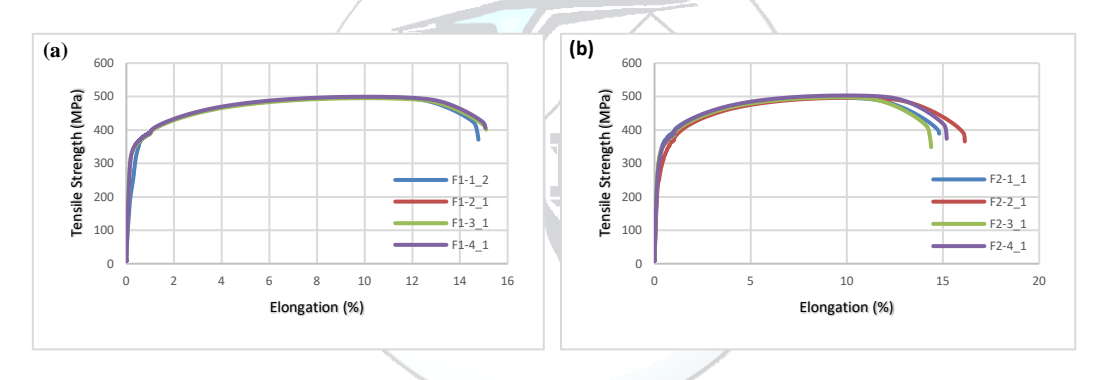


Figure 7. Stress-elongation (%) curves of: (a) lower heat input joint, and (b) higher heat input joint.

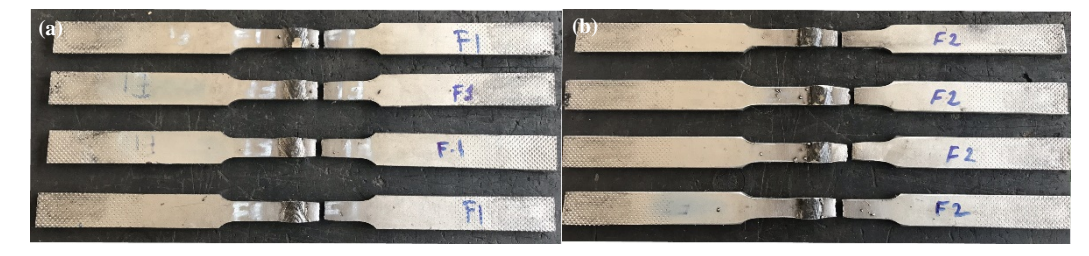


Figure 8. Macrographs showing the fracture locations in the tensile test specimens extracted from: (a) lower heat input joint and (b) higher heat input joint.

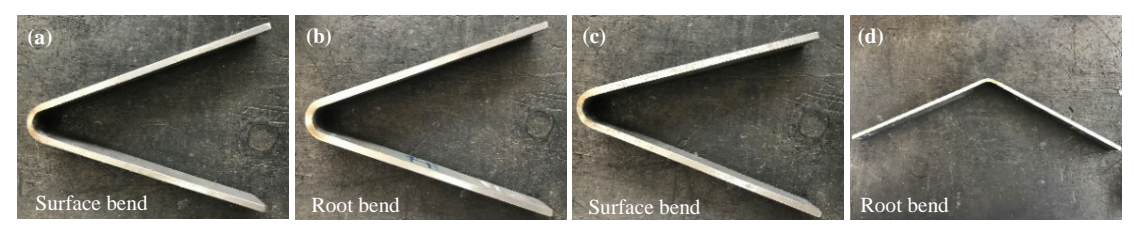


Figure 9. Macrographs showing the surface and root bend specimens extracted from: (a) lower heat input joint and (b) higher heat input joint. Note that no cracking occurred in any of the specimens.



Figure 10. Macrograph showing the failure location in root bend specimens extracted from the higher heat input joint. Note that failure takes place in the coarse grained HAZ (CGHAZ) region.

4. CONCLUSIONS

The weldability of AISI 430 plates with a thickness of 5 mm by GMAW welded using a filler wire of 307 with a diameter of 1.2 mm and the influence of heat input on the microstructural evolution in the joint area and thus on joint properties were investigated. The following conclusions were withdrawn from this study:

- AISI 430 plates with a thickness of 5 mm was defect-free welded in two passes by GMAW process.
- A fine dendritic microstructure was evolved in the fusion zone of both joints, although the grain size of the dendrites was slightly coarser in the higher heat input joint.
- Two distinct HAZ regions were formed in both joints namely coarse grained HAZ (CGHAZ) and fine grained HAZ (FGHAZ) regions.
- It was observed that the martensite formation along ferrite grain boundaries (intergranular martensites) and the coarsening of ferrite grains took place in the CGHAZ. However, no martesite was observed along the grain boundaries in the CGHAZ next to the fusion boundary. On the contrary, carbide precipitation was observed along the fusion boundaries of both joints.
- Both joints displayed a hardness increase in the weld region.
- All the tensile test specimens failed in the base plate. Both joints showed similar strength values to that
 of the BM, the strength performance of the joints being about 99%. However, the ductility performance
 was lower, i.e. about 65%, due to confined plasticity resulting from strength overmatching weld region.
 No clear indication of the influence of the heat input on joint performance has been observed in tensile
 loading condition.
- Both surface and root bend specimens extracted from lower heat input joint did not crack in bending
 test while the surface bend specimen did not crack but root bend specimen failed in the case of higher
 heat input joint, indicating that the heat input variation did in fact affect the joint behavior in bending
 condition. The results also indicate that the strength overmatching weld region cannot shield the
 cracking in root bend condition in the case of higher heat input joint.

ACKNOWLEDGMENT

We would like to thank Mr. Sedat UYSAL and Tuğrul YAZGAN from NOKSEL Çelik Boru Sanayi A.Ş. (Noksel Steel Pipe Inc.), İskenderun-Hatay, Turkey, for their support in conduction of the metallography and mechanical tests. The authors also thank Hikmet Gizem SARSILMAZ from Kahraman-Sarsılmaz Machinery, İskenderun, for conducting welds.

CONFLICT OF INTEREST STATEMENT

The authors declare that there is no conflict of interest.

REFERENCES

- [1]. N. Ghosh, P.K. Pal, G. Nandi, "GMAW dissimilar welding of AISI 409 ferritic stainless steel to AISI 316L austenitic stainless steel by using AISI 308 filler wire", *Engineering Science and Technology*, an *International Journal*, vol. 20, pp. 1334–1341, 2017.
- [2]. T. Mohandas, M.G. Reddy, M. Naveed, "A comparative evaluation of gas tungsten and shielded metal arc welds of a ferritic stainless steel", *J. Mater. Process. Technol.*, vol. 94, pp. 133-140, 1999.

- [3]. C. Lippold and D.J. Kotecki, Welding Metallurgy and Weldability of Stainless Steels. 1st ed., Hoboken: John Wiley & Sons Inc.; 2005.
- [4]. F.B. Pickering, "Physical metallurgy of stainless steel development", *Int. Met. Rev.*, vol. 21, pp. 227-268, 1976.
- [5]. R. Ghasemi, B. Beidokhti, M. Fazel-Najafabadi, "Effect of delta ferrite on the mechanical properties of sissimilar ferritic-austenitic stainless steel welds", *Arch. Metall. Mater.*, vol. 63 (1), pp. 437-443, 2018.
- [6]. S. Aguilar, R. Tabares, C. Serna, "Microstructural transformations of dissimilar austenite-ferrite stainless steels welded joints", *Journal of Materials Physics and Chemistry*, vol. 1 (4), pp. 65-68, 2013.
- [7]. J. Zhou, J. Shen, S. Hu, G. Zhao, Q. Wang, "Microstructure and mechanical properties of AISI 430 ferritic stainless steel joints fabricated by cold metal transfer welding", *Materials Research Express*, vol. 6 (11), Article No: 116536, 2019.
- [8]. P.D. Antunes, et al., "Mechanical and microstrutural characterization of weldments of ferritic stainless steel AISI 444 using austenitic stainless steels filler metals". *J. ASTM International*, vol. 9 (2), pp. 1-9, 2012.
- [9]. K. Shanmugam, A.K. Lakshminarayanan and V. Balasubramanian, "Tensile and impact properties of shielded metal arc welded AISI 409M ferritic stainless steel joints", *J. Mater. Sci. Technol.*, vol. 25 (2), pp. 181-186, 2009.
- [10]. A.K., Lakshminarayanan, "Effect of welding processes on tensile and impact properties, hardness and microstructure of AISI 409M ferritic ftainless joints fabricated by duplex stainless steel filler metal", *Journal of Iron and Steel Research, International*, vol. 16., pp. 66-72, 2009.
- [11]. N. Kashaev, V. Ventzke, and G. Çam, "Prospects of laser beam welding and friction stir welding processes for aluminum airframe structural applications", *Journal of Manufacturing Processes*, vol. 36, pp. 571-600, 2018.
- [12]. G. Çam and G. İpekoğlu, "Recent developments in joining of aluminium alloys", *Int. J. Adv. Manuf. Technol.*, vol. 91(5-8), pp. 1851-1866, 2017.
- [13]. G. Çam, "Friction stir welding (FSW) A novel welding technology developed for Al-Alloys", *Engineer and Machinery*, vol. 46 (541), pp. 30-39, Feb. 2005. (in Turkish)
- [14]. A. Von Strombeck, G. Çam, J.F. Dos Santos, V. Ventzke, and M. Koçak, "A comparison between microstructure, properties, and toughness behavior of power beam and friction stir welds in Al-alloys", in Proc. of the TMS 2001 Annual Meeting Aluminum, Automotive and Joining (New Orleans, Louisiana, USA, February 12-14, 2001), eds: S.K. Das, J.G. Kaufman, and T.J. Lienert, pub.: TMS, Warrendale, PA, USA, pp. 249-264, 2001.
- [15]. G. Çam, V. Javaheri, and A. Heidarzadeh, "Advances in FSW and FSSW of Dissimilar Al-Alloy Plates", *Journal of Adhesion Science and Technology*, 2022 (DOI: https://doi.org/10.1080/01694243.2022.2028073).
- [16]. G. İpekoğlu, B. Gören Kıral, S. Erim, and G. Çam, "Investigation of the effect of temper condition friction stir weldability of AA7075 Al-alloy plates", *Mater. Tehnol.*, vol. 46 (6), pp. 627-632, 2012.
- [17]. G. İpekoğlu, S. Erim, B. Gören Kıral, and G. Çam, "Investigation into the effect of temper condition on friction stir weldability of AA6061 Al-alloy plates", *Kovove Mater.*, vol. 51 (3), pp. 155-163, 2013.
- [18]. G. Çam, G. İpekoğlu, and H. Tarık Serindağ, "Effects of use of higher strength interlayer and external cooling on properties of friction stir welded AA6061-T6 joints", *Sci. Technol. Weld. Join.*, vol. 19 (8), pp. 715-720, 2014.
- [19]. G. Çam, S. Güçlüer, A. Çakan, and H.T. Serindağ, "Mechanical properties of friction stir butt-welded Al-5086 H32 plate", *Mat.-wiss. u. Werkstofftech.*, vol. 40 (8), pp. 638-642, 2009.
- [20]. A. Heidarzadeh, et al., "Friction stir welding/processing of metals and alloys: A comprehensive review on microstructural evolution", *Progress in Materials Science*, vol. 117, Paper No. 100752, 2021.
- [21]. T. Küçükömeroğlu, E. Şentürk, L. Kara, G. İpekoğlu, and G. Çam, "Microstructural and mechanical properties of friction stir welded nickel-aluminum bronze (NAB) alloy", *Journal of Materials Engineering and Performance (JMEPEG)*, vol. 25 (1), pp. 320-326, 2016.
- [22]. G. Çam, S. Mistikoglu, and M. Pakdil, 'Microstructural and mechanical characterization of friction stir butt joint welded 63%Cu-37%Zn brass plate', *Weld. J.*, vol. 88 (11), pp. 225s-232s, 2009.
- [23]. G. Çam, H.T. Serindağ, A. Çakan, S. Mıstıkoğlu, and H. Yavuz, 'The effect of weld parameters on friction stir welding of brass plates', *Mat.-wiss. u. Werkstofftech.*, vol. 39 (6), pp. 394-399, 2008.1997.
- [24]. A. Günen, E. Kanca, M. Demir, F. Çavdar, S. Mistikoğlu, and G. Çam, "Microstructural and mechanical properties of friction stir welded pure lead", *Indian Journal of Engineering & Materials Sciences (IJEMS)*, vol. 25 (1), pp. 26-32, 2018.
- [25]. G. Çam, "Friction stir welded structural materials: Beyond Al-alloys", *Int. Mater. Rev.*, vol. 56 (1), pp. 1-48, 2011.
- [26]. G. Çam, G. İpekoğlu, T. Küçükömeroğlu, and S.M. Aktarer, "Applicability of friction stir welding to steels", *JAMME*, vol. 80(2), pp. 65-85, 2017.
- [27]. S. Selvi, A. Vishvaksenan, and E. Rajasekar, "Cold metal transfer (CMT) technology An overview", Cold metal transfer (CMT) technology An overview, *Defence Technology*, vol. 14, pp. 28-44, 2018.

[28]. G. Çam, Ç. Yeni, S. Erim, V. Ventzke, and M. Koçak, "Investigation into properties of laser welded similar and dissimilar steel joints", *Sci. Technol. Weld. Join.*, vol. 3 (4), pp. 177-189, 1998.

- [29]. J. dos Santos, G. Çam, F. Torster, A. Insfran, S. Riekehr, V. Ventzke, and M. Koçak, "Properties of power beam welded steels, Al- and Ti-alloys: Significance of strength mismatch", *Welding in the World*, vol. 44 (6), pp. 42-64, 2000.
- [30]. G. Çam, M. Koçak, and J.F. dos Santos, "Developments in laser welding of metallic materials and characterization of the joints", *Welding in the World*, vol. 43 (2), pp. 13-26, 1999.
- [31]. G. Çam, et al., "Characterization of laser and electron beam welded Al-alloys", *Prakt. Metallogr.*, vol. 36 (2), pp. 59-89, 1999.
- [32]. G. Çam and M. Koçak, "Microstructural and mechanical characterization of electron beam welded Al-alloy 7020", *J. Mater. Sci.*, vol. 42 (17), pp. 7154-7161, 2007.
- [33]. G. Çam, V. Ventzke, J.F. dos Santos, M. Koçak, G. Jennequin, and P. Gonthier-Maurin, "Characterisation of electron beam welded aluminium alloys", *Sci. Technol. Weld. Join.*, vol. 4 (5), pp. 317-323, 1999.
- [34]. T. Küçükömeroğlu, et al., "Investigation of mechanical and microstructural properties of friction stir welded dual phase (DP) steel", *IOP Conf. Series: Mater. Sci. Eng.*, vol. 629, Paper No. 012010, 2019.
- [35]. G. İpekoğlu, T. Küçükömeroğlu, S.M. Aktarer, D.M. Sekban, and G. Çam, "Investigation of microstructure and mechanical properties of friction stir welded dissimilar St37/St52 joints", *Materials Research Express*, vol. 6 (4), Article Number: 046537, 2019.
- [36]. T. Küçükömeroğlu, S.M. Aktarer, G. İpekoğlu, and G. Çam, "Mechanical properties of friction stir welded St 37 and St 44 steel joints", *Materials Testing*, vol. 60 (12), pp. 1163-1170, 2018.
- [37]. T. Küçükömeroğlu, S.M. Aktarer, G. İpekoğlu, and G. Çam, "Microstructure and mechanical properties of friction stir welded St52 steel joints", *International Journal of Minerals, Metallurgy and Materials*, vol. 25 (12), pp. 1457-1464, 2018.
- [38]. L. Cui, H. Fujii, N. Tsuji, and K. Nogi, "Friction stir welding of a high carbon steel", *Scripta Mater.*, vol. 56, pp. 637-40, 2007.
- [39]. Y. Azuma, Y. Kameno, and T. Takasugi, "Friction stir welding in stainless steel sheet of type 430 using Ni-based dual two-phase intermetallic alloy tool", *Welding International*, vol. 27 (12), pp. 929-935, 2013.
- [40]. B.W. Ahn, D.H. Choi, D.J. Kim, and S.B. Jung, "Microstructures and properties of friction stir welded 409 L stainless steel using a Si3N4 tool", *Mater. Sci. Eng. A*, vol. 532, pp. 476-479, 2012.
- [41]. A.K. Lakshminarayanan, V. Balasubramanian, "An assessment of microstructure, hardness, tensile and impact strength of friction stir welded ferritic stainless steel joints", Mater. Des., vol. 31, pp. 4592-4600, 2010.
- [42]. M.S. Khorrami, et al., "Study on microstructure and mechanical characteristics of low-carbon steel and ferritic stainless steel joints", *Materials Science & Engineering A*, vol. 608, pp. 35-45, 2014.
- [43]. M. van Warmelo, D. Nolan, and J. Norrish, "Mitigation of sensitisation effects in unstabilised 12%Cr ferritic stainless steel welds", *Materials Science & Engineering A*, vol. 464, pp. 157-169, 2007.
- [44]. G. İpekoğlu and G. Çam, "Formation of weld defects in cold metal transfer arc welded 7075-T6 plates and its effect on joint performance", *IOP Conf. Series: Materials Science and Engineering*, vol. 629, Paper No: 012007, 2019.
- [45]. M. Pakdil, G. Çam, M. Koçak, and S. Erim, "Microstructural and mechanical characterization of laser beam welded AA6056 Al-alloy", *Mater. Sci. Eng. A*, vol. 528 (24), pp. 7350-7356, 2011.
- [46]. Y. Bozkurt, S. Salman, and G. Çam, "Effect of welding parameters on lap-shear tensile properties of dissimilar friction stir spot welded AA5754-H22/2024-T3 joints", *Sci. Technol. Weld. Join.*, vol. 18 (4), pp. 337-345, 2013.
- [47]. G. İpekoğlu and G. Çam, "Effects of initial temper condition and postweld heat treatment on the properties of dissimilar friction-stir-welded joints between AA7075 and AA6061 aluminum alloys", *Metall. Mater. Trans. A*, 2014, Vol. 45A (7), pp. 3074-3087
- [48]. G. İpekoğlu, S. Erim, and G. Çam, "Investigation into the influence of post-weld heat treatment on the friction stir welded AA6061 Al-alloy plates with different temper conditions", *Metall. Mater. Trans. A*, vol. 45A (2), pp. 864-877, 2014.
- [49]. G. İpekoğlu, S. Erim, and G. Çam: "Effects of temper condition and post weld heat treatment on the microstructure and mechanical properties of friction stir butt welded AA7075 Al-alloy plates", *Int. J. Adv. Manuf. Technol.*, vol. 70 (1), pp. 201-213, 2014.
- [50]. M. Koçak, M. Pakdil, and G. Çam, "Fracture behaviour of diffusion bonded Ti-alloys with strength mismatch", *Sci. Technol. Weld. Join.*, vol. 7 (4), pp. 187-196, 2002.
- [51]. G. Çam, M. Koçak, D. Dobi, L. Heikinheimo, and M. Siren, "Fracture behaviour of diffusion bonded bimaterial Ti-Al joints", *Sci. Technol. Weld. Join.*, vol. 2 (3), pp. 95-101, 1997.

Classification of Live / Lifeless Assets from Long Distance with Laser Signals by Using Deep Learning Network

Nevzat Olgun^{1*}, İbrahim Türkoğlu²

¹ Zonguldak Bulent Ecevit University, Department of Computer Technologies, 67800, Devrek/Zonguldak, Türkiye.

²Firat University, Department of Software Engineering, 23200, Merkez/Elazığ, Türkiye.

*Corresponding Author email: nevzat.olgun@beun.edu.tr

Abstract

In counter-terrorism, urban warfare operations and active combat environments, some targets may be live people, while some targets may consist of fake materials such as mannequins. Determining whether these targets are alive or not is important for human life. In addition, it is important to determine whether the instruments used in the biometric verification steps belong to a real living thing. In this study, it is aimed to classify the determined targets as live/lifeless with low-power laser signals in situations where people cannot be reached directly. For this purpose, people as living samples and different types of lifeless materials at a certain distance were pointed with a low-powered laser light source and laser signals reflected from the targets were recorded with the receiving system. In the classification of Live / Lifeless, human vitality and other materials (non-living) in nature are compared. In the study, laser signal samples are taken from different points of the arm of 9 volunteer men for living assets and 17 materials frequently used by people for lifeless assets. For lifeless assets, often found in nature, aluminum, black, fabric, frosted glass, glass, pottery, iron, galvanize, granite, linden, magnet, mdf, marble, cardboard, polyethylene, polystyrene, PVC and artificial marble are selected. The laser signals obtained from the targets are classified as live/lifeless by undergoing training in Long-Short Term Memory networks after preprocessing and feature extraction steps. As a result of the study, a live / lifeless assets distinction is made with an accuracy rate of 99.7%.

Key words

Laser, Laser Signs, Deep Learning, Liveness Detection, Live Detection, Target Detection

1. INTRODUCTION

It is important to determine the vitality of the elements on the enemy front line in active war environments, in the fight against terrorism and in urban warfare operations. In some cases, mannequin and similar materials are used in the elements on the enemy line and if this can be detected remotely, significant gains can be achieved. In such cases, it is important to determine the presence of live / inanimate assets of the target from far distances with laser signals. Similarly, if real live targets can be detected in hostage operations, many lives can be saved.

In addition, in biometric security systems, it is important to detect vitality in order to determine whether the fingerprint, photograph, retina belong to a living person. In this way, interference that imitates a person's biometric

data can be detected and necessary precautions can be taken. Printed photographs of the human face, patterns for fingerprints, and 3D masks for face detection are frequently used to overcome biometric measures [1–3].

Many studies have been carried out on viability detection in the literature. Some of these studies focused on radio frequency, some on cameras, and some on lasers. In the literature, there are studies on the localization of a person behind the wall with the wall radar and signs of life [4–7]. The focus of such studies is to take advantage of the micro-doppler characteristic caused by small vibrations in the body during human breathing. In such systems, a radio frequency signal is sent to the body, and when the signal reaches the body, small displacement information is returned as a phase shift signal due to breathing or heartbeat movement.

In vitality detection studies with a camera, methods such as obtaining heart rate information, detecting blinking movements, detecting facial mimics, color gradient features are frequently used [1–3,8–20]. In vitality detection applications where camera systems are used, the system fails in insufficient light conditions or in cases where there is no light at all.

One of the techniques used in vitality detection that allows for non-contact measurement is the use of lasers. Lasers have also become an important tool for optical remote sensing due to their ability to produce an intense amount of parallel beam consisting of monochromatic, coherent and polarized light. For the first time, there have been great developments in the production techniques of lasers produced using ruby crystal over time, and varieties operating at different wavelengths, different output powers and different pulse times have emerged [21]. According to the material used in the production of lasers, they are divided into four groups as gas lasers, liquid lasers, solid state lasers and semiconductor (diode) lasers. While lasers used in continuous wave form transmit a relatively low amount of energy to the target continuously, lasers in pulsed wave form can transmit instantaneously higher energy to the target at certain intervals. Diode lasers are small in size and low cost, they can be produced at different output powers and different wavelengths. Because of these advantages, they are frequently used in chemical analysis, remote sensing, medical applications, defense technologies, telecommunications and industry [22].

When laser light is reflected on a target object, it is partially reflected, partially transmitted, or partially absorbed from the target. Laser beams reflected from the target can be measured and converted into signals with the help of high gain coefficient avalanche photo diodes in electro-optic devices. Due to the fact that different types of targets exhibit scattering and absorption properties in different ways, it is possible to obtain information about many types of living/lifeless targets around us using laser signals reflected from targets.

Very small amounts of mechanical vibrations can be measured with laser interferometers [23–27]. With traditional Michelson interferometer-based laser vibration meters, it can measure heartbeats and skin changes during breathing at close range [28–30]. Such interferometers require stable optical setup and are not suitable for use outside the laboratory. Laser Doppler Vibrometers (LDV) are laser vibration meters that are widely used in measuring small vibrations and are also commercially available on the market [31]. In a study with LDV, vibrations in the chest wall as a result of beating of the heart were measured and the results were associated with ECG [32]. In another study, the vibrations of the skin surface in the neck are studied depending on the cardiac rate[33,34]. Qu et al. have worked on the detection of human voice using pan-tilt-zoom (PTZ) camera and LDV. In this study, they focused on the detection of the moving person with the PTZ camera and the orientation of the LDV on the moving person for sound detection with LDV [35].

Marchionni et al. used LDV to measure heart and lung activities from a distance of about 2 m in preterm children[36]. Takano et al., in their study, reflected a laser beam on the subjects' face and recorded the laser spots formed for 30 seconds with a time-lapse camera. They extracted the subjects' heart rate information from the video recordings [37]. Ozana et al., in their study on farm animals, projected a laser light source to the targets and recorded the laser spots on the target with a 500-fps camera. They obtained the heart rate and respiratory information of the subjects with the signal processing methods from the video they recorded [38].

In the previous studies carried out by our team, a single laser light source and receiver system are used to classify different types of lifeless materials at a distance [39,40].

In this study, when health teams such as earthquakes, floods, storms, war environments and falls from height cannot reach the patient directly, or when it is necessary to determine the viability of elements on the enemy front line in a combat environment, it is necessary to collect information with low power laser signs from the specified target and in the light of the information obtained, it is intended to be classified as life/lifeless. In the classification of live/lifeless, human vitality and other materials (non-living) in nature are compared. Within the scope of the study, laser signals are obtained from a certain distance from live and lifeless targets, the obtained signals are classified as live/lifeless by undergoing training in Long-Short Term Memory networks (LSTM) after preprocessing and feature extraction steps and the results are examined.

When the literature is examined, it is seen that cameras are generally used in livelihood detection studies. Ambient light plays an important role in systems where cameras are used. In low lighting conditions, the performance of

the systems made with the camera decreases. In cases where there is insufficient or no ambient light, camera systems become completely inoperable. With the proposed system, an active measurement method using only laser light is presented. This study with laser light has the potential to be less affected by lighting conditions. The main contributions of this study are as follows.

- Live/lifeless classification was made using a laser signal and deep learning architecture based on a single measurement point.
- A faster classification time was obtained by using reduced size laser signals instead of raw laser signals in the detection of live/lifeless.
- Classification of different types of lifeless assets and a living human tissue was performed based on laser signals and deep learning.

2. RELATED WORKS

In this section, general information about the basics of laser measurement technique, which is the basis of the distinction between living tissue and lifeless materials, and the deep learning model used in classification are given.

2.1. Interaction of laser light with materials and living tissue

When laser beams are reflected on the surface of a material, they make specular or diffuse reflections depending on the surface roughness of the material. When the amount of roughness on the surface of the material is smaller than the wavelength of the laser light reflected on the material, specular reflection will occur, otherwise diffuse reflection will occur [40]. In cases where there is diffuse reflection, subsurface scattering occurs. Under natural conditions, many materials have a certain amount of rough surface due to the micro-textures on their surface. In this case, the laser beams reflected on the material reflect as a combination of specular and diffuse reflection. Figure 1 shows specular and diffuse reflection patterns of laser beams from the material surface. As can be seen in Figure 1, subsurface scattering can also occur in diffuse reflections. Since each material type has different surface textures and different microstructures, the laser signals reflected from the materials will also be different.

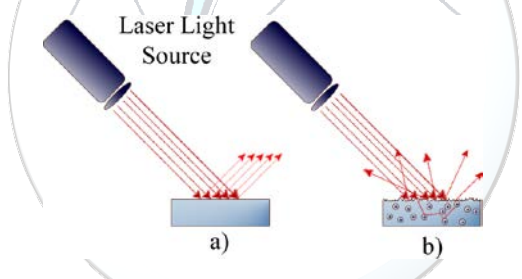


Figure 1. Laser beams and reflection types a) Specular reflection from a smooth surface b) Diffuse reflection and subsurface scattering from a rough surface

Lasers are in different wavelengths according to the production technique. Laser beams of different wavelengths and different optical output power can cause different effects on living tissues. When laser beams are projected onto a tissue, they show reflection, absorption, transmission and scattering [41]. Depending on the wavelength, the interaction of laser beams with living tissue can also be a mixture of them. Figure 2 shows the interaction of laser beams with living tissue. In this study, laser signals reflected from living tissue were used. The reflection amount of laser beams between 300-1100nm wavelength in soft tissues is 10 times higher than absorption.

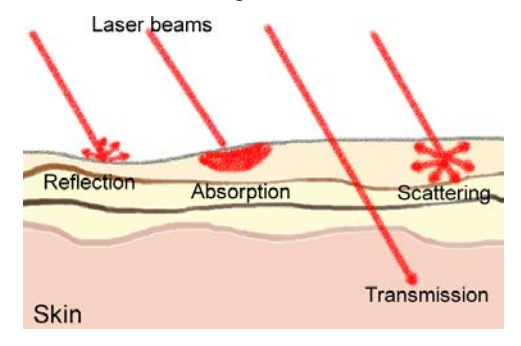


Figure 2. Interaction of laser beams with living tissue. Depending on the characteristics of the laser and the living tissue, the laser beam reflects, absorbs, transmits or scatters.

2.2. Deep learning: LSTM model

The use of Deep learning algorithms has started to increase in many areas such as object recognition, signal processing, natural language processing. Deep learning is a type of artificial neural networks (ANN). The most important step in artificial neural networks and other machine learning algorithms is extracting properties from raw data [42]. This step is no longer required with use of deep learning networks. Deep learning networks can extract features from the raw data given to them due to their structure and transfer this important data as an input to the next layer [43].

Deep learning networks consist of different architectures according to the areas in which they are used. Convolutional neural networks (CNN) are often used in image processing and similar fields [42,44]. In addition, CNNs are used in signal processing [45,46]. Recurrent neural networks (RNN) architecture is frequently used in signal processing, natural language processing, and time series data processing [47–50]. RNN focuses on the relationship between the data in the input sequence given to it. Cells in this architecture use their outputs as input in the next process. In this case, the output of each cell depends on the previous output. A simple RNN cell and its expansion can be seen in Figure 3.

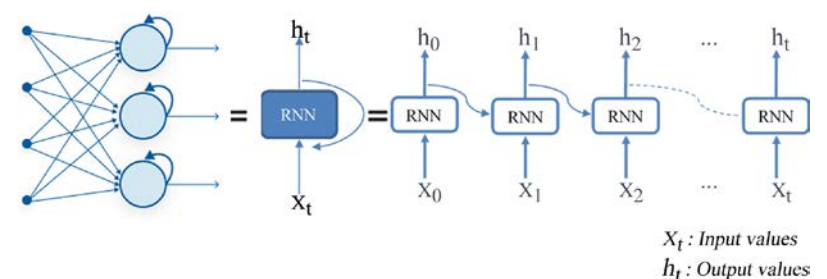


Figure 3. RNN cell and its expansion

RNN architecture succeeds in short-term dependencies but fails in long-term dependencies. Hochreiter et al. reported that the problem related to learning of long-term dependencies in RNN architecture was solved in their study made in 1997. This structure similar to RNN is called Long Short-Term Memory networks (LSTM). LSTM consists of a memory cell that can protect its state over time and non-linear gates regulating data input/output in the cell [40,51]. Input, forget, and output gates in an LSTM cell is interconnected by 4 neural networks and they form the cell memory. LSTM model, gates in its structure as well as the internal structure of an LSTM cell can be seen in Figure 4.

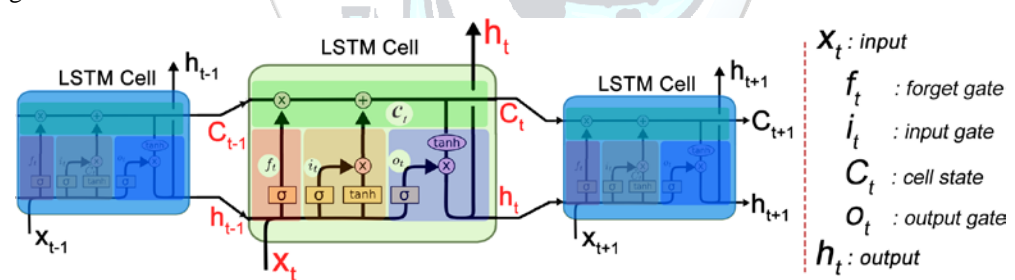


Figure 4. LSTM model, gates in its structure and the internal structure of the LSTM cell

In LSTM cell model shown in Figure 4, out of the forget gate is represented by f_t , out of the input gate by i_t whereas out of the output gate is represented by o_t , the cell state by C_t and out of the cell by h_t . f_t , i_t , C_t , o_t and h_t are defined in Eq. 1 - 5. Weights are represented by W_f , W_i , W_c , W_o , bias values are represented by b_f , b_i , b_c , b_o [40].

$$f_t = \sigma(W_f \cdot [h_{t-1}, x_t] + b_f) \tag{1}$$

$$i_t = \sigma(W_i \cdot [h_{t-1}, x_t] + b_i) \tag{2}$$

$$C_t = f_t * C_{t-1} + i_t * [tanh(W_c \cdot [h_{t-1}, x_t] + b_c)]$$
(3)

$$o_t = \sigma(W_0 \cdot [h_{t-1}, x_t] + b_0) \tag{4}$$

$$h_t = o_t * tanh(C_t) \tag{5}$$

3. MATERIALS AND METHODS

3.1. Experimental Setup and Data Collection

Laser meter module that emits red light at 1 mW output power and 650 nm wavelength is used in the scope of the study. The firmware of the laser meter module is reprogrammed to take 3000 raw laser mark samples per measurement and transfer them to the computer via the serial port [39]. Different points of the live / lifeless targets in the laboratory environment are pointed with the laser light source on the cartesian robot arm in line with the coordinates coming from the computer program, and the laser signals reflected from the target are detected by the device and transferred to the computer system. The distance between the laser light source and the targets is chosen as 2 meters. In Figure 5, the sensor module consisting of the experimental study setup, laser light source and optical device are shown.

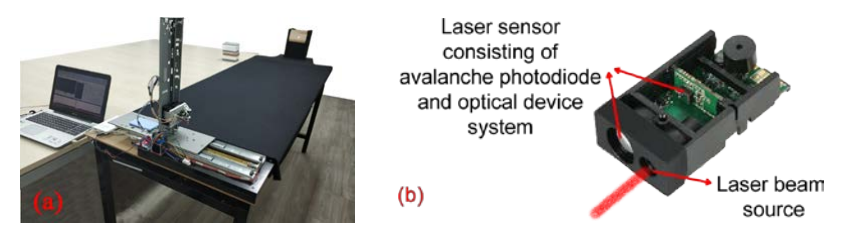


Figure 5. a) Experimental work setup.

b) Laser light source and optical system.

In the study conducted during daylight hours, 130 laser signal samples are taken from different points of the arm of 9 volunteer men for live assets, and 69 laser signal samples from different points of 17 materials frequently used by people for lifeless assets. Aluminum, black fabric, frosted glass, glass, pottery, iron, galvanize, granite, linden, magnet, mdf, marble, cardboard, polyethylene, polystyrene, pvc and artificial marble are selected for lifeless assets. In Figure 6, the visuals of the materials used in the study and the position of living and inanimate beings in the experimental setup are shown. In addition, before each measurement, measurements are made by turning off the laser light to detect white noise caused by the device and daylight. At the end of the data collection process, a total of 1170 laser signals are obtained from the arms of male subjects and a total of 1170 laser signals from lifeless assets.

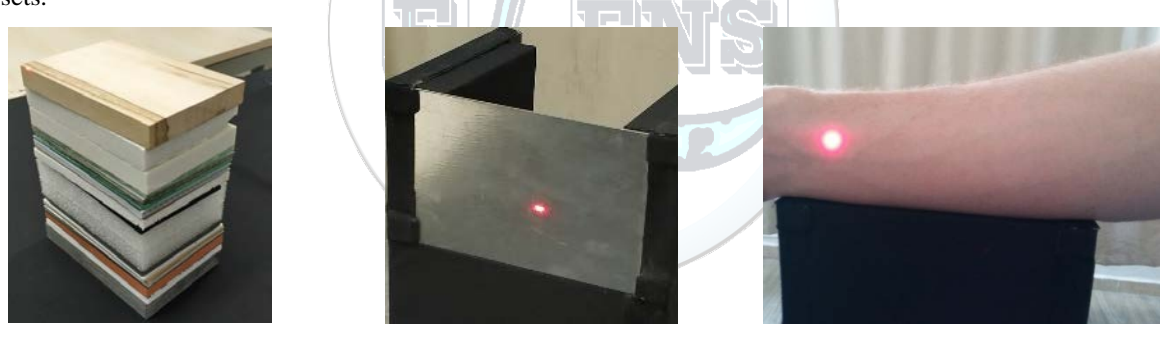


Figure 6. Images of the materials used in the study and the position of live/lifeless assets in the experimental system.

3.2. Signal Processing and Deep Learning

The study consists of steps for data collection, data preparation and classification. Figure 7 shows the block diagram of the study.

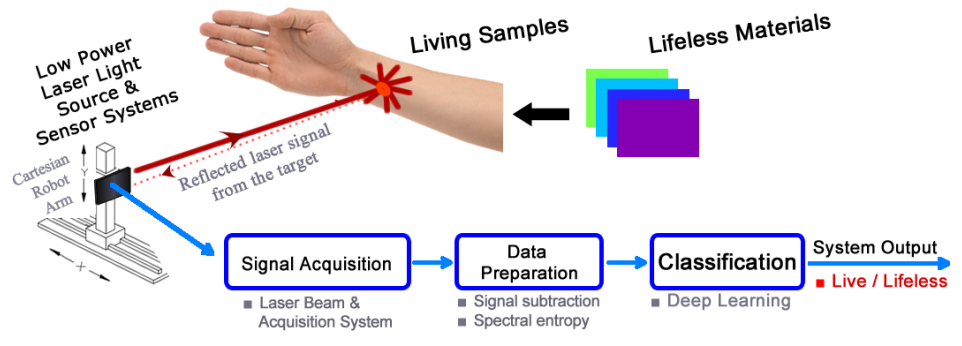


Figure 7. Block diagram of the study

In the preprocessing step of the study, the subtraction process defined in Equation 6 is performed to separate the environment & system noise signals from the laser signals obtained from live and lifeless assets.

$$x(n) = s(n) - d(n) \tag{6}$$

In Equation 6, x(n) refers to the noise-free laser signal, s(n) refers to the noisy laser signal, and d(n) refers to the environment & system noise signals. In Figure 8, the raw laser signals of the male subject's arm, aluminum, linden(wood) and pottery are seen, environment & system noise signals are seen and the laser signals as a result of the subtraction process are seen.

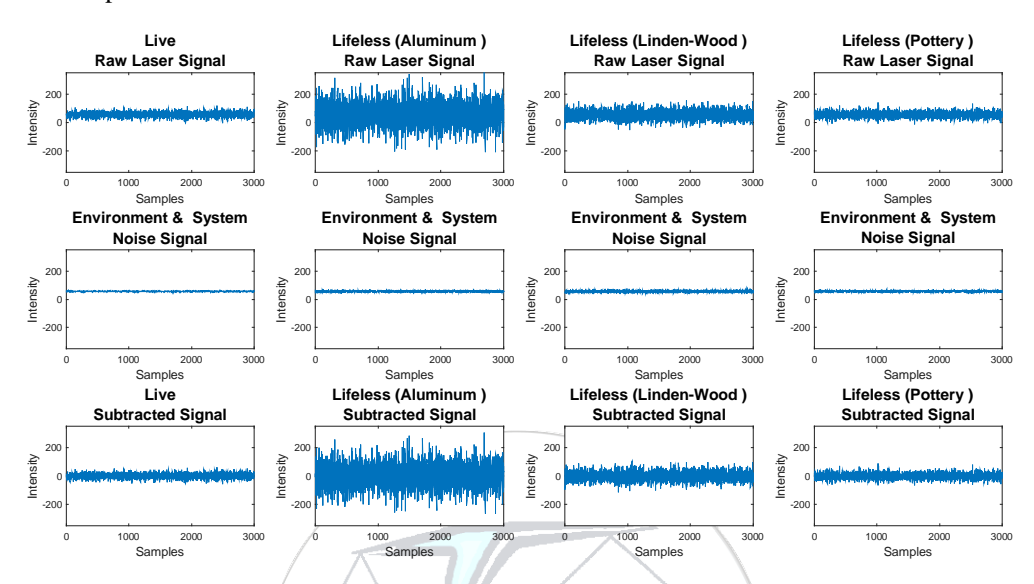


Figure 8. Raw laser signals of live, lifeless(aluminum), lifeless(linden), lifeless(pottery) materials, environment & system noise signals and the laser signals as a result of the subtraction process

The normalized energy distribution graph of the raw laser signals obtained after subtracting the background noise signals from the raw signals obtained from living and lifeless assets is given in Figure 9.

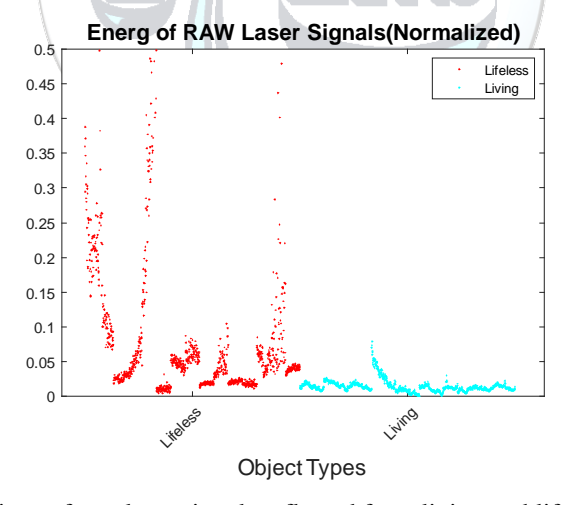


Figure 9. Energy distributions of raw laser signals reflected from living and lifeless assets after subtraction process

The spectral power density is based on the process of estimating the power distribution in the frequency band of the signal. This process is based on the Fourier transform. Welch method is an advanced version of this method [31]. The Welch spectral power density is explained as in Equation 7.

$$P_{w} = \frac{1}{l} \sum_{i=0}^{l-1} \check{S}_{xx}^{i}(f) \tag{7}$$

In Equation 7, P_w shows Welch spectral power density, $S_{xx}^i(f)$ shows the i^{th} improved periodogram of spectral power density, and l shows the length of the signal. In the study, Welch spectral power density is applied to laser signals following subtraction process. Figure 10 shows the laser signals with subtraction process and laser signals with Welch spectral power density applied.

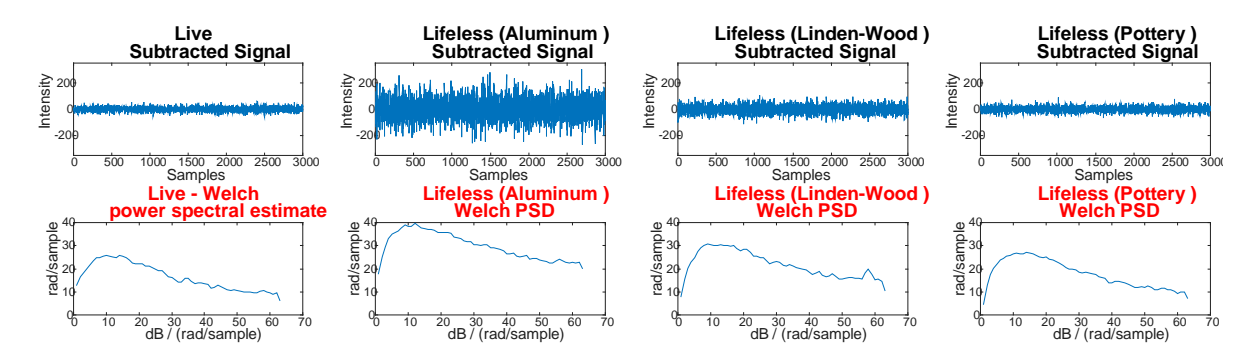


Figure 10. Preprocessed laser signals for live, lifeless(aluminum), lifeless (galvanize) materials and laser signals with Welch spectral power density applied

In the study, a bidirectional LSTM architecture consisting of 64 hidden layers are used to classify laser signals from a total of 2340 live/lifeless assets obtained as a result of signal processing steps. Figure 11 shows the LSTM architecture used in the study. In the study, the number of hidden layers, layer structures and hidden unit numbers in the layers were selected by trial-and-error method.

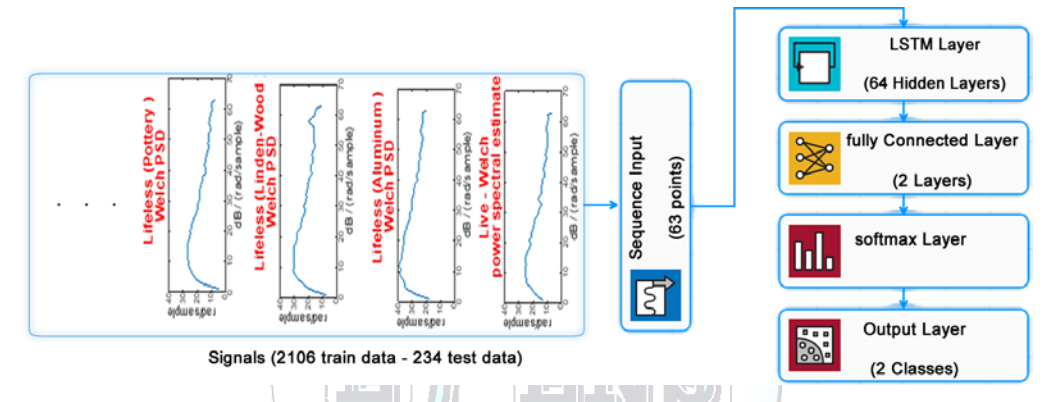


Figure 11. LSTM architecture used in the study

3.3. Performance Evaluation

In this study, the performance of the proposed model was evaluated using a 10-fold cross validation technique. This technique avoids obtaining biased results in validation results [52]. The data set obtained was randomly divided into 10 equal parts so that the amount of data in each class was equal. While 9 parts of the data set divided into parts were used for training the model, the remaining part was used for the performance test of the model. This process was done for all parts of the data set and the overall performance of the system was found by averaging the results obtained from the test results. The graphical model of training and test data according to the 10-fold cross-validation technique can be seen in Figure 11.

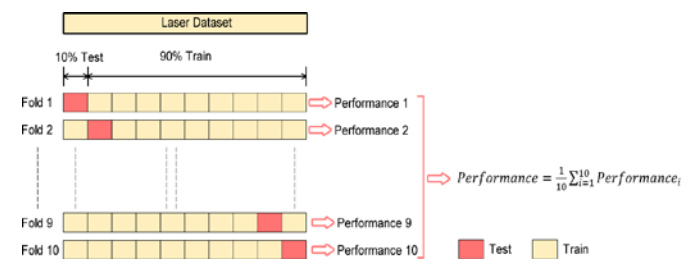


Figure 11. Graphical model of training and test data according to 10-fold cross validation technique.

Classification accuracy was used to compare the proposed system with existing studies. It is extremely important to use the same performance criteria to make comparative assessments with existing studies. Most of the existing studies use accuracy criteria in classification. Considering the accuracy criterion is a reasonable criterion in studies where the data set is balanced. The accuracy criterion can be defined as the ratio of the estimates that the classifier makes correctly to all estimates. The accuracy of the proposed method can be calculated as in Eq. 8.

$$Accuracy = \frac{TP + TN}{TP + TN + FP + FN} \tag{8}$$

True positive (TP), true negative (TN), false positive (FP), and false negative (FN) were taken as basis for the calculation of accuracy performance criteria. In this study, precision, recall and F-score evaluation criteria were used as well as accuracy performance criteria. These definitions are shown in the following equations [53].

$$precision = \frac{TP}{TP + FP} \tag{9}$$

$$recall = \frac{TP}{TP + FN} \tag{10}$$

$$F - score = 2 * \frac{precision * recall}{precision + recall}$$
(11)

4. RESULTS AND DISCUSSION

In LSTM architecture, which is used for classification of live and lifeless assets, the data set is divided into 10 equal parts, and the remaining data is used for training at a time. The hyper parameters used for the training of the LSTM network were determined as the maximum epoch number of 100, the learning rate 0.001, and the optimization algorithm Adam. Mini-batch size was chosen as 256.

The length of the raw laser signals obtained from the experimental studies consists of 3000 points. Measurements were taken with the laser beams on and off to eliminate environment/device noise. During the data preparation phase, these signals were subtracted from each other and the noise in the signals was removed. As it is known, processing high-dimensional signals in deep learning models is time consuming and costly. For this reason, the noise-free raw laser signals were converted into signals of much smaller size (63 points) by calculating the Welch spectral power densities. In the experimental studies, the reduced size laser signals were trained separately in 16, 32, 64, 128 hidden layer LSTM networks and their performances were compared. The calculation time of a signal from the raw laser signal according to the Welch method took 0.026 s.

Training of reduced size laser signals in the LSTM model significantly increases the performance and speed of the system. With the reduction of the data size, the training time in the 64 hidden layer LSTM network takes 0.55 seconds per epoch. Average classification results, training times and LSTM hidden layer numbers of the reduced size laser signals are given in Table 1.

Table 1. Hidden layers, average classification results and training times of laser signals with reduced dimensions.

LSTM Hidden Layer	16	32	64	128
Training time (1 epoch)	0.39 s	0.44 s	0.55 s	0.87 s
Recall	% 97.42 ± 4.38	99.29 ± 0.81	$\%$ 99.70 \pm 0.45	$\%$ 99.49 \pm 0.44
Precision	$\%97,39 \pm 4,42$	$\%99.27 \pm 0.83$	$\%99.70 \pm 0.45$	$\%99.49 \pm 0.44$
F1-score	% 97,41± 4,40	$\%$ 99.28 \pm 0.82	$\%$ 99.70 \pm 0.45	$\%$ 99.49 \pm 0.44
Accuracy	% 97.39 ± 4.42	% 99.27 ± 0.83	% 99.70 ± 0.45	% 99.49 ± 0.44

After the training of the network, the classification performance in the test data is calculated as the lowest 98.72%, the highest 100% and the average performance is 99.70%. Figure 12 shows the confusion matrix of the highest training and test performance of the 64 hidden layers LSTM network.

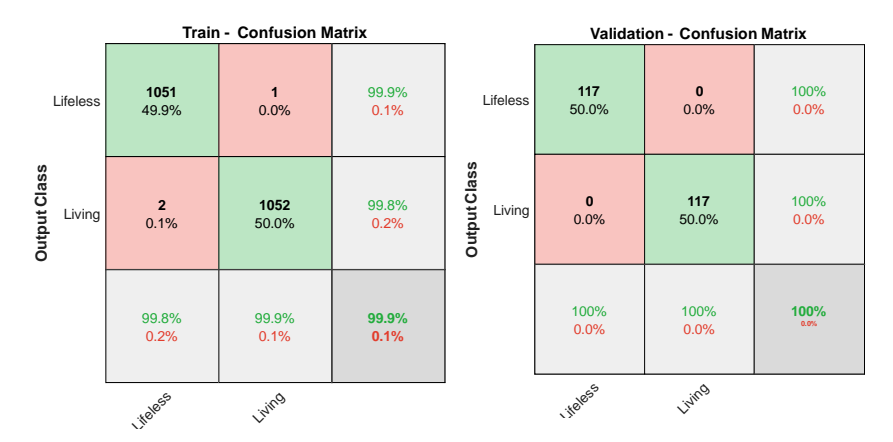


Figure 12. Confusion matrix showing the highest results in the classification performance of live and lifeless assets.

In this study, it is aimed to classify the target determined by low-power laser signals from a certain distance as live/lifeless when it is necessary to detect the vitality of the elements on the enemy front line in the war environment or to determine whether the people using biometric verification systems are real people. For this purpose, laser signals are obtained from the arms of the volunteer subjects and 17 materials, the laser signals obtained are passed through the signal processing steps and they are trained and classified using the LSTM architecture used in deep learning networks. With the proposed system, a high performance of 99.70% has been achieved.

In later studies, the classification of the target from more distances and the effect of atmospheric conditions on the performance of the system can be examined.

REFERENCES

- [1] Singh M, Arora AS. A Novel Face Liveness Detection Algorithm with Multiple Liveness Indicators. Wireless Personal Communications 2018;100:1677–87. https://doi.org/10.1007/S11277-018-5661-1.
- [2] Matthew P, Anderson M. Novel categorisation techniques for liveness detection. Proceedings 2014 8th International Conference on Next Generation Mobile Applications, Services and Technologies, NGMAST 2014 2014:153–8. https://doi.org/10.1109/NGMAST.2014.51.
- [3] Fei J, Xia Z, Yu P, Xiao F. Adversarial attacks on fingerprint liveness detection. Eurasip Journal on Image and Video Processing 2020;2020:1–11. https://doi.org/10.1186/S13640-020-0490-Z/TABLES/7.
- [4] Debnath SBC. TTW life sign detection by means of CW X-band radar, homeland security and rescue applications. 2017 USNC-URSI Radio Science Meeting (Joint with AP-S Symposium), USNC-URSI 2017, Institute of Electrical and Electronics Engineers Inc.; 2017, p. 89–90. https://doi.org/10.1109/USNC-URSI.2017.8074911.
- [5] Zhang H, Zhang L, Gao Q, Xiao Y, Hong H, Zhu X. Body Movement Cancellation Based on Hybrid Radar-Webcam Sensing System. IEEE MTT-S 2019 International Microwave Biomedical Conference, IMBioC 2019 - Proceedings, Institute of Electrical and Electronics Engineers Inc.; 2019. https://doi.org/10.1109/IMBIOC.2019.8777873.
- [6] JalaliBidgoli F, Moghadami S, Ardalan S. A Compact Portable Microwave Life-Detection Device for Finding Survivors. IEEE Embedded Systems Letters 2016;8:10–3. https://doi.org/10.1109/LES.2015.2489209.
- [7] Wu CW, Huang ZY. Using the phase change of a reflected microwave to detect a human subject behind a barrier. IEEE Transactions on Biomedical Engineering 2008;55:267–72. https://doi.org/10.1109/TBME.2007.910680.
- [8] Liu S, Song Y, Zhang M, Zhao J, Yang S, Hou K. An Identity Authentication Method Combining Liveness Detection and Face Recognition. Sensors 2019, Vol 19, Page 4733 2019;19:4733. https://doi.org/10.3390/S19214733.
- [9] Shi M, Wang H, Sun J, Liu C, Huang Z, Zhang B. Face liveness detection benchmark based on stereo matching. ACM International Conference Proceeding Series 2019. https://doi.org/10.1145/3349801.3349811.
- [10] Hassan MA, Mustafa MN, Wahba A. Automatic liveness detection for facial images. Proceedings of ICCES 2017 12th International Conference on Computer Engineering and Systems 2018;2018-January:215–20. https://doi.org/10.1109/ICCES.2017.8275306.
- [11] Sun L, Pan G, Wu Z, Lao S. Blinking-Based Live Face Detection Using Conditional Random Fields. Lecture Notes in Computer Science (Including Subseries Lecture Notes in Artificial Intelligence and Lecture Notes in Bioinformatics) 2007;4642 LNCS:252–60. https://doi.org/10.1007/978-3-540-74549-5_27.
- [12] Menotti D, Chiachia G, Pinto A, Schwartz WR, Pedrini H, Falcão AX, et al. Deep Representations for Iris, Face, and Fingerprint Spoofing Detection. IEEE Transactions on Information Forensics and Security 2015;10:864–79. https://doi.org/10.1109/TIFS.2015.2398817.
- [13] Jung E, Hong K. Biometric verification based on facial profile images for mobile security. Journal of Systems and Information Technology 2015;17:91–100. https://doi.org/10.1108/JSIT-03-2014-0020/FULL/PDF.
- [14] GuangZhu X, PanLong Y, BangJun L, YaoBin Z, JiQuan Y. Eye Region Activity State based Face Liveness Detection System. International Journal of Security and Its Applications 2016;10:361–74. https://doi.org/10.14257/ijsia.2016.10.1.33.
- [15] Lee TW, Ju GH, Liu HS, Wu YS. Liveness detection using frequency entropy of image sequences. ICASSP, IEEE International Conference on Acoustics, Speech and Signal Processing Proceedings 2013:2367–70. https://doi.org/10.1109/ICASSP.2013.6638078.
- [16] Park E, Kim W, Li Q, Kim H, Kim J. Fingerprint liveness detection using CNN features of random sample patches: Liveness detection using CNN features. Lecture Notes in Informatics (LNI),

- Proceedings Series of the Gesellschaft Fur Informatik (GI) 2016;P-260. https://doi.org/10.1109/BIOSIG.2016.7736923.
- [17] Ghiani L, Yambay DA, Mura V, Marcialis GL, Roli F, Schuckers SA. Review of the Fingerprint Liveness Detection (LivDet) competition series: 2009 to 2015. Image and Vision Computing 2017;58:110–28. https://doi.org/10.1016/J.IMAVIS.2016.07.002.
- [18] Lavrentyeva G, Kudashev O, Melnikov A, de Marsico M, Matveev Y. Interactive Photo Liveness for Presentation Attacks Detection. Lecture Notes in Computer Science (Including Subseries Lecture Notes in Artificial Intelligence and Lecture Notes in Bioinformatics) 2018;10882 LNCS:252–8. https://doi.org/10.1007/978-3-319-93000-8_29.
- [19] Dong J, Tian C, Xu Y. Face liveness detection using color gradient features. 2017 International Conference on Security, Pattern Analysis, and Cybernetics, SPAC 2017 2018;2018-January:377–82. https://doi.org/10.1109/SPAC.2017.8304308.
- [20] Al-Naji A, Perera AG, Mohammed SL, Chahl J. Life Signs Detector Using a Drone in Disaster Zones. Remote Sensing 2019, Vol 11, Page 2441 2019;11:2441. https://doi.org/10.3390/RS11202441.
- [21] Maiman TH. Stimulated Optical Radiation in Ruby. Nature 1960 187:4736 1960;187:493–4. https://doi.org/10.1038/187493a0.
- [22] Nasim H, Jamil Y. Diode lasers: From laboratory to industry. Optics and Laser Technology 2014;56:211–22. https://doi.org/10.1016/j.optlastec.2013.08.012.
- [23] Schnabel R. Squeezed states of light and their applications in laser interferometers. Physics Reports 2017;684:1–51. https://doi.org/10.1016/j.physrep.2017.04.001.
- [24] Yu TY. Laser-based sensing for assessing and monitoring civil infrastructures. Sensor Technologies for Civil Infrastructures, vol. 1, Elsevier Inc.; 2014, p. 327–56. https://doi.org/10.1533/9780857099136.327.
- [25] Lutzmann P, Göhler B, van Putten F, Hill CA. Laser vibration sensing: overview and applications. In: Kamerman GW, Steinvall O, Bishop GJ, Gonglewski JD, Lewis KL, Hollins RC, et al., editors. Electro-Optical Remote Sensing, Photonic Technologies, and Applications V, 2011, p. 818602. https://doi.org/10.1117/12.903671.
- [26] Lutzmann P, Göhler B, Hill CA, Putten F van. Laser vibration sensing at Fraunhofer IOSB: review and applications. Optical Engineering 2016;56:031215. https://doi.org/10.1117/1.OE.56.3.031215.
- [27] Zalevsky Z, Beiderman Y, Margalit I, Gingold S, Teicher M, Mico V, et al. Simultaneous remote extraction of multiple speech sources and heart beats from secondary speckles pattern. Optics Express 2009;17:21566–80. https://doi.org/10.1364/OE.17.021566.
- [28] Yazdanfar S, Kulkarni MD, Izatt JA. High resolution imaging of in vivo cardiac dynamics using color Doppler optical coherence tomography. Optics Express 1997;1:424. https://doi.org/10.1364/OE.1.000424.
- [29] Cikajlo I, Šprager S, Erjavec T, Zazula D. Cardiac arrhythmia alarm from optical interferometric signals during resting or sleeping for early intervention. Biocybernetics and Biomedical Engineering 2016;36:267–75. https://doi.org/10.1016/j.bbe.2015.12.006.
- [30] Šprager S, Zazula D. Detection of heartbeat and respiration from optical interferometric signal by using wavelet transform. Computer Methods and Programs in Biomedicine 2013;111:41–51. https://doi.org/10.1016/j.cmpb.2013.03.003.
- [31] Leader in Optical Measurement Equipment Polytec n.d. https://www.polytec.com/eu/ (accessed February 6, 2020).
- [32] Scalise L, Morbiducci U, Melis M De. A laser Doppler approach to cardiac motion monitoring: effects of surface and measurement position. SPIE Proceedings, vol. 6345, 2006, p. 63450D-63450D 11. https://doi.org/10.1117/12.693151.
- [33] Scalise L, Morbiducci U. Non-contact cardiac monitoring from carotid artery using optical vibrocardiography. Medical Engineering & Physics 2008;30:490–7. https://doi.org/10.1016/j.medengphy.2007.05.008.
- [34] De Melis M, Morbiducci U, Scalise L. Identification of cardiac events by Optical Vibrocardiograpy: Comparison with Phonocardiography. Annual International Conference of the IEEE Engineering in Medicine and Biology Proceedings, 2007. https://doi.org/10.1109/IEMBS.2007.4352949.
- [35] Yufu Qu, Tao Wang, Zhigang Zhu. Remote audio/video acquisition for human signature detection. 2009 IEEE Computer Society Conference on Computer Vision and Pattern Recognition Workshops, IEEE; 2009, p. 66–71. https://doi.org/10.1109/CVPRW.2009.5204294.
- [36] Marchionni P, Scalise L, Antonioli L, nobile S, Carnielli VP. Non-contact procedure to measure heart and lung activities in preterm pediatric patients with skin disorders. In: Longo L, editor. Laser Florence 2017: Advances in Laser Medicine, vol. 10582, SPIE; 2018, p. 20. https://doi.org/10.1117/12.2316345.
- [37] Takano C, Ohta Y. Heart rate measurement based on a time-lapse image. Medical Engineering and Physics 2007;29:853–7. https://doi.org/10.1016/j.medengphy.2006.09.006.

- [38] Ozana N, Margalith I, Beiderman Y, Kunin M, Campino GA, Gerasi R, et al. Demonstration of a Remote Optical Measurement Configuration That Correlates with Breathing, Heart Rate, Pulse Pressure, Blood Coagulation, and Blood Oxygenation. Proceedings of the IEEE 2015;103:248–62. https://doi.org/10.1109/JPROC.2014.2385793.
- [39] Olgun N, Türkoğlu İ. Lazer İşaretleri ile Otomatik Hedef Tanıma. Sakarya University Journal of Computer and Information Sciences 2018;1:1–10.
- [40] Olgun N, Türkoğlu İ. Defining materials using laser signals from long distance via deep learning. Ain Shams Engineering Journal 2022;13:101603. https://doi.org/10.1016/J.ASEJ.2021.10.001.
- [41] Gülsoy M. Lazerlerin Tıptaki Uygulamaları n.d.
- [42] LeCun Y, Bengio Y, Hinton G. Deep learning. Nature 2015;521:436–44. https://doi.org/10.1038/nature14539.
- [43] Hinton GE, Salakhutdinov RR. Reducing the dimensionality of data with neural networks. Science 2006. https://doi.org/10.1126/science.1127647.
- [44] Cireşan DC, Meier U, Gambardella LM, Schmidhuber J. Handwritten Digit Recognition with a Committee of Deep Neural Nets on GPUs. ArXiv Preprint ArXiv:11034487 2011.
- [45] Huang Z, Dong M, Mao Q, Zhan Y. Speech emotion recognition using CNN. MM 2014 Proceedings of the 2014 ACM Conference on Multimedia, 2014, p. 801–4. https://doi.org/10.1145/2647868.2654984.
- [46] Palaz D, Magimai-Doss M, Collobert R. Analysis of CNN-based speech recognition system using raw speech as input. Proceedings of the Annual Conference of the International Speech Communication Association, INTERSPEECH, vol. 2015- Janua, 2015, p. 11–5.
- [47] Zhang JS, Xiao XC. Predicting chaotic time series using recurrent neural network. Chinese Physics Letters 2000;17:88–90. https://doi.org/10.1088/0256-307X/17/2/004.
- [48] Kalchbrenner N, Blunsom P. Recurrent continuous translation models. EMNLP 2013 2013 Conference on Empirical Methods in Natural Language Processing, Proceedings of the Conference, Association for Computational Linguistics; 2013, p. 1700–9.
- [49] Cho K, Van Merriënboer B, Gulcehre C, Bahdanau D, Bougares F, Schwenk H, et al. Learning phrase representations using RNN encoder-decoder for statistical machine translation. EMNLP 2014 2014 Conference on Empirical Methods in Natural Language Processing, Proceedings of the Conference, 2014, p. 1724–34. https://doi.org/10.3115/v1/d14-1179.
- [50] Morioka T, Iwata T, Hori T, Kobayashi T. Multiscale recurrent neural network based language model. Proceedings of the Annual Conference of the International Speech Communication Association, INTERSPEECH, vol. 2015- Janua, 2015, p. 2366–70.
- [51] Greff K, Srivastava RK, Koutnik J, Steunebrink BR, Schmidhuber J. LSTM: A Search Space Odyssey. IEEE Transactions on Neural Networks and Learning Systems 2017;28:2222–32. https://doi.org/10.1109/TNNLS.2016.2582924.
- [52] Fushiki T. Estimation of prediction error by using K-fold cross-validation. Statistics and Computing 2011;21:137–46. https://doi.org/10.1007/s11222-009-9153-8.
- [53] Kiran R, Kumar P, Bhasker B. Oslcfit (organic simultaneous LSTM and CNN Fit): A novel deep learning based solution for sentiment polarity classification of reviews. Expert Systems with Applications 2020;157:113488. https://doi.org/10.1016/j.eswa.2020.113488.

Assessment of Durability of Inkjet Prints on Laboratory Paper Substrates with Wheat Pulp Based on Rub Resistance

Maja Rudolf^{1*}, Katja Petric Maretić¹, Irena Bates¹, Ivana Plazonić¹, Valentina Radić Seleš¹

¹ University of Zagreb, Faculty of Graphic Arts, 10000, Zagreb, Croatia.

*Corresponding Author email: maja.rudolf@grf.unizg.hr

Abstract

Paper recycling is becoming increasingly important as the production of packaging and various printed products grows. As alternative to wood fiber that is the most common raw material in paper production this research examines the quality of paper which is made with addition of non-wood fibers derived from wheat straw. For this purpose, laboratory paper substrates were made by blending recycled newspaper pulp and wheat straw pulp in different proportions. In this study we analyse rub resistance of laboratory paper substrates with variable content of wheat pulp printed in full tone with black and yellow inks by digital ink jet printing technique. The main objective of this research is to determine whether this kind of print has necessary durability for carrying stable illustrations. One of the main characteristics of print quality is resistance to rubbing which is very important for packaging during transport, storage and the end use. Rub resistance test was executed according to BS 3110 standard. The print durability was assessed through the Euclidean color difference and the individual CIE L*a*b* differences before and after the rub tests. The analysis showed that the increase of wheat pulp content in paper substrates has affected the increase of color difference. Greater rub resistance was observed on substrates with lower share of wheat pulp. Samples printed with yellow ink showed overall greater durability than samples printed with black ink. In further analysis we observed that for the black prints the difference in lightness ($\Delta L'$) of the CIE L*a*b* color space was most affected as the prints became lighter with the number of rubbing cycles. In samples printed with vellow ink most affected was the color difference on vellow-blue axis ($\Delta b'$) meaning that the yellowness of the prints was degrading with the number of rubbing cycles.

Key words

durability, inkjet printing, paper substrate, rub resistance, wheat pulp

1. INTRODUCTION

Rapid rise in the production of paper products leads the paper industry to the search for alternative fiber sources that would reduce or replace wood as a main source of virgin fiber in papermaking processes. So far, the alternative sources of the virgin fibers can be categorized as: agricultural crop residues such as cereal or straw residues, natural growing plants such as miscanthus, reeds or other grasses and non-wood crops that include textile crops such as cotton or flax [1]. Agricultural crops residues are interesting for their abundance and low cost but also for the shorter growing cycle than wood [2]. As the most available crop that is grown in Croatia is

wheat [3], this research was focused on examining the quality and durability of laboratory paper substrates produced with different ratios of wheat straw fibers. The wheat straw was collected after harvesting, cut and converted to wheat pulp according to soda method where fibers are separated from plant tissue [4]. Wheat pulp was blended with wood pulp from recycled newsprint paper in different ratios to improve the characteristics of shortened recycled wood fibers [5]. The previous research has led to the conclusion that the addition of wheat pulp up to 30% provide good quality of the prints on such laboratory paper substrates [6-8].

Rub resistance is defined as the ability to resist damage during the friction of two surfaces in contact [9]. It is very important feature of the printed material, especially packaging, because it must endure the process of shipment, storage, and handling from production phase to the end use. It can be evaluated visually or by calculating Euclidean color differences (ΔE_{00}) of printed materials in the CIE L*a*b* color space [10].

2. MATERIALS AND METHODS

The research was divided into four phases: production of laboratory paper substrates, printing, rub resistance testing and spectrophotometric measurements of colorimetric values before and after the rub resistance testing to determine the changes in print coloration.

2.1. Production of Laboratory Paper Substrates

Four types of paper substrates were produced with different weight ratios of recycled newsprint pulp and wheat pulp:

- N reference paper substrate with 100% recycled newsprint pulp,
- 1NW with 90% recycled newsprint pulp and 10% wheat straw pulp,
- 2NW with 80% recycled newsprint pulp and 20% wheat straw pulp,
- 3NW with 70% recycled newsprint pulp and 30% wheat straw pulp.

2.2. Printing

In the second phase laboratory paper substrates were printed using inkjet printing technique on EFI Rastek H652 digital printer. UV curable black and yellow inks were printed in full tone over the paper substrates. Settings of the printer were adjusted to "high quality" printing mode, with 8 passes in 600 dpi resolution and the printing speed of 12.1 m²/h.

2.3. Rub resistance testing

Printed paper substrates were cut to smaller round samples with the diameter of 5 cm. The rub resistance test was performed on a tribometer Hanatek T4 Rub and Abrasion Tester according to the BS 3110:1959 standard under the constant pressure of 0.23 kg (0.5 lb) with rotational motions of 20, 40 and 60 cycles at the speed of 1 revolutions per second.

2.4. Spectrophotometric measurement of colorimetric values

Before the paper substrates were subjected to rub resistance tests the spectrophotometric measurements were made to determine the CIE L*a*b* colorimetric values of each printed sample. After the rub resistance tests had been made, the measurements were repeated and the Euclidean color difference ΔE_{00} was calculated according to CIEDE2000 formula (1). Device used for the spectrophotometric measurements was SpectroEye with illuminant D50 and 2° observer angle.

$$\Delta E_{00} = \sqrt{\left(\frac{\Delta L'}{k_L S_L}\right)^2 + \left(\frac{\Delta C'}{k_C S_C}\right)^2 + \left(\frac{\Delta H'}{k_H S_H}\right)^2 + R_T \left(\frac{\Delta C'}{k_C S_C}\right) \left(\frac{\Delta H'}{k_C S_H}\right)}$$
(1)

where: $\Delta L'$ is representing the difference in lightness between printed samples before and after the rub resistance test, $\Delta C'$ is the chroma difference between printed samples before and after the rub resistance test and $\Delta H'$ is the hue difference between printed samples before and after the rub resistance test. R_T is the rotation function, while k_L , k_C , k_H are the parametric factors for variation in the experimental conditions and S_L , S_C , S_H are the weighting functions [11].

In addition to the ΔE_{00} calculations, the difference of individual components of the CIE L*a*b* color space $\Delta L'$, $\Delta a'$ and $\Delta b'$ was calculated according to the formulas (2), (3) and (4) where the value marked with index 1

74 Rudolf et al.

represents the value measured before the rub resistance test and the value marked with index 2 represents the value measured after the test.

$$\Delta L' = L_1^* - L_2^* \tag{2}$$

$$\Delta a' = a_1^* - b_2^* \tag{3}$$

$$\Delta b' = b_1^* - b_2^* \tag{4}$$

Durability is considered acceptable or print quality is good if the value of the Euclidean color difference is less than 1 and can be tolerated up to 2. The untrained eye of the observer does not notice a difference in color change for those values of ΔE_{00} [12].

3. RESULTS AND DISCUSSION

Euclidean color difference (ΔE_{00}) was measured before and after the rub resistance test on 30 samples, and average value was calculated. Table 1. shows values of ΔE_{00} for four types of paper substrates (N, 1NW, 2NW and 3NW) printed in full tone black and yellow after the rub resistance test with 20, 40 and 60 rubbing cycles. Prints on paper substrates with added wheat pulp showed slightly increased color difference compared to the prints on the reference paper substrates without added wheat pulp.

For the black prints, calculated color difference on samples marked N was 0.55 for 20 cycles, and 0.75 for 40 and 60 cycles, meaning that the color difference can't be perceived with the untrained eye and that the black prints are stable to rubbing. Black prints on papers with added wheat pulp show lesser durability and more fluctuation in rub resistance tests, regardless of the number of cycles and wheat content, with increased value of Euclidean color difference ranging from 0.77 to 1.2.

The Euclidean color difference for the yellow prints is less pronounced as indicated by the low ΔE_{00} values ranging from 0.39 to 0.51 on reference substrates marked N. Substrates with added wheat pulp showed a slight increase in Euclidean color difference values from 0.43 to 0.86 that predictably rise with the number of rub test cycles.

Table 1. Average ΔE_{00} values of black and yellow prints made on four paper substrates N, 1NW, 2NW and 3NW after the rub resistance test with 20, 40 and 60 rubbing cycles

Paper substrate type		N			1NW			2NW			3NW	
No. of rubbing cycles	20	40	60	20	40	60	20	40	60	20	40	60
Average ΔE_{00}												
Black prints	0.55	0.75	0.75	0.98	0.83	0.91	0.8	0.82	1.2	0.77	0.79	0.98
Yellow prints	0.42	0.39	0.51	0.43	0.62	0.69	0.55	0.72	0.66	0.62	0.62	0.86

Further calculations have examined the difference of individual components of the CIE L*a*b* color space (ΔL ', Δa ' and Δb ') with purpose to determine which of them were most affected by rub tests in respect of 20, 40 and 60 rubbing cycles. As predicted, the paper substrates printed with black ink had most significant change in L^* component which suggests that the rubbing test had most impact on lightness. Figure 1. shows the charts with the difference of ΔL ', Δa ' and Δb ' for each type of the tested paper substrates. The reference substrate marked N showed gradual increase in ΔL ' values with the increased number of rubbing cycles (Figure 1.a). The negative values indicating that the black color tone becomes lighter. Change on a^* (green/red) and b^* (blue/yellow) axis was slightly rising in the positive direction (< 0.2), although the changes cannot be perceived with the human eye. With the addition of wheat pulp, color durability showed greater fluctuations compared to reference paper substrate, with unpredictable results of ΔL ' in relation to the number of rubbing cycles. However, Figure 1. b), c) and d) shows that all calculated ΔL ' values were measured in the acceptable range < 1.2. In the paper substrates with added wheat pulp, the Δa ' values did not change significantly and the Δb ' values had slight increase with the number of rubbing cycles, although the difference was insignificant (< 0.4). The amount of wheat pulp in the paper substrate had no significant impact on the measured values.

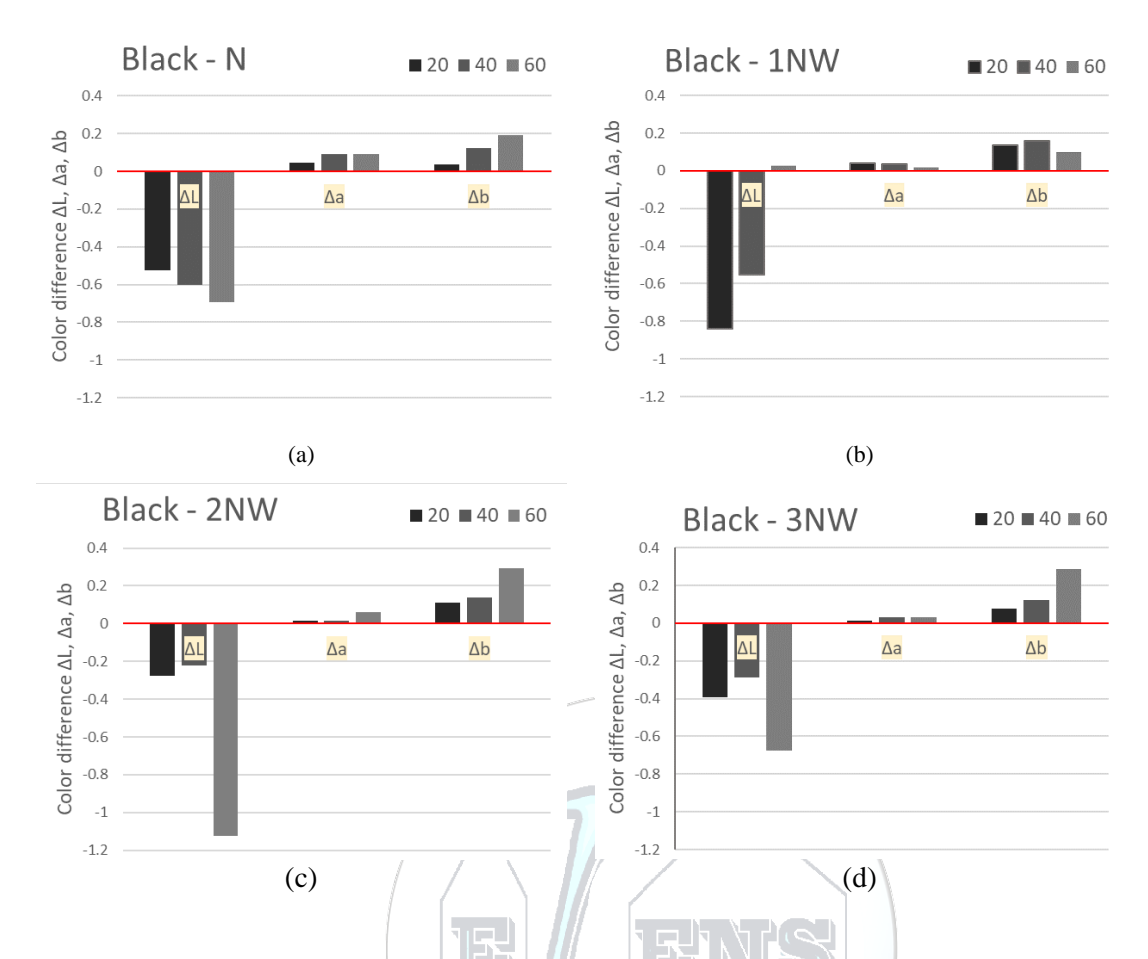


Figure 1. Color difference of $\Delta L'$, $\Delta a'$ and $\Delta b'$ for black prints on four paper substrates N, 1NW, 2NW and 3NW calculated from measurements before and after the rub resistance test with 20, 40 and 60 cycles

The greatest differences in b^* component of the CIE L*a*b* color space – the blue/yellow axis, was observed on prints with yellow ink. The reference sample (Figure 2.a) shows increase in ΔL ' values in the acceptable range < 0.5 and shows good durability throughout 20, 40 and 60 rubbing cycles. The color difference in the component a^* – the red/green axis – had shown insignificant increase < 0.2, after the rub resistance testing. As expected, the greatest difference was observed for the Δb ' with the increased values in the positive range < 1.5, indicating that the yellow color after the rubbing test has slightly decreased yellowness. Figure 2. b), c) and d) show calculated values of ΔL ', Δa ' and Δb ' for yellow prints on paper substrates with added wheat pulp. The change in lightness indicated with ΔL ' has insignificantly increased compared to the reference substrate, measuring < 0.73 given the highest number of rubbing cycles. Differences Δa ' have not changed significantly in respect to the rubbing cycles and increase of wheat amount in the paper substrate (< 0.5). In the b^* axis changes were more pronounced after 40 and 60 rubbing cycles compared to the reference paper substrate, resulting with Δb ' of ~1 with 20 rubbing cycles regardless of wheat content, from 1.3 to 1.5 for 40 rubbing cycles and from 1.8 to 2 for 60 rubbing cycles. These results can still be categorized as acceptable with the very small color difference.

76 Rudolf et al.

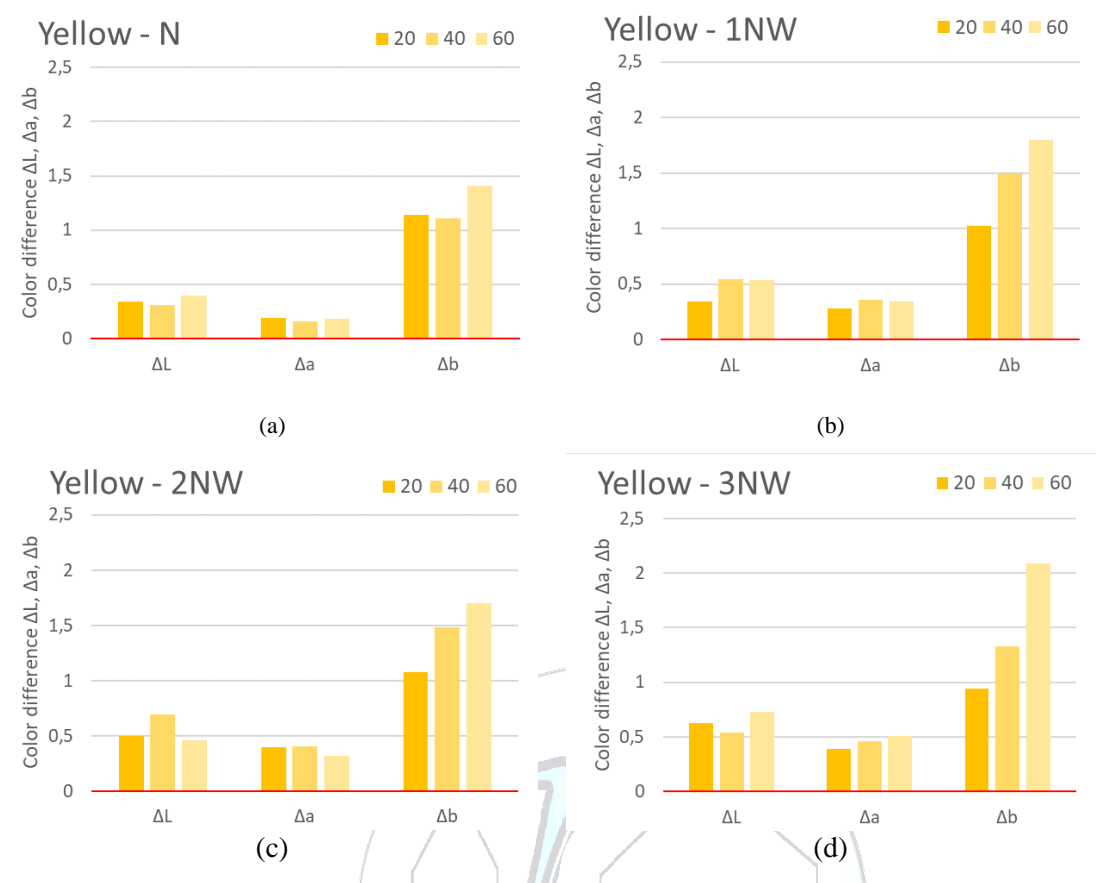


Figure 2. Color difference of ΔL ', Δa ' and Δb ' for yellow prints on four paper substrates N, 1NW, 2NW and 3NW calculated from measurements before and after rub resistance test with 20, 40 and 60 cycles

4. CONCLUSION

In this paper the durability of black and yellow prints made on the paper substrates with added wheat pulp was assessed based on the rub resistance testing. The calculated Euclidean color difference and the color difference of separate components of the CIE L*a*b* color space values showed the satisfactory level of print durability for the black and yellow prints. Lesser rub durability of prints was determined on the paper substrates with added wheat pulp than on the reference substrate without wheat pulp, but the results were still in the acceptable ranges. The prints in full tone black ink showed overall the greater Euclidean color difference than the prints made with full tone yellow ink which indicated that the yellow prints were more durable in comparison with black ones. Black samples on paper substrates with added wheat pulp showed slightly unpredictable results in the ΔL ' calculations regardless of the percentage of added wheat pulp or the number of rubbing cycles in the resistance testing. All results were within acceptable ranges. Yellow prints on paper substrates with added wheat pulp showed the greatest increase in Δb ' component with respect of the rubbing cycles increase, meaning there was a slight loss of yellowness in the color, but also in the acceptable range. The amount of wheat pulp in the substrate had not significantly affected results. It can be concluded that laboratory paper substrates with added wheat pulp up to 30% has provided satisfactory durability of digital inkjet prints in the rub resistance tests and can be recommended for further development in creating paper for packaging and other purposes.

ACKNOWLEDGMENT

This work has been supported in part by Croatian Science Foundation under the project "Printability, quality and utilization of substrates with non-wood fibers" (UIP-2017-05-2573) and by the University of Zagreb.

CONFLICT OF INTEREST STATEMENT

The authors declare that there is no conflict of interest.

REFERENCES

- [1]. E. S. Abd El-Sayed, M.E. l-Sakhawy, and M. El-Sakhawy, "Non-wood fibers as raw material for pulp and paper industry", *Nordic Pulp & Paper Research Journal* vol. 35(2), pp. 215-230, 2020.
- [2]. G. Fang, and K. Shen, "Wheat Straw Pulping for Paper and Paperboard Production", Chapter 12 in Global Wheat Production, Intech Open, Edited by Shah Fahad, pp. 223-239, 2018.
- [3]. "Agriculture, Hunting, Forestry and Fishing: Crop production" Croatian Bureau of Statistics, Available: http://www.dzs.hr/PXWeb/sq/f89a3233-db53-4c01-a514-f8e59e54bd81
- [4]. I. Plazonić, I. Bates, and Ž. Barbarić-Mikočević, "The Effect of Straw Fibers in Printing Papers on Dot Reproduction Attributes, as Realized by UV Inkjet Technology", *BioResources*, vol. 11(2), pp. 5033-5049, 2016.
- [5]. I. Plazonić, Ž. Barbarić-Mikočević, V. Džimbeg-Malčić, and I. Bates, "The rub resistance of printed papers with variable content of wheat pulp", *Proceedings of Natural resources, green technology and sustainable development/2*, 2016. pp. 76-79
- [6]. I. Plazonić; I. Bates; Ž. Barbarić-Mikočević, and B Lajić, "Chemical degradation of prints made on papers with wheat pulp", *Proceedings of International Conference on Innovative Technologies IN-TECH 2017*, 2017. pp. 117-120
- [7]. I. Bates, I. Plazonić, V. Džimbeg-Malčić, and D. Banić, "Influence of straw pulp in printing substrate on stability of digital prints", *Proceedings of International Conference on Innovative Technologies IN-TECH* 2017, 2017. pp. 113-116
- [8]. M. Rudolf, I. Plazonić, K. Petric Maretić, I. Bates, and V. Radić Seleš, "Rub resistance of ink jet prints on laboratory substrates with wheat pulp" *Proceedings of Printing & Design* 2020., 2020, pp. 126-131
- [9]. J. Vališ, B. Jašurek, and T. Syrovy, "Methodology of evaluation of print abrasion resistance", *Proceedings in Wood, Pulp & Paper Polygrafia Academica*, 2014, pp. 107-110
- [10]. S. Jamnicki Hanzer, R. Kulčar, M. Vukoje, and P. Širol, "Mechanical and chemical resistance of thermochromic packaging prints", *Proceedings The Tenth International Symposium GRID 2020*, 2020, pp. 109-118
- [11]. G. Sharma, W. Wu, and E. N. Dalal, "The CIEDE2000 color-difference formula: implementation notes, supplementary test data, and mathematical observations", *ColorResearch and Application*, vol. 30, pp. 21–30, 2005.
- [12]. I. Zjakić, Upravljanje kvalitetom ofsetnog tiska, Zagreb, Croatia: Hrvatska sveučilišna naklada, 2007.

Comparison of Optical Stability of Papers Containing Wheat Pulp Printed with Digital and Flexographic Printing Technique after Accelerated Ageing

Valentina Radić Seleš^{1*}, Irena Bates¹, Maja Rudolf², Ivana Plazonić³, Katja Petric Maretić³

¹University of Zagreb Faculty of Graphic Arts, Department of printing processes, 10000, Zagreb, Croatia
²University of Zagreb Faculty of Graphic Arts, Department of Computer Graphics and Multimedia Systems, 10000, Zagreb, Croatia
³University of Zagreb Faculty of Graphic Arts, Department of Fundamental and General Knowledge, 10000, Zagreb, Croatia
*Corresponding Author email: valentina.radic.seles@grf.unizg.hr

Abstract

Flexographic and digital printing are currently the fastest growing branches in the printing industry. The selection of printing substrates for these printing techniques is large, but paper substrates are the most widely used. Paper manufacturing is based mainly on the use of renewable fibers, and the dominant fiber resource for the pulp and paper industry is wood which is accounting for 90% of the world's fiber utilization. As woods consumption for paper production is still high, there are various possibilities to reduce it. One way is by reducing the proportion of wood pulp in paper by adding straw pulp of various cereals such as wheat. Wheat straw has numerous advantages and can be used in pulp form as a source of primary fibers for paper production. As paper as a multicomponent material, besides fibers composed of cellulose, hemicellulose and lignin also includes additives, minerals and synthetic polymers. Due to its complex nature it is prone to deterioration when exposed to elevated temperature, humidity and light. Paper ageing is irreversible change and is the best indicator of paper optical permanence. Objective of this study was to determine the optical stability of prints after undergoing aging treatment with elevated temperature and UV light for 48 and 96 hours. Laboratory papers containing wheat pulp were printed by two printing techniques with cyan and yellow inks to compare better optical stability: UV inkjet and flexographic technique. The optical stability of all prints was observed based on the difference in the reflection spectra (ΔR). The results indicated that all laboratory papers printed with cyan ink with flexographic technique show better optical stability than the ones printed with digital technique. Laboratory papers printed with yellow ink by both techniques show good optical stability.

Key words

Accelerated ageing, Digital, Flexographic, Optical stability, Prints, Wheat pulp

1. INTRODUCTION

Flexography printing is a method of direct printing, that uses resilient relief image plates of rubber or photopolymer material. The plates are inked by a cell-structured, ink-metering "anilox" roll carrying a fast-drying fluid ink to plates which achieve high quality printed reproduction of text and images on any substrate, absorbent or nonabsorbent. Flexographic printing is an efficient, cost-effective and versatile printing method. Flexography printing uses low-viscosity inks which dry very quickly between the printing units of a printing machine. Solvent-based, water-based and ultraviolet-curable inks are used in flexographic printing and the appropriate ink for each

substrate must be very careful chosen. Adhesion, block resistance, rub resistance, heat resistance and lightfastness can be satisfactory on one substrate but terrible on another. Different ink systems require different control and different conditions [1]. Recently developed digital printing technique differs from traditional, analog printing methods because digital printing machines do not require any printing plates. Instead of using printing plates to transfer a printing image, digital printing machines print the ink directly onto the printing substrate. Ink jet printing is a technique where inkjet heads deposit droplets of ink on the paper as the printing substrate and the image is produced by means of a dot matrix that creates the letter or graphic image [2]. Digital production print technology is evolving quickly, and its output quality is improving continuously [3]. It is predicted that digital printing technique will grow dramatically as press become cheaper with improvements in the print quality [2]. Flexographic and digital printing, both with their advantages and disadvantages can print on all kinds of substrates from paper, board, polymer materials (foil and film) to thick cardstock, heavyweight papers, folding cartons and fabric. [1,3]. Since paper is the most widely used printing substrate all over the world and wood is currently dominant raw material for paper manufacture, it would be sensible and commercially viable to replace it as much as possible with other plant biomasses by utilization of non-wood fiber materials to produce cellulose pulps [4,5]. The nonwood fibers have some features that are superior to those of wood fiber and others that represent clear disadvantages, such as fiber storage issues. Nonetheless, it is possible to manufacture high-quality paper from these fibers. The cellulose content of wheat straw is very similar to that of wood. The hemicellulose content tends to be higher, but the lignin content is considerably lower. The lower lignin content is an advantage in papermaking [4]. Several studies have shown that straw fibers from certain cereals like wheat show suitable characteristics required for pulp and paper production.

The quality and appearance of graphic product are crucial when end users consider buying products [6]. Therefore, optical stability is amongst most important factors when it comes to product appearance. Paper is constantly exposed to numerous endogenous and exogenous factors that affect its stability. Due to factors such as heat, light and moisture, paper ageing processes cause change in chemical and mechanical properties of paper elements and ink components during the ageing process [7]. Artificial ageing speeds the natural ageing process of paper by subjecting it to extreme conditions for certain period of time and is used to determine the lifespan or permanence of paper or even to predict the long-term effects of conservation treatments [8]. In researches several methods of simulation of the natural ageing process are used, since the process of natural ageing is impractical because of the involved period of time [9]. In this research, the optical stability of flexography and digital prints made on substrates with wheat pulp will be observed trough difference in reflectance spectra where deterioration will be visible after accelerated ageing process.

2. MATERIALS AND METHODS

2.1. Laboratory Papers

Wheat straw was converted into semi-chemical pulp according to soda method [10]. Pulping conditions are presented in Table 1.

Table 1. Pulping conditions

Type of straw	Pulping method	Extraction conditions			
Wheat	Soda pulping	Temperature of 120°C, alkali level of 16% for 60 min, and a 10:1 liquid biomass ratio			

Obtained unbleached wheat pulp was mixed with recycled wood pulp in different weight ratios, 10%, 20% and 30%. A laboratory paper containing only recycled wood pulp was used as a reference paper in the process

80 Radić Seleš et al.

of comparing quality of optical properties of laboratory papers containing wheat pulp. Laboratory papers weighed approximately 42.5 gm⁻² were formed by a Rapid Köthen sheet former ((FRANK- PTI GmbH, Birkenau Germany) according to EN ISO 526 9-2:2001 standard [11]. In total, 4 types of laboratory papers were formed. Abbreviations used in marking all samples are listed in Table 2.

Table 2. Abbreviations used in marking samples

100R	laboratory paper with 100 % recycled pulp (reference)
90R10W	laboratory paper with 90% recycled pulp and 10% wheat pulp
80R20W	laboratory paper with 80% recycled pulp and 20% wheat pulp
70R30W	laboratory paper with 70% recycled pulp and 30% wheat pulp
48h	accelerated aged for 48 hours
96h	accelerated aged for 96 hours

2.2. Printing of Laboratory Papers by Flexographic Technique

All laboratory papers were printed in full tone with cyan and yellow ink by flexographic laboratory device Esiproof RK Printcoat Instruments with water based flexographic inks. Printing was performed with anilox roll with total volume of 39.1 cm3/m-2 and engraved with line screen of 40 lincm-1 at a temperature of 23° C and a relative humidity of 50%. An engraving angle for anilox roll was 60 degree angle, respectively the hexagonal cell that offers higher quantity of cells that indicates increasing in the ink transfer, as well as homogeneity.

2.3. Printing of Laboratory papers by Digital Technique

Each laboratory paper was also printed in full tone with cyan and yellow ink by digital EFI Rastek H652 UV curable inkjet printer with the resolution of 600×600 dots per inch (dpi) (respectively with high quality mode 8 pass) and printing speed of $12.10 \text{ m}^2/\text{hr}$.

2.4. Accelerated Ageing

Laboratory papers printed with both techniques were exposed to accelerated ageing treatment in the test equipment SunTEST XSL+ according to standard ASTM D 6789-02 [12] under conditions summarized in Table 3.

Conditions					
Wavelength (nm)	290 - 800				
Irradiance (Wm ⁻²)	765 ± 50				
Test equipment	SunTEST XSL+, Id.No. 196 Rotronic Hygrolog, Id.No. 180/2				
Duration process (h)	48 96				
Ambient condition	24.8°C 54.7 % RH				
Filter	daylight				

2.5. Optical Properties

For assessment the quality and permanence of the prints obtained on laboratory papers with added wheat pulp after artificial ageing, optical stability was observed trough color degradation. Color degradation was estimated through the difference in reflectance spectra between unaged and aged prints (ΔR), calculated according to the equation 1. Prints reflectance spectra measurements were processed using X-rite spectrophotometer with standard illuminate D50 and 2° observer, in the interval of the wavelengths from 400 nm to 700 nm for every 10 nm. Reflectance values (R) were measured for all printed paper samples before and after ageing. Optical measurements were repeated 25 times on each sample.

$$\Delta R = R_{unaged} - R_{aged} \tag{1}$$

3. RESULTS AND DISCUSSION

Figures 1-4 present the experimental results of reflectance measurements presented as ΔR , before and after accelerated ageing in the visible part of electromagnetic spectrum for all analyzed papers printed with digital and flexographic technique.

Following graph in Figure 1 shows the difference in reflectance values on laboratory papers printed by flexographic printing technique with cyan water based printing ink. The highest reflectance difference is visible on paper made from 100% recycled pulp after 48 hours of artificial ageing. It also shows the highest difference after 96 hours of accelerated ageing compared to other papers printed with cyan flexographic ink. The highest optical stability is visible on laboratory paper made with the addition of 10% wood pulp after 48 hours of accelerated ageing.

82 Radić Seleš et al.

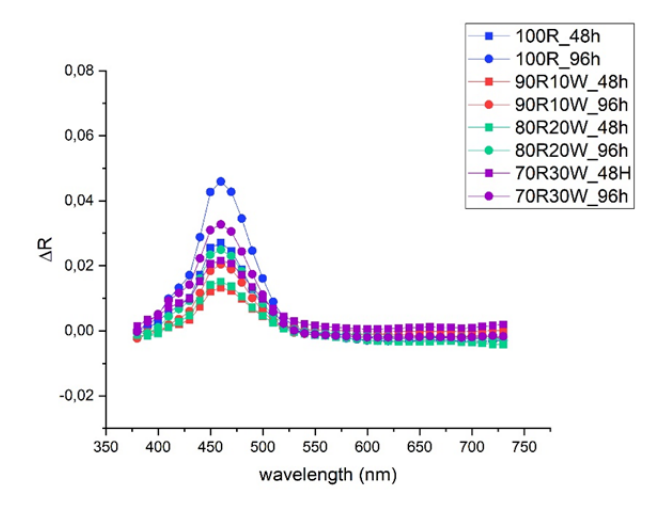


Figure 1. The influence of ageing time on reflectance spectra of cyan prints made by flexographic printing technique on laboratory papers without (100R) and with wheat pulp (90R10W, 80R20W, 70R30W)

Figure 2 shows the difference in reflectance values between unaged and aged laboratory papers printed by flexographic printing technique with yellow water based printing ink. It is visible that the highest degradation occurs on paper made from 100% recycled pulp after the first 48 hours of accelerated ageing. The best optical stability of prints provides papers made with addition of wheat pulp of 20% and 30%.

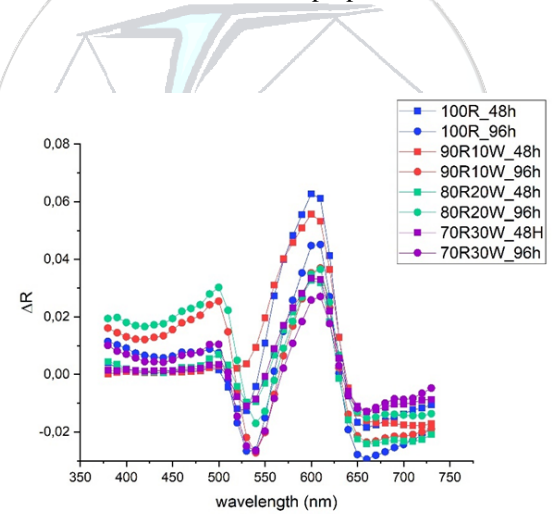


Figure 2. The influence of ageing time on reflectance spectra of yellow prints made by flexographic printing technique on laboratory papers without (100R) and with wheat pulp (90R10W, 80R20W, 70R30W)

In Figure 3, cyan prints on all laboratory papers obtained by digital printing technique present expected reflectance curves. The highest degradation of all cyan prints occurs after first 48 hours of accelerated ageing on laboratory paper 100R, paper without wheat pulp. After additional 48 hours of accelerated ageing, degradation is still visible but significantly lower. Others cyan prints obtained on laboratory papers with wheat pulp addition show similar behavior. However, cyan prints made on papers with 30% of wheat pulp exhibit the lowest reflectance differences, so they are the most stable ones. It is clearly visible that reflectance values of all cyan prints drop with addition of wheat pulp into papers.

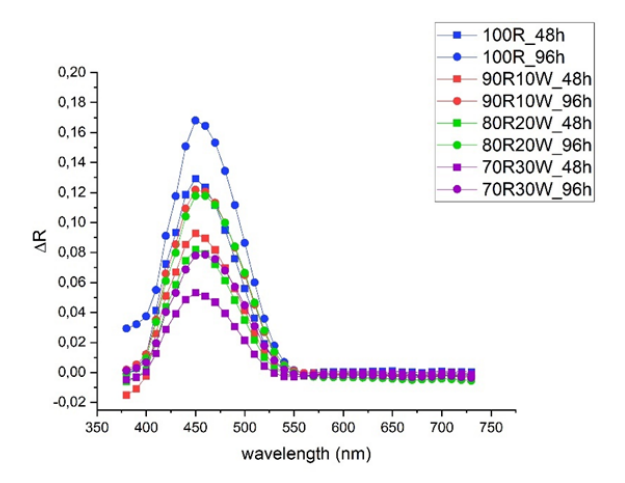


Figure 3. The influence of ageing time on reflectance spectra of cyan prints made by digital printing technique on laboratory papers without (100R) and with wheat pulp $(90R10W,\,80R20W,\,70R30W)$

Figure 4 represents the difference in reflectance values for laboratory papers printed by digital technique with yellow ink. The same trend is also visible here as on previous graph for cyan prints. The highest degradation occurs within the first 48 hours of accelerated ageing, and stability is better with each additional increase in shere of wheat pulp in printing substrate. The best optical stability was noticed on prints obtained on paper with addition of 30% wheat pulp. Yellow prints show better optical stability than cyan prints.

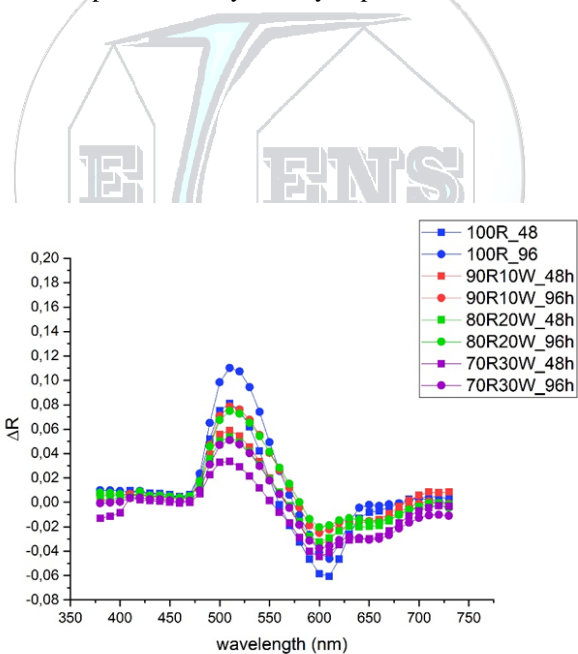


Figure 4. The influence of ageing time on reflectance spectra of yellow prints made by digital printing technique on laboratory papers without (100R) and with wheat pulp (90R10W, 80R20W, 70R30W)

84 Radić Seleš et al.

4. CONCLUSION

The aim of this research was to point out the influence of printing technique and printing substrate with wheat pulp on optical stability of prints. Considering all obtained results, the following can be concluded:

- The highest color degradation of cyan and yellow prints occurs in the first 48 hours of accelerated ageing on all papers printed with both techniques,
- Cyan ink printed with flexographic printing technique provides better optical stability than the one printed with digital technique,
- Yellow ink provides prints with higher optical stability of prints on all printing substrates than cyan ink for both printing techniques,
- Addition of wheat pulp into paper substrate positively influences optical stability of all analyzed prints

The results in this research suggest that the optical stability of prints on papers formed with addition of wheat pulp is satisfactory and could be additionally improved if papers would be formed in industrial production.

ACKNOWLEDGMENT

This work has been supported in part by Croatian Science Foundation under the project "Printability, quality and utilization of substrates with non-wood fibres" (UIP-2017-05-2573) and by the University of Zagreb.

CONFLICT OF INTEREST STATEMENT

The authors declare that there is no conflict of interest.

REFERENCES

- [1]. G. Cusdin, Flexography: Principles & Practices. 5th edition, Volume 1. Foundation of Flexographic Tehnical Association. Inc. USA, 1999.
- [2]. D. Bann, "The all new print production Handbook", Watson-Guptill Publications, New York 2007.
- [3]. Digital Printing & Types of Digital Printing Xerox, [Online] Available: https://www.xerox.com/en-ng/digital-printing/insights/what-is-digital-printing
- [4]. V. Radić Seleš, I. Bates, I. Plazonić, I. Majnarić, "Analysis of optical properties of laboratory papers with straw pulp coated with titanium dioxide white ink", Cellulose chemistry and technology, 54 (5-6), 473-483, 2020. doi:10.35812/CelluloseChemTechnol.2020.54.48.
- [5]. R. Shmulsky and P.D. Jones, "Pulp and Paper Map" 2014. The Forestry Chronicle
- [6]. N. Pauler, "Paper Optics-Optical and colour science related to the pulp and paper industry", AB Lorentzen & Wettre. Sweden, 2012
- [7]. V. Radić Seleš, I. Bates, I. Plazonić, M. Rudolf, K. Petric Maretić, V. Džimbeg-Malčić, "Optical stability of laboratory papers with wheat pulp printed by digital technique after artificial ageing" U: Oktav, M., Akgül, A., Oğuz, M., Özdemir, L., Özomay, Z. & Sesli, Y. (ur.)Proceedings of 3rd International printing technologies symposium Istanbul Turkey, 2019.
- [8]. S. Soleymani, T. Ireland, D. McNevin, "Influence of acidity on the mechanical stability of retouched Japanese tissue papers during the course of artificial ageing" AICCM Bulletin, 38:1, 3-14, 2017. DOI: 10.1080/10344233.2017.1337324
- [9]. B. Thompson, "Printing Materials: Science and Technology", Pira International, Leatherhead, Surrey, United Kingdom (2004).
- [10]. I. Plazonic, I. Bates, Z. Barbaric-Mikocevic, "The Effect of Straw Fibers in Printing Papers on Dot Reproduction Attributes, as Realized by UV Inkjet Technology" BioResources, 11(2), pp. 5033-5049, 2016.
- [11]. M. Vukoje, I. Bates, I. Plazonić, "Optical stability of papers with wheat fibers after accelerated ageing", International Conference MATRIB 2015 Materials, Wear, Recycling Proceedings, pp. 362-369, 2015.
- [12]. ASTM D 6789-02, Test Method for Accelerated Light Aging of Printing and Writing Paper by Xenon-Arc Exposure Apparatus, 2002.